UNIVERSITÀ DEGLI STUDI DI PADOVA

UNIVERSITÀ DEGLI STUDI DI PADOVA

Dipartimento di Fisica e Astronomia "Galileo Galilei"

Master Degree in Physics

Final Dissertation

An apparatus for production and spectroscopy of BaF-doped parahydrogen cryogenic crystals for electron electric dipole moment measurements

Thesis supervisor

Prof. Caterina Braggio

Thesis co-supervisor

Dr. Giovanni Carugno

Candidate

Alessandro Lippi

Academic Year 2023/2024

Contents

Abstract **1**

1 Introduction **3**
1.1 Electron Electric Dipole Moment - eEDM . . . 3
1.1.1 Detecting an eEDM - Schiff's theorem . . . 5
1.2 eEDM measurements with molecules . . . 6
1.3 State of the art . . . 9
1.4 eEDM measurements with matrix isolation of BaF . . . 11

2 Molecular sources **14**
2.1 Plasma ion source . . . 14
2.1.1 Einzel Lenses . . . 18
2.1.2 BaF ion beam . . . 20
2.2 Laser ablation . . . 22
2.2.1 Buffer gas cooling . . . 26
2.3 Molecules spectroscopy . . . 30
2.3.1 Laser cooling . . . 30
2.3.2 Matrix isolation . . . 31
2.3.3 Parahydrogen cryogenic crystals . . . 33

3 BaF ion beam production **37**
3.1 Ion source setup . . . 38
3.2 Magnetic field confinement . . . 40
3.3 Einzel lens analysis . . . 42
3.4 RGA 200 mass analysis . . . 46

4 Parahydrogen crystal production and characterization **54**
4.1 Cryogenic and optical system . . . 54
4.2 Crystal characterization . . . 56

Conclusions and Outlook **64**

References **66**

Abstract

In the physics beyond the Standard Model, one of the primary challenges is addressing the imbalance of matter and antimatter in the universe. Theories such as supersymmetry explain such discrepancy by predicting the existence of new high energy particles, with energy scale exceeding several tera-electron volts (TeV), out of reach of currently available particle accelerators.
Table-top experiments emerged as a promising approach to solve this issue. These experiments focus on high sensitivity measurement of the electron Electric Dipole Moment (eEDM) in polar molecules, as by detecting small changes in the electron's spatial charge distribution, it is possible to indirectly detect high energy particles that might influence it.
This thesis focuses on the development of an apparatus within the PHYDES collaboration for the production and spectroscopy of BaF-doped parahydrogen (p-H_2) cryogenic crystals. This combination, which has never been investigated before, is herein analyzed with the ultimate goal to perform eEDM measurements using the matrix isolation technique.
The work involved the design and construction of a molecular source capable of generating a barium monofluoride (BaF) ion beam, that has a great coherence time along with large internal effective field, both crucial parameters for a good sensitivity of eEDM measurements. The main components of the source will be analyzed to ensure efficient and stable production of approximately 10^{14} molecules per hour. Additionally, a cryogenic setup was analyzed to produce pure p-H_2, an isotope of hydrogen that will be used to host a large number of BaF molecules in a stable and inert environment with exceptional optical clarity. In this work, we stored and subsequently grew crystals of both H_2 and p-H_2, conducting spectroscopic analysis to measure their thickness and achieving a p-H_2 purity of approximately 97%.
While the complete integration of BaF into the p-H_2 matrix was not realized in this project, the apparatus developed has the potential to significantly improve the sensitivity of eEDM measurement, laying a solid groundwork for future investigations.

Chapter 1

Introduction

The Standard Model (SM) of particle physics is one of the most significant theories of our generation and has produced several outstanding discoveries in the field of particle physics [1, 2]. Developed in the latter half of the 20th century [3], the SM provides a solid framework for understanding the physics of fundamental particles like quarks, leptons, and gauge bosons [4], describing their interactions via the electromagnetic, weak, and strong forces. Moreover, it integrates quantum field theories and symmetries that led to the prediction, often followed by the discovery of previously unknown particles. The most notable example of the SM predictions is the Higgs boson, confirmed by experiments at the Large Hadron Collider (LHC) in 2012 with the ATLAS and CMS experiment [5, 6].
There are however open problems in the SM. Beyond the impossibility to incorporate gravity in its formalism [7], it fails to account for the observed matter-antimatter asymmetry in the universe [8]. This asymmetry arises from the CP violation, where C stands for charge conjugation and P for parity. CP violation is predicted by the Standard Model, however it is insufficient to explain the observed imbalance of matter-antimatter. This provides a major motivation to search for new sources of CP violation.

1.1 Electron Electric Dipole Moment - eEDM

supersymmetry and theories beyond the Standard Model (BSM) [9] predict additional particles at TeV energy scale, as schematized in Figure 1.1, whose existence can be probed with experiments searching for electric dipole moments (EDM) of electrons or nuclei beyond the LHC energy scales [10].
In the framework of the Standard Model, electron EDM arises due to CP violation, which is closely related to T violation through the CPT theorem. [11]. Due to the incomplete understanding of CP violation, the precise value of the SM expected eEDM is hard to compute. For instance, the Standard Model nicely explains the CP violation for K and B mesons decay [12, 13] through the Cabibbo-Kobayashi-Maskawa matrix [14], however the eEDM arises only at the four-loop level of perturbation theory and is predicted to be less than $d_e^{SM} < 10^{-38}$ e cm [15]. This very small values makes eEDM a challenging parameter to be measured, necessitating experiments of extraordinary sensitivity.
Tabletop experiments have proven to complement high energy collider experiments effectively. Leveraging AMO techniques to test fundamental symmetries and constants, they have shown great potential in detecting small signals that could indicate new forces beyond the Standard Model. However, given the SM prediction of eEDM, along with the current best experimental sensitivity of 4.1×10^{-30} e cm [16], all searches for the eEDM are expected to yield null results. Nonetheless, in BSM theories, especially in supersymmetric theories, the eEDM can appear at

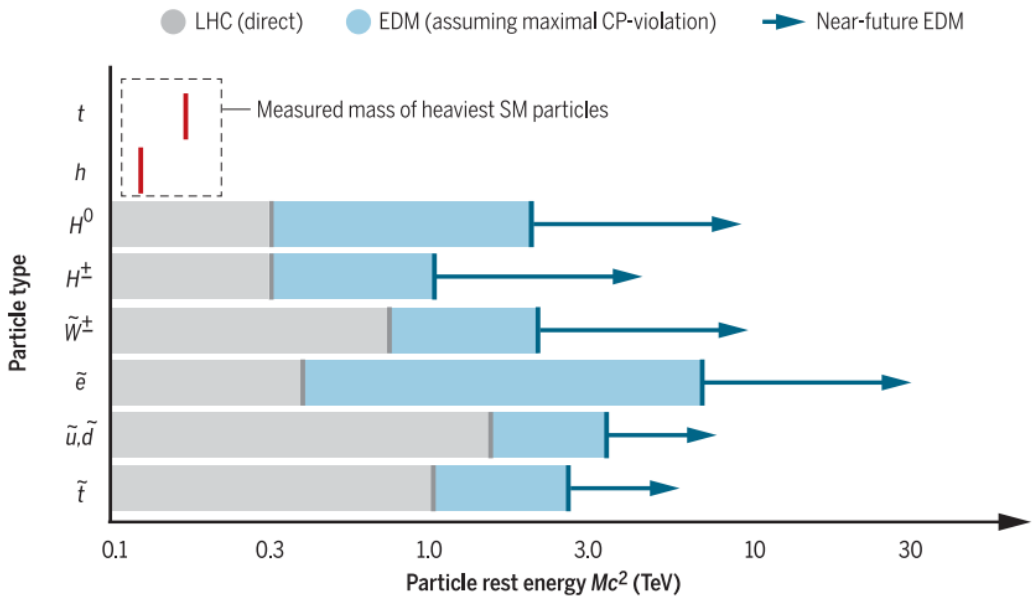

Figure 1.1: Overview of predicted particles along with the current energy limits of the experiments to find them. The red bars show the measured masses of the heaviest SM particles, the top quark (t) and Higgs boson (h). Although no particles BSM have been discovered, new experiments can exclude their existence below certain masses. The gray and blue areas indicate excluded ranges for hypothetical particles as additional Higgs bosons (H^0, $H^{\pm}$) and supersymmetric partners (denoted by tildes) of SM particles. Gray regions are ruled out by direct LHC searches, while blue regions are excluded by EDM experiments assuming maximal CP violation. Arrows indicate projected sensitivity for future EDM experiments. [11].

the one- or two-loop level, with required sensitivity closer to current experiments. An illustration explaining how new high energy particles might give rise to an electron EDM is shown in Figure 1.2, where the presence of a new high energy particle affects the space charge distribution of an electron, resulting in a permanent eEDM. Another possible assumption can be done by consid-

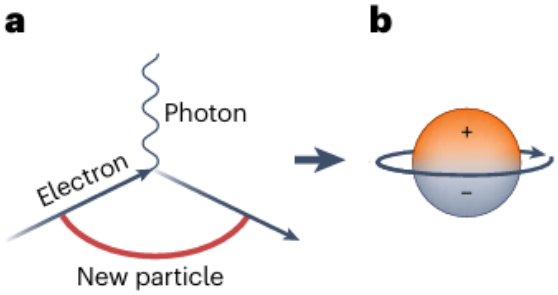

Figure 1.2: Illustration of interaction between new bSM high energy particle and an electron. **a**: New particles that mediate symmetry-violating forces might couple to the electron; **b**: The charge distribution becomes asymmetric, resulting in a permanent electron Electric Dipole Moment (eEDM), d_e, aligned with its spin axis [11].

ering neutrinos as Majorana particles [17]. This approach introduces new CP-odd phases in the lepton sector and permits non-vanishing two-loop contributions to the EDM, without requiring modifications to the SM. The resulting contribution to the eEDM could reach 10^{-33} e cm, three order of magnitude from the current eEDM best sensitivity.
To understand why eEDM requires P and T violation, one can consider an electron with electric dipole moment $\boldsymbol{d}$ and magnetic dipole moment $\boldsymbol{\mu}$. Both moments will align with the spin direc-

tion, since it is the only vector available to orient the particle. The Hamiltonians H_M and H_E that describe the interactions of the electron with a magnetic field $\mathbf{B}$ and an electric field $\mathbf{E}$ are, in the non relativistic regime, respectively:

$$H_M = -\boldsymbol{\mu} \cdot \mathbf{B} = -\mu \boldsymbol{\sigma} \cdot \mathbf{B} \tag{1.1}$$

$$H_E = -\boldsymbol{d} \cdot \mathbf{E} = -d \boldsymbol{\sigma} \cdot \mathbf{E} \tag{1.2}$$

where $\boldsymbol{\sigma}$ is the Pauli spin operator. Under a parity transformation, the axial vectors $\boldsymbol{\mu}$ and $\mathbf{B}$ remain invariant, while the polar vector $\mathbf{E}$ changes sign. Under a time reversal transformation, $\mathbf{E}$ remains invariant, but $\boldsymbol{\mu}$ and $\mathbf{B}$ change sign. Consequently, while H_M is invariant under both parity (P) and time reversal (T) transformations, H_E is invariant under none of them and will contribute with a change in energy of the state.

1.1.1 Detecting an eEDM - Schiff's theorem

To detect an eEDM, one might consider to place an electron in a uniform external electric field, $\mathbf{E}_e$ and observe a change in energy proportional to it. However, this approach is impractical for a free electron, which would quickly be accelerated out of the observation region. Alternately, researchers have attempted to measure d_e through the observation of linear Stark effects in a paramagnetic atom [18] or molecule [19], with an effect similar to the one shown in Figure 1.2, arising from an electric dipole moment of the unpaired electron.
However, according to the Schiff's theorem, there can be no first order linear Stark effect and any measurable EDM should vanish in the non-relativistic limit of quantum mechanics [20]. Physically, this means that when an external field is applied to an atom or molecule, the Schiff screening takes place, meaning that the internal field will cancel the external field, fully screening it. However, as first demonstrated by Sandars [21], Schiff's theorem does not apply when relativistic effects are taken into account.
This can be seen by considering the Dirac equation for an electron in a central potential, given by:

$$H = c\boldsymbol{\alpha} \cdot \mathbf{p} + mc^2\gamma^0 - e\left(\phi_i + \phi_e\right) \tag{1.3}$$

where $\boldsymbol{\alpha}$ and γ are the Dirac matrices, $\mathbf{p}$ is the relativistic momentum, ϕ_i is the internal electrostatic potential, and ϕ_e is the external electrostatic potential.
The single particle perturbation Hamiltonian corresponding to the contribution of the electron EDM, under the influence of an electric field $\mathbf{E}$, when $\mathbf{B} = 0$ is:

$$H_{\mathrm{EDM}} = -d_e\gamma^0\boldsymbol{\Sigma} \cdot \mathbf{E} \tag{1.4}$$

where $\boldsymbol{\Sigma} = \mathbf{I} \cdot \sigma$ are the Pauli matrices. This equation can be rewritten by separating the contribution from the relativistic effects as:

$$H_{\mathrm{EDM}} = -d_e\gamma^0\boldsymbol{\Sigma} \cdot \mathbf{E} - d_e(\gamma^0 - 1)\boldsymbol{\Sigma} \cdot \mathbf{E} \tag{1.5}$$

The first term on the right-hand side corresponds to the non-relativistic limit, which does not contribute to the first-order energy shift according to Schiff's theorem. This is due to its null expectation value $\langle\psi| - d_e\gamma^0\boldsymbol{\Sigma} \cdot \mathbf{E}|\psi\rangle = 0$ for an eigenstate $|\psi\rangle$.
On the other hand, the second term does contribute to the energy shift, leading to a non-zero EDM. This term arises from the relativistic nature of the electron's motion, specifically the contribution of the Dirac matrices in the presence of an external electric field.
The first order energy shift contribution ΔE is:

$$\Delta E = \langle\psi| - d_e(\gamma - 1)\boldsymbol{\sigma} \cdot \mathbf{E}|\psi\rangle \neq 0\,. \tag{1.6}$$

It is thus clear that while the average electric field may vanish in the non-relativistic limit, it does not do so when relativistic corrections are included.
The electron's motion in heavy atoms or molecules can indeed give rise to contributions to the eEDM, as a relativistic electron does not experience a purely electrostatic force, but rather a combination of electric and magnetic fields.
A dipole moment with velocity $c\boldsymbol{\beta}$ under the influence of an electric field $\mathbf{E}$ will undergo Lorentz contraction in the laboratory frame (d_e^L), mainly:

$$d_e^L = d_e - \frac{\gamma}{1+\gamma}\boldsymbol{\beta} d_e \cdot \boldsymbol{\beta} \,. \tag{1.7}$$

The relativistic enhancement of the EDM is particularly pronounced in systems with high atomic number Z, as the enhancement scales approximately with Z^3. This scaling is due to the stronger relativistic effects in heavier elements, where the inner electrons move at speeds comparable to the speed of light.
From equation 1.7 one can define, using a central field approximation and a few assumptions, the non-classical energy shift as:

$$\Delta E = -d_e \left\langle \psi_A \left| \boldsymbol{\sigma} \cdot \mathbf{E} \left[1 + \frac{p_{cl}^2}{2(mc)^2} \right] - \frac{1}{4m^2c^2} \left[\mathbf{p} \cdot \mathbf{E} \cdot \mathbf{p} + \mathbf{E} \cdot \mathbf{p} \cdot \boldsymbol{\sigma} \cdot \mathbf{p} \right] \right| \psi_A \right\rangle \tag{1.8}$$

which includes a correction term that accounts for the particle's relativistic momentum $p_{cl}^2/(2mc)^2$ and an additional correction term involving the interaction between the momentum and electric field components.
Therefore, measuring an electron EDM is possible despite of Schiff's theorem, and is a direct consequence of the relativistic nature of the electron's motion in heavy atoms or molecules.

1.2 eEDM measurements with molecules

In all atoms and molecules, CP violations (CPV) effects become apparent by measuring energy shifts when an electric field (E) is applied to the system. This effect can be described by a term in the atomic or molecular Hamiltonian as:

$$H_{CPV} \propto \mathbf{S} \cdot \mathbf{n} \tag{1.9}$$

where $\mathbf{S}$ represents the electron spin. The polar vector $\mathbf{n}$ is aligned with E, which polarizes the atom or molecule as $\mathbf{n} = P(E)\hat{E}$, where $\hat{E}$ is the unit vector along the applied field, and $P(E)$ (with values from 1 to -1) represents the dimensionless electrical polarization of the atom or molecule.
As previously mentioned, not only can the Schiff screening be overcome in the relativistic regime, but electrons moving near high Z (heavy) nuclei are subjected to an effective internal electric field (E_{eff}) orders of magnitude grater than the external electric field. This is a crucial parameter that makes atoms, and especially polar molecules, an ideal setup to study and detect eEDM with high sensitivity.

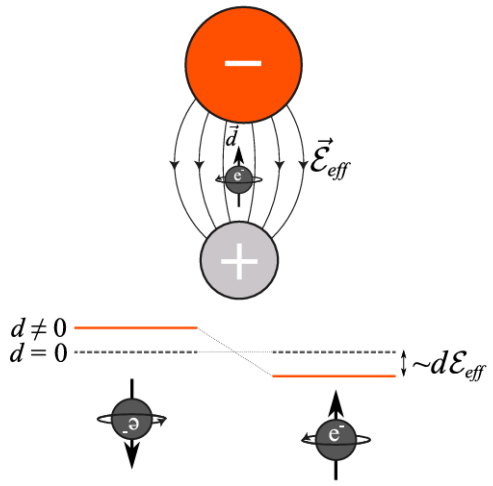

Figure 1.3: A simple illustration of the consequence of a non-zero eEDM on the energy splitting of the molecular quantum state. If $D \neq 0$, the energy shift will be proportional to $d_e E_{\text{eff}}$ [22].

A representation of how the energy shifts associated with H_{CPV} can be measured is shown in Figure 1.3. In this scenario, an unpaired valence electron in a polar molecule experiences the effective internal electric field E_{eff}, leading to an energy splitting $\Delta E \propto d_e E_{\text{eff}}$. The polarization axis $\mathbf{n}$, and hence E_{eff}, is aligned with the externally applied field E_{lab}, while $d_e \propto \mathbf{S}$. Here a fully polarized molecule ($P = 1$) is depicted.
Polarization arises by applying an external field that produces a Stark-induced mixing of opposite parity energy levels (i.e. $|+\rangle$ and $|-\rangle$). Complete mixing of the states corresponds to $|P| = 1$. Assuming a valence electron in the s orbital of an atom, to reach full polarization a $E \approx 0.1e/a_0^2$ is required, with a_0 Bohr radius, thus an $E_{\text{lab}} \approx 1$ GV/cm, far from current laboratory produced electric fields. With current laboratory electric field ($E_{\text{lab}}^{\max} \approx 300$ GV/cm), a polarization of $P \approx 10^{-4}$ is typically achieved. On the other hand, in polar molecules, the internal field from the negative ion acting on the positive ion naturally has a magnitude of e/a_0^2, so an s-orbital of the positive ion can be fully polarized [23].
However, in the absence of any externally applied field, the molecular eigenstates are also eigenstates of angular momentum, meaning there is no preferred orientation of one ion relative to the other. A sufficiently strong applied E-field can mix rotational states of opposite parity (e.g., $|+\rangle = |J = 0\rangle$ and $|-\rangle = |J = 1\rangle$) and orient the molecular axis, thus the internal E-field along it. The energy splitting of such molecular rotational states is typically smaller than 10^{-4} eV, thus is sufficient to apply an external field smaller than 100 kV/cm to reach $P \approx 1$. This is the reason why molecular systems typically have CPV-induced energy shifts 10^3 to 10^4 times larger than those in atoms, where there is no internal field.
Generally, the CPV induced energy split ΔE_{CPV} is described by:

$$\Delta E_{CPV} = Q(C_{CPV}) \times P(E) \tag{1.10}$$

where $Q(C_{CPV})$ is the intrinsic sensitivity of the system [24]. For a system of atoms or molecules, this can be written as a product of four factors:

$$Q(C_{CPV}) = Q_{at}(C_{CPV}) \times Q_{nuc}(C_{CPV}) = S_{at}^{C_{CPV}}(Z) q_{at} \times S_{nuc}^{CPV}(Z) q_{nuc} \tag{1.11}$$

Here, the subscript at corresponds to effects associated with atomic/molecular/ionic structure, and nuc to effects of nuclear structure. The factors $S_{at}^{CPV}(Z)$ are associated to electron-nucleon interaction and grows rapidly with Z (approximately Z^3 for paramagnetic systems), while

$S_{nuc}^{CPV}(Z)$ depends on the atoms and grows linearly with Z. The factors q depend on the detailed structure of the electronic or nuclear state in the system. For paramagnetic systems in which the investigated parameter is related to the electron spin, like d_e, $Q_{nuc}(C_{CPV}) = 1$ since they are not dependent from the nuclear spins.

eEDM measurement

Molecular eEDM research usually rely on coherent precession of electrons in an internal effective field of the molecule. The eEDM sensitivity factor [22] of such researches is given by:

$$\sigma(d_e) \approx \frac{1}{PE_{\text{eff}}\sqrt{N}\tau} \tag{1.12}$$

Where P is the polarization, N is the number of molecules investigated and τ is the coherent interaction time.
In the next following chapters, we will discuss how these parameters have been carefully considered in the construction of our eEDM detection setup using the matrix isolation technique. For instance, the choice to work with barium monofluoride (BaF) molecules has been done for its large internal effective field of $E_{\text{eff}} \approx 4 - 7$ GV/cm [25, 26]. Although higher effective field can be reached with molecules such as ThO and YbF, with 71.3 and 20.8 GV/cm respectively [25], the lower mass of BaF allows for better optimization and deceleration of the molecular beam. Moreover, BaF might ensure a long coherence time within a cryogenic matrix, a crucial parameter that must be investigated in future experiments to analyse how the crystal structure might effect it.
A block diagram of the full experimental apparatus planned for eEDM measurements at LNL laboratories is shown in Figure 1.4. In this thesis work, the production of BaF has been addressed through the development and characterization of a plasma ion source. Laser ablation is another method that could be used to develop molecular sources, offering greater stability compared to plasma ion sources. This method is under study in our group, in collaboration with the group of Prof. Steven Hoekstra at the Groningen University. The investigated source generates a molecular beam, which will be controlled through an Einzel lens and magnetic fields to maximize molecular density at the crystal growth site. In future experiments both a decelerator and mass filter will be included. A filter ensures a pure doping of the crystal, as molecular beams usually contain a large quantity of extra gases that could create defects in the crystal. A decelerator will be needed as ion sources generate molecules at approximately 10 km/s and with such energies both the crystal and the molecule bond will break. Afterwards the beam will be ideally directed into a crystal growth chamber to create a BaF-doped cryogenic crystal.

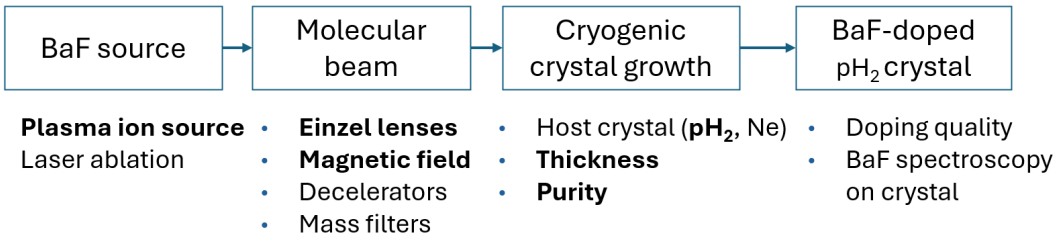

Figure 1.4: Block diagram of the full apparatus for eEDM measurements with BaF molecules in parahydrogen crystals. In this thesis work, the parts highlighted in bold have been studied.

Parahydrogen (p-H_2) has been selected for as it could offer favorable properties such as optical clarity and minimal perturbation over the guest molecules, promising to result in longer coherence times for the guest molecules [27]. Although a doped crystal has not been produced during this work, an experimental study of the methods for pH crystal production has been devised, focusing

on the purity and growth rate. As it will be detailed in the following, during the growth process it is possible to monitor both the crystal purity and thickness through acquisition of spectra at Fourier Transform Infrared interferometer (FTIR). The ability to produce a high density crystal with a small number of defects is essential for maximizing the sensitivity of the experiment. Tests on neon matrices will also be conducted, as for this matrix studies about its influence on guest BaF molecules are available in the literature [28].

1.3 State of the art

An overview of the eEDM limits set by the most relevant experiments in the past 20 years is shown in Figure 1.5.

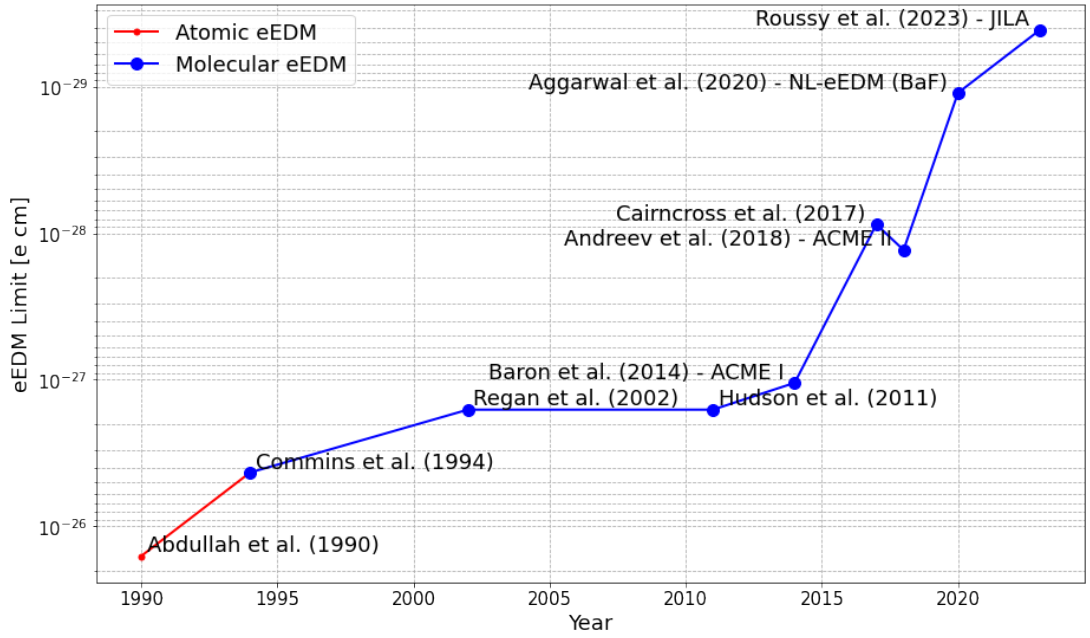

Figure 1.5: Evolution of the sensitivity of eEDM measurements over the years. The first two measurements used atoms, while the remaining ones utilized molecules to leverage their large effective electric field.

Recent advancements have been made in the precision measurement of the eEDM using methods that involve trapping and manipulating heavy polar molecules [29] or molecular ions [30]. Molecules are particularly advantageous because they can generate very large effective electric fields (E_{eff}) at the location of the electron, greatly amplifying the potential eEDM signal. The most precise measurements of the eEDM has been reported by the team at JILA, University of Colorado Boulder [16]. In this experiment, the researchers improved upon previous eEDM bounds by a factor of approximately 2.4, achieving an upper limit of $|d_e| < 4.1 \times 10^{-30}$ e cm with 90% confidence. This was accomplished using molecular ions of HfF^+, where the electrons are subjected to a large intramolecular electric field of $E_{\text{eff}} \approx 23$ GV/cm , approximately 10^5 times larger than what can be applied in a laboratory, allowing the eEDM to be probed with high sensitivity.
The measurement relies on quantum projection-noise-limited spectroscopy of molecular ions confined in a radio frequency trap, shown in Figure 1.6, image B. The experiment begins with the production and trapping of approximately 20,000 HfF^+ ions, oriented in space by applying a rotating electric bias field ($\vec{E}_{\text{rot}}$) at an angular frequency of $\omega_{rot} = 2\pi \times 375$ kHz. The orientation of the molecules with respect to this field allows the researchers to control the internal electric field that the valence electron experiences. Moreover, the ions are under the influence of

a quadrupole magnetic field gradient to create a time-averaged effective bias magnetic field $\vec{B}_{\text{rot}}$. The energy levels of the molecular ions are manipulated and probed using Ramsey spectroscopy. The core idea is to measure the energy shift when the electron spin is aligned and anti-aligned with the effective electric field, as it is directly related to the eEDM. The specific energy levels used in the experiment are the $^3\Delta_1$ states of the molecule, which are split into doublets in the presence of the applied electric and magnetic fields, as shown in Figure 1.6, image A. The energy

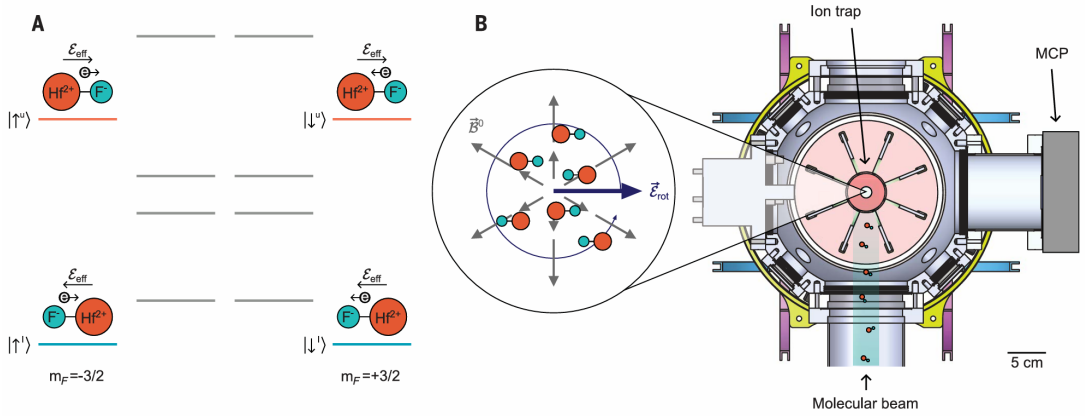

Figure 1.6: **A**: Illustration of the level structure of HfF^+ ions in the eEDM-sensitive state $^3\Delta_1$ ($v = 0, J = 1$). .The horizontal axis indicates the projection of the total angular momentum m_F onto the externally applied electric field, which also orients the internal effective electric field of $E_{\text{eff}} \approx 23$ GV/cm. The vertical axis indicates the energy of the states. **B**: Schematics of the ion trap used in the experiment [16].

difference between the states in each doublet is measured by preparing the system in a superposition of these states through a $\frac{\pi}{2}$ pulse, allowing them to evolve over time. Such difference is sensitive to eEDM-induced energy shifts of $\pm 2 d_e E_{\text{eff}}$, allowing the eEDM value to be extrapolated. Moreover, the doublets have opposite magnetic moments, resulting in the cancellation of the Zeeman splitting, which corresponds to approximately $\mu_B B_{\text{rot}}$ and is the largest contribution to the energy splitting.

The system is allowed to evolve over a set period, during which the superposed states acquire a relative phase difference due to their energy separation. To convert the accumulated phase difference into a measurable quantity, a second $\frac{\pi}{2}$ Ramsey pulse is applied to convert the accumulated phase difference into a population difference between the states. This quantity can be measured by state-selective photo-dissociation by counting the resulting Hf^+ ions [31]. The accumulated phase defines where the ions will be detected, as shown in Figure 1.7, image A, where $N^{u/l}_{In/Anti}$ are the number of ions counted in the different states. The experiment is repeated for different initial spin states and for various free-evolution times, generating pairs of Ramsey fringes, as shown Figure 1.7, image B. The frequencies of these fringes correspond to the energy splitting of the doublets.

To mitigate noise and systematic errors, the experiment is designed to be highly differential. For instance, the measurement is performed simultaneously on spatially overlapping clouds of ions in both doublets, which allows the researchers to subtract common-mode noise. Unpredictability in magnetic field gradients, electric field distortions, and other technical imperfections, such as imperfect spatial overlap of the ion clouds, negatively affect the measurement. However, the total systematic uncertainty was determined to be 6.9 μHz, smaller than the statistical uncertainty. The eEDM signal frequency f^{DB} detected is $f^{DB} = -14.6 \pm 22.8_{\text{stat}} \pm 6.9_{\text{syst}}$ μHz. Dividing by $-2E_{\text{eff}}\frac{\text{sgn}(g_F)}{h}$, where g_F is the g factor of the state, the eEDM results in:

$$d_e = (-1.3 \pm 2.0_{stat} + \pm 0.6_{syst}) \times 10^{-30} \text{e cm} \tag{1.13}$$

consistent with zero within one standard error. Here the label stat and syst refers to statistical

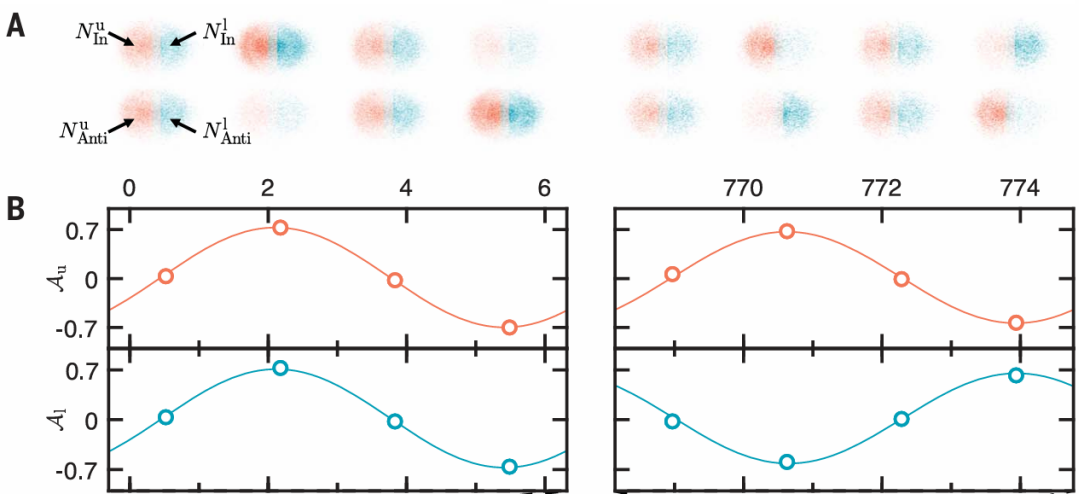

Figure 1.7: **A**: Detection of Hf^+ ions: ions are classified into the upper or lower doublet based on their position (upper doublet in orange, lower doublet in blue). **B**: Asymmetries for the upper and lower doublets are collected into Ramsey fringes. [16]

and system error respectively.
The work by the JILA team represents the current state of the art, setting the most stringent constraints on the eEDM to date. Moreover, if one considers theories such as supersymmetry, two-Higgs model or left-right symmetric models, the eEDM at the one-loop level [32] is:

$$d_e = \frac{e a_0 \alpha g^2}{4\pi} \sin\phi_{CP} \frac{m_e^2}{M^2} \tag{1.14}$$

where M is the mass of a new predicted particle with coupling strength g, ϕ_{CP} is the phase describing how strongly the CP symmetry is being violated and α is the fine structure constant. With a few assumption over g and ϕ_{CP}, this new limit can be interpreted as ruling out the presence of new particles with masses of:

$$M \geq \left(\frac{g}{\alpha^{\frac{1}{2}}} \right) 40\text{TeV} \tag{1.15}$$

Considering $g \approx \alpha$, this limit is one order of magnitude grater than the largest possible particle that can be detected at the LHC [33].

1.4 eEDM measurements with matrix isolation of BaF

The readout technique described in Section 1.3 is not applicable in the context matrix isolation. It is however possible to directly readout the accumulated phase with high sensitivity, as devised in the work by A. Vutha et al. [34]. As shown in Figure 1.8, this method entails seven steps to perform one measurement cycle for BaF molecules trapped in a rare-gas matrix. Throughout the process, a small bias magnetic field $B_Z\hat{Z}$ is applied along one axis of the crystal. Molecules of BaF are already oriented by the crystal structure, therefore no electric field is applied during the experiment, except in step (f), where the Stark shift in the hyperfine structure is utilized to differentiate between oppositely oriented molecules.

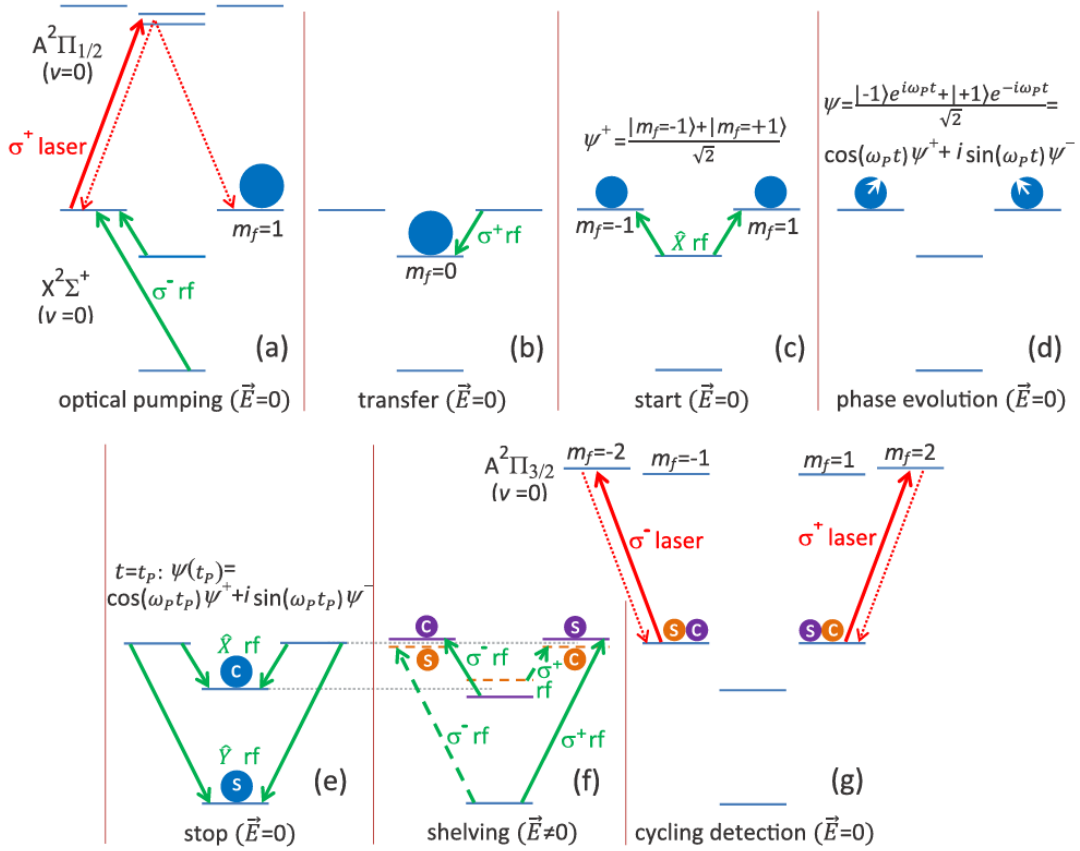

Figure 1.8: Scheme for measuring the electron Electric Dipole Moment using $^{138}Ba^{19}F$ molecules in a rare-gas matrix at 3 K. The molecules thermalize into four $X^2\Sigma^+$ hyperfine states and the following 7 steps can be applied to measure the eEDM. (a): They are optically pumped and coupled via RF fields into the $X^2\Sigma^+ m_f = +1$ state. (b) This population is transferred to the $m_f = 0$ state. (c) Then into ψ^+, an even superposition of $m_f = -1$ and $m_f = +1$ states. (d) The phases of ψ^+ components evolve over a time t_P. (e) After this period, ψ^+ and ψ^- components are transferred into two $m_f = 0$ states. (f) From these states, the population is moved into $m_f = -1$ and $m_f = +1$ states using appropriate RF fields. This step is performed with an applied electric field $E_Z\hat{Z}$, allowing distinct frequency-resolved transitions for molecules oriented in the $+\hat{Z}$ and $-\hat{Z}$ directions. These transitions make the scheme insensitive to magnetic fields and double the sensitivity to d_e. (g) Finally, the $m_f = -1$ and $m_f = +1$ populations are measured by exciting them with σ^- and σ^+ laser transitions, respectively, and detecting the resulting fluorescence. The ratio of fluorescence for σ^- and σ^+ provides a measurement of d_e. [34]

Prior to the steps shown in Figure 1.8, a rare-gas crystal embedded with $^{138}Ba^{19}F$ molecules is prepared. At a temperature of approximately 3 K, all the atoms thermalize into the ground electronic, vibrational, and librational states, as well as the ground state for the molecule's center-of-mass motion.

Initially, the four hyperfine states possess equal populations. In step (a), the population can be optically pumped into the $X^2\Sigma^+ m_f = +1$ state using σ^+ circularly polarized laser light, tuned to the $A^2\Pi_{1/2}$ state. Given that electronic transitions within the matrix are typically broadened beyond their natural width in a free molecule, the hyperfine structure remains unresolved. However, for σ^+ polarization, the $X^2\Sigma^+ m_f = +1$ state is a dark state, as no $m_f = +1$ transitions exist for the σ^+ laser driving to the $A^2\Pi_{1/2}$ state, causing the population to accumulate in this state. The σ^+ laser light does not strongly couple the two $m_f = 0$ hyperfine states to the $A^2\Pi_{1/2}$ state, necessitating σ^- rf fields to couple these states to the $m_f = -1$ state. Consequently, at the end of step (a), the majority of the population resides in the $X^2\Sigma^+ m_f = +1$ state.

In step (b), this population is transferred to one of the $X^2\Sigma^+ m_f = 0$ states using a σ^+ rf π pulse.

The population is then moved into an even superposition of the $X^2\Sigma^+ m_f = -1$ and $m_f = +1$ states:

$$|\psi^+\rangle = \frac{|m_f = -1\rangle + |m_f = +1\rangle}{\sqrt{2}} \tag{1.16}$$

This is achieved using $\hat{X}$-polarized rf fields, as depicted in panel (c).
The energies of the $m_f = +1$ and $m_f = -1$ states shift by $+\hbar\omega_P$ and $-\hbar\omega_P$, respectively, due to the applied magnetic field and the effective electric field within the aligned molecules. For molecules oriented in the $\pm\hat{Z}$ directions, $\omega_P = (g\mu_B B_Z \pm d_e E_{\text{eff}})/\hbar$ represents the precession frequency caused by the interaction of the magnetic moment $g\mu_B$ with the magnetic field, and d_e with the effective electric field. Thus, at the conclusion of the phase evolution step, the state is expressed as:

$$|\psi(t_P)\rangle = \cos(\omega_P t_P)|\Psi^+\rangle + i\sin(\omega_P t_P)|\Psi^-\rangle \ . \tag{1.17}$$

The stop pulse in (d) uses $\hat{X}$-polarized rf to transfer the Ψ^+ component of $\Psi(t_P)$ to one of the $X^2\Sigma^+ m_f = 0$ states, and $\hat{Y}$-polarized rf to transfer the Ψ^- component to the other $m_f = 0$ state. The two resulting populations $s = \sin^2(\omega_P t_P)$ and $c = \cos^2(\omega_P t_P)$ can then be used to measure the phase progression.
In step (f), an electric field is applied along the $\hat{Z}$ axis of the crystal structure, causing the hyperfine structure splittings to differ slightly between molecules oriented in the $+\hat{Z}$ and $-\hat{Z}$ directions, thus enabling the rf transitions to address them separately. The population is moved from the two $X^2\Sigma^+ m_f = 0$ states into the $X^2\Sigma^+ m_f = \pm 1$ states. For the $-\hat{Z}$ molecules, the population from one $m_f = 0$ state is transferred to the $m_f = +1$ state, while $\hat{Z}$ molecules undergo the opposite transitions, to the $m_f = -1$ state.
The population in the $X^2\Sigma^+ m_f = -1$ state is detected in step (g) by exciting the $X^2\Sigma^+(m_f = -1)(v = 0)$ to $A^2\Pi_{3/2}(m_f = -2)(v = 0)$ transition using σ^- circularly polarized laser light, and observing the resulting fluorescence. Following this measurement cycle, most molecules will reside in $X^2\Sigma^+(v > 0)$ states.
The magnetic field B_Z and precession time t_P are chosen such that the total precession angle $\omega_P t_P$ is approximately $\omega_P t_P \bmod 2\pi = \delta + \pi/4$, where $\delta = \delta_B \pm \delta_E$, respectively the contribution of the magnetic field and eEDM ($\delta_E = d_e E_{\text{eff}} t_p/\hbar$). The ratio of the population in $m_f = -1$ to that in $m_f = +1$ is then $f_+(1 - 4\delta_+) + f_-(1 + 4\delta_-)$, where the contributions from δ_B cancel in the ratio, isolating the effect of d_e and making the measurement insensitive to magnetic field drifts.
The statistical uncertainty δ_{d_e} of a measurement using this method is influenced by the volume of the crystal, the density of BaF, and the number of experimental cycles. With ideal parameters, such as approximately 10^{13} molecules aligned along $\hat{Z}$, the BaF eEDM sensitivity δ_{d_e} in Argon [34] is estimated to be :

$$\delta_{d_e} \approx 1 \times 10^{-34} \text{e cm} \sqrt{\frac{1\ \text{cm}^3}{V}} \sqrt{\frac{1\ \text{month}}{T_{\text{measure}}}} \tag{1.18}$$

where V is the volume of crystal and T_{measure} is the period of data collection cycles.
The experimental setup described in this work is designed to create a highly controlled environment for the study of a large number of BaF molecules, which could enhance the statistical sensitivity of eEDM following the above described scheme. In the following chapters, each component of the apparatus will be examined in detail, with an emphasis on their contributions to the overall experimental sensitivity.

Chapter 2

Molecular sources

Precise experiments, such as those required for eEDM measurements, require a careful selection and consequent optimization of the molecular sources. This chapter examines the two principal molecular beam sources: plasma discharge ion sources and laser ablation coupled with buffer gas cooling.
Plasma ion sources are well known to produce high quantity of molecules, a crucial parameter for eEDM sensitivity, especially within the matrix isolation technique, further discussed in the chapter. Furthermore, an analysis of how laser ablation generates hot molecular species is given, along with cooling techniques allowing these molecules to reach temperatures suitable for precision spectroscopy measurements.

2.1 Plasma ion source

In this section, we will examine the main characteristics and operational functions of an oven source with plasma discharge for ion beams. The primary advantage of this source, compared to buffer gas-cooled sources, is the production of a very high intensity beam. When combined with a decelerator in a setup to dope cryogenic crystals, this source can potentially achieve an unprecedented number of molecules for investigation.
The development of ion sources has seen a significant advancement since the beginning of the last century. Many kind of ion sources have emerged for scientific purposes and technological applications. An overview of the principles, design, and operation of plasma ion sources will be given in this section. This method has proven to be highly effective in creating high current beams of metal ions, as evidenced by the widespread use of vacuum arc ion sources in laboratories worldwide [35]. Moreover, its versatility has been proven by the production of ion beams from over 50 different solid metals.
In this work we will focus on the plasma discharge technique, from which we aim to create a reliable and efficient method for producing ionized BaF molecules, thereby expanding the utility of vacuum arc ion sources beyond their traditional metal ion scope.
In general, an ion beam source consists of the ionizer, in which the ions are generated, and of an electrode system for ion extraction, acceleration and focusing. If a beam of neutral molecules is required, neutralization techniques need to be implemented after the formation of the ion beam. The ionizer can operate using gaseous elements, compounds, liquids, or solids. These materials are then vaporized through various methods, including external or internal ovens, plasma heating, ion beam sputtering, laser ablation, or vacuum-arc ablation. If one aims to obtain a beam of positive ions several processes can be used such as thermal ionization [36], contact-ionization [37] and other techniques.
The formation of the plasma usually begins through Helium, Argon [38], or more in general a

noble gas undergoing a gas discharge, which occurs when an electric current passes through a gas, ionizing it and creating a plasma. This process is influenced by several factors, including the type of gas, pressure, and applied voltage. An important aspect of many gas discharges is the formation of a space charge layer or sheath, a non-neutral plasma region near the electrodes. This phenomenon negatively influences ion beam production and will be taken into account later in this section.
The gas discharge can be triggered by DC or AC high frequency voltage. In this section we will only delve into the first one.

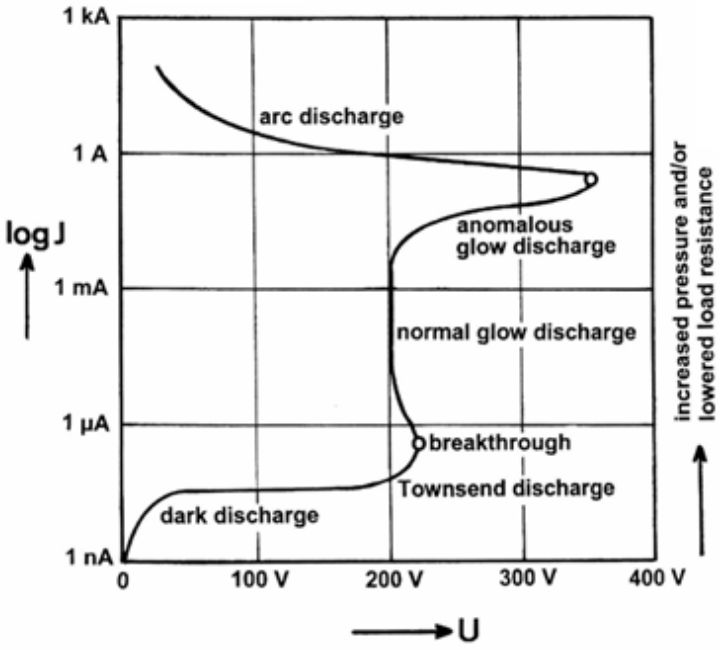

Figure 2.1: Current-voltage characterization of a DC-discharge with cold or heated cathodes, where U is the voltage between the two electrodes and J is the plasma current on the electrodes [39].

A characterization of a DC-discharge is displayed in Figure 2.1, showing the behaviour of the plasma. The plot shows all the stages of a plasma discharge, which are determined by the ion current J and the voltage between cold electrodes U. The first stage is the so called dark discharge where, at low pressure, a low voltage is applied between the electrodes and a current of few hundreds nA can be measured. A current saturation regime while increasing the voltage is reached until around 200 V, when free electrons in the chamber are accelerated toward the positive electrode and ions are accelerated toward the negative electrode. Accelerated electrons will collide with neutral gas atoms, causing excitation or ionization. This ionization creates additional ions and electrons, which are further accelerated by the electric field, leading to more ionization events. This is a cascade process known as Townsend breakdown, that leads to a rapid increase in electron density and eventually generating avalanches, resulting in the formation of a plasma. At a breakthrough point, which is dependent both on gas parameters and electrodes distance, the plasma enters the glow discharge regime. Here the breakdown voltage causes sudden gas ionization, creating a self-sustaining discharge where the current is limited by the glow itself, resulting in a voltage drop region. Glow discharges are further divided into normal and abnormal types based on current density, where the latter one is reached with an increasing pressure and a fall in the cathode potential. Secondary electrons are now being emitted by the cathode due to ion impact and the measured plasma current is of the order of mA.
Operating at even higher pressures and currents compared to glow discharges, arc discharges exhibit a decreasing current-voltage characteristic, where the voltage across the discharge decreases

as the current increases. This behavior is due to a significant increase in cathode temperature, leading to thermionic emission from the electrodes which will become the dominant process. The increasing cathode temperature can also be achieved by maintaining the same current values while lowering the load resistance of the apparatus driving electric circuit. Variants of DC

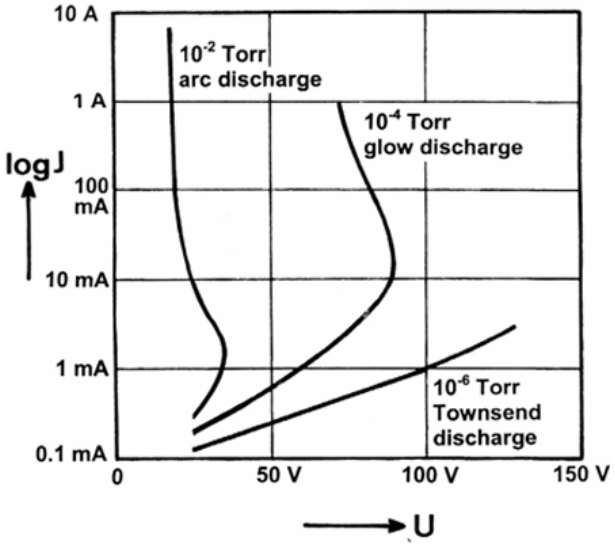

Figure 2.2: Current-voltage characterization of a filament driven DC-discharge with thermionic cathodes. For different pressures, the voltage between the two electrodes is noted with U, while J is the ion current.

discharges are achieved when thermionic cathodes are utilized. Since thermionic cathodes require electrical heating, all filament-driven discharges are non-self-sustaining, therefore plasma discharge will follow a different behaviour, shown in Figure 2.2.
Depending on the gas pressure, filament-driven sources can exhibit characteristics of arc discharges (10^{-2} mBar), glow discharges (10^{-4} mBar) or Townsend discharges (10^{-6} mBar). In the setup used in the present thesis work, that will be detailed in Chapter 3, the discharge was achieved in the arc discharge regime with thermionic cathodes.
The ion current J_i produced in this method is given by:

$$J_i = J_e n_0 q_I l \tag{2.1}$$

where J_e is the electron current, n_0 the gas density q_I the ionization cross-section and l the electron path length. A plot of the ionization cross section vs electron energy is given in Figure 2.3 for different gas species and ionization degree. The cross section strongly depends on the electron velocity, and therefore on the ionization energy W_I and interaction time Δt. The maximum cross section is achieved when the energy equation $W_I \cdot \Delta t = \hbar$ holds true [39], thus when the electron velocity is:

$$v_{e,opt} = W_I \frac{d}{\hbar} \tag{2.2}$$

For the purpose of this work, a He gas discharge was preferred. At parity of electron energy He has a smaller cross section compared to other gases, which results in a higher electron energy needed to activate the plasma. Nonetheless, since its energy will be greater, it will result in more efficient ionization of the molecule of interest (BaF).
The plasma in a gas discharge is not uniformly distributed. The cathode region, known as the cathode sheath, is characterized by a strong electric field and a significant voltage drop (cathode fall). The cathode sheath plays a crucial role in sustaining the discharge by accelerating ions toward and into the cathode, which release secondary electrons upon impact, further sustaining

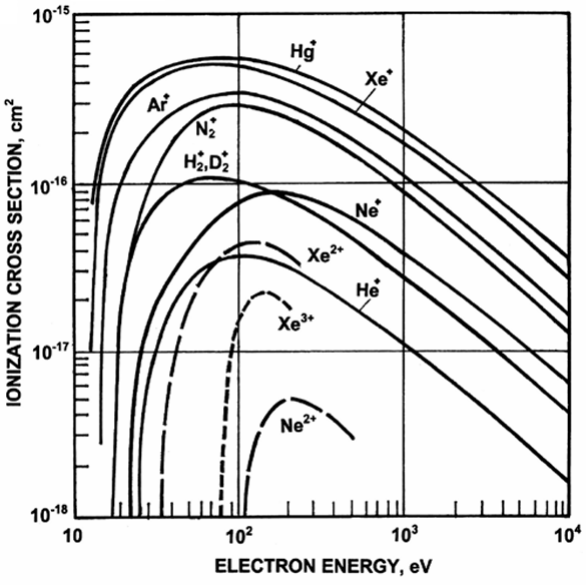

Figure 2.3: Ionization cross section (cm^2) by single electron impact energy (eV) for different ionizing gasses.

the discharge. The region between the cathode sheath and the anode, known as the positive column, is nearly neutral with a high plasma density. Most ionization and excitation processes occur in this region. The properties of the positive column, such as electron temperature and density, determine the characteristics of the ion beam extracted from the ion source. Likewise, the plasma striking into the anode maintains the current necessary to sustain the plasma discharge. Most importantly, the anode usually has a central hole, where the plasma plume that streams through is utilized to form the ion beam. Extracting ions from a plasma can be done by applying a voltage V_{ex} between the plasma holder and the extractor electrode (anode). The extraction velocity of the plasma entering the extraction region is given by:

$$v_0 \geq \sqrt{\frac{k_B T_e}{m_i}} \tag{2.3}$$

where T_e is temperature of the plasma electrons and m_i is the ion mass in amu.
In the presence of space-charge limitations, the ions current is described in the framework of the Langmuir-Schokkty-Child's prediction [40] through the expression:

$$I = \frac{4}{9}\epsilon S \left(\frac{2q_i}{m_i}\right)^{1/2} \frac{V_{ex}^{\frac{3}{2}}}{d^2} \tag{2.4}$$

where S is the extraction open area, q_i the ion charge and d is the extraction gap. If low energy ions are needed, i.e. $U < V_{ex}$, a decelerator is installed after the extraction zone. Introducing a modest longitudinal magnetic field in the extraction region can effectively control the amount of plasma transported from the cathode to the extractor. An illustration showing the principle of this mechanism is shown in Figure 2.4. Without a magnetic field, a significant portion of the plasma would be lost to the walls. By applying a magnetic field of just a few Gauss, depending on the anode voltage, the radial plasma loss can be significantly reduced, as a larger fraction of the generated plasma is directed towards the extractor and subsequently converted into an ion beam. An illustration of such a configuration, proposed at LBNL, Berkeley USA [35], is shown in Figure 2.5.

The initial shape of the ion beam, specifically the radial profile immediately after extraction, is primarily determined by the radial plasma density distribution at the extraction point along with

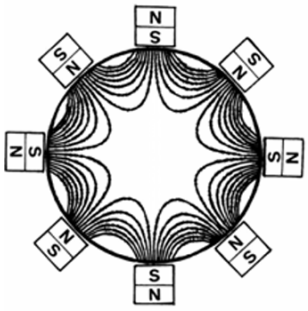

Figure 2.4: Illustration of plasma and ion beam confinement inside the extraction chamber of the ion source, which can be achieved with a small magnetic field [35].

the extraction optics. If the plasma density is not uniform across the extractor, achieving an optimal match with the extraction optics becomes challenging. Although using an open-ended multipole magnetic bucket, configured in the ion source drift region, can flatten the plasma profile at the extractor [41], the beam profile tends to quickly revert to a Gaussian shape after propagating some tens of centimeters downstream [42].

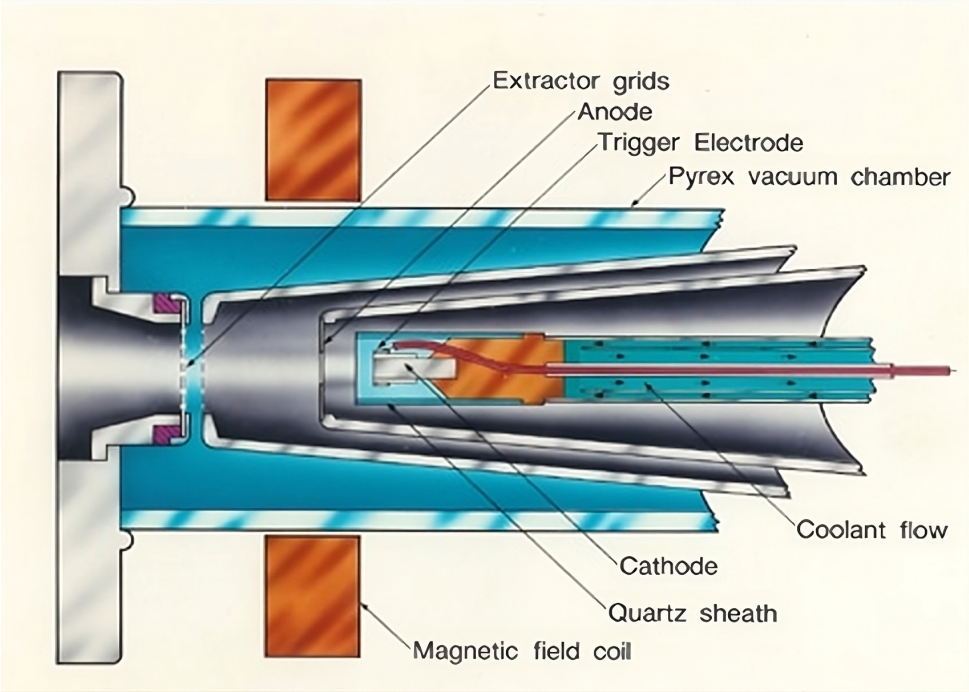

Figure 2.5: Schematic of a vacuum arc ion source, specifically the MEVVA II model, developed at Lawrence Berkeley National Laboratory (LBNL), Berkeley, USA [35]. The diagram shows the key components: electrodes (anode and cathode) for ion beam production, a gas inlet system, and a trigger mechanism for plasma arc ignition. The setup includes coils that generate a magnetic field to minimize radial plasma loss, optimizing the ion extraction process. The setup is kept at low temperatures through a coolant flow, usually refrigerated water.

2.1.1 Einzel Lenses

By adjusting the arc current one can further optimize the extraction by controlling the plasma density. Alternatively, to further refine and focus the beam, Einzel lenses, also known as unipotential lenses, are commonly used. These lenses can focus and direct the ion beam after the extraction, ensuring the beam maintains its desired shape and intensity over longer distances.

This is of central importance in the present work, where BaF molecules have to be implanted inside a crystal at a large distance (> 30 cm) from the source.
Einzel lenses are electrostatic lenses able to focus ion or electron beams without significantly altering their kinetic energy and are particularly valued for their simplicity and compactness. Moreover, since the focal power of electrostatic lenses is solely dependent on the energy of the charged particles and not on their charge-to-mass ratio, they are particularly advantageous over magnetic lenses for focusing heavily charged particles with moderate energy [43].
An Einzel lens typically consists of three cylindrical electrodes aligned along the axis of the beam path [44]. The central electrode is held at a high potential (positive or negative) while the outer electrodes are grounded. The primary purpose of this configuration is to create an electrostatic field that focuses the charged particles in the beam, as shown in Figure 2.6. The focusing princi-

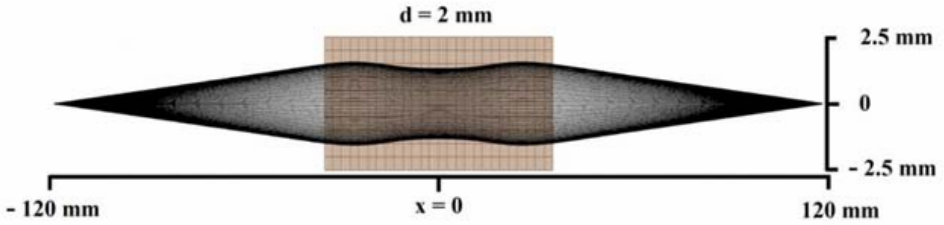

Figure 2.6: Beam path axial trajectory, simulated in the work of Abdulla et al. [45].

ple relies on the electric field applied in the region of the lens, as it affects the transverse velocity of the charged particles, focusing them without significantly changing their axial (longitudinal) velocity. A charged particle that enters the lens experiences a deceleration, while approaching the central electrode, and then an acceleration as it leaves the electrode. The overall net effect on the kinetic energy of the particle is minimal, but the transverse components of its motion are altered, leading to a focusing effect.
The potential V within the lens can be described by the Laplace equation for the cylindrical coordinates, given the boundary conditions of the grounded and high potential electrodes. The resulting electrostatic field E influences the motion of the charged particles, according to the Lorentz force $F = qE$, where q is the charge of the particle. The potential applied to the central electrode creates a symmetric electrostatic field causing the deceleration and subsequent re-acceleration of the particles. The axial potential $V(z)$ can be expressed as a function of the position z along the lens axis and can be approximated by solving Poisson's equation as:

$$V(z) = V_0 \left(1 - \frac{z^2}{d^2}\right) \tag{2.5}$$

where V_0 is the maximum potential at the center, and d is the distance from the center to the point where the potential is zero.
The lens action can be described by a focal length f that depends on the geometry of the electrodes and the potential applied to the central electrode.

$$f \approx \frac{2d}{\left(\frac{V_0}{V} - 1\right)} \tag{2.6}$$

where d is the distance between the electrodes, V_0 is the potential of the central electrode, V is the energy of the incoming beam particles. An illustration of an example of Einzel lens geometry along with the behaviour of the focal length is shown in Figure 2.7.

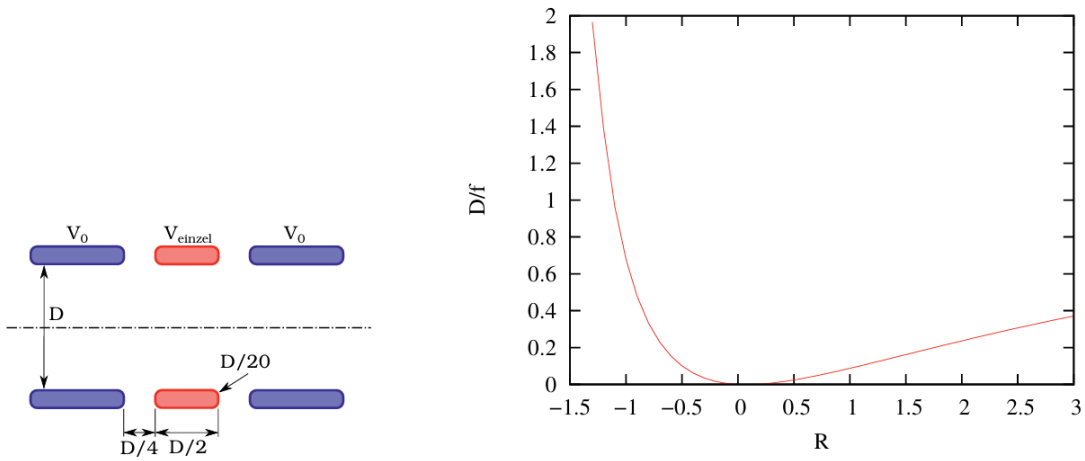

Figure 2.7: Left: An example of an Einzel lens geometry, here $D = 4d$; Right: The focal length scaled with D as a function of the ratio $R = \frac{V_0}{V} - 1$. Schematics taken from [46].

For a three-element Einzel lens, the potential distribution can also be controlled to ensure that the beam remains focused while minimizing spherical and chromatic aberrations [47]. Spherical aberration is a type of aberration where particles passing through the outer regions of the lens are focused at different points compared to those passing through the central regions, leading to a blurred beam. Spherical aberration in Einzel lenses can be quantified by calculating the deviation from the ideal focal point for particles entering the lens at different radial distances. Using a three-element lens with appropriately chosen electrode lengths and spacings can significantly reduce the spherical aberration compared to simpler designs. The work of A. Ahmad et. al. [47] proposes such a configuration of three electrodes, as shown in Figure 2.8.

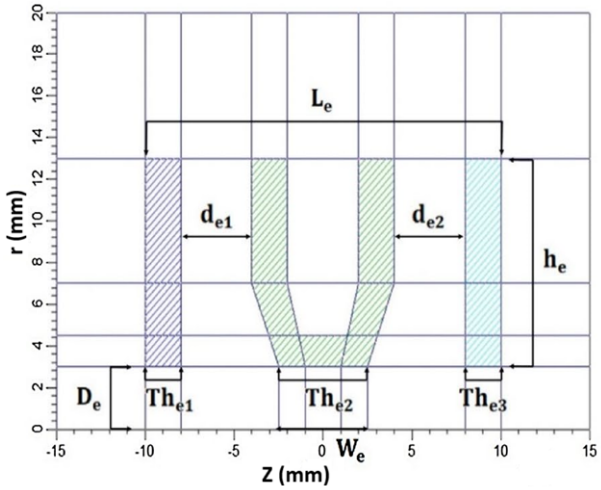

Figure 2.8: Configuration of a three electrodes Einzel lens to achieve minimal aberration. Illustration taken from [47].

2.1.2 BaF ion beam

As vacuum arc ion sources are primarily metal ion sources, they can also be operated to form beams that are controllable mixtures of gas and metal ions. This versatility makes them suitable for generating BaF ion beams, the molecule of interest in the present work apparatus for eEDM measurements. The process will begin by heating BaF_2 in an oven to vaporize the molecules

mainly into BaF + F. These vaporized BaF molecules are then ionized using the plasma generated with Helium in the vacuum chamber. This glowing plasma discharge provides the necessary conditions for ionizing BaF molecules, producing BaF^+ ions. The source used in this thesis is similar to the one introduced by Menzinger et al. [48], and is schematized in Figure 2.9. Further details will be given in Chapter 3. The proportion of gaseous ions can be regulated by

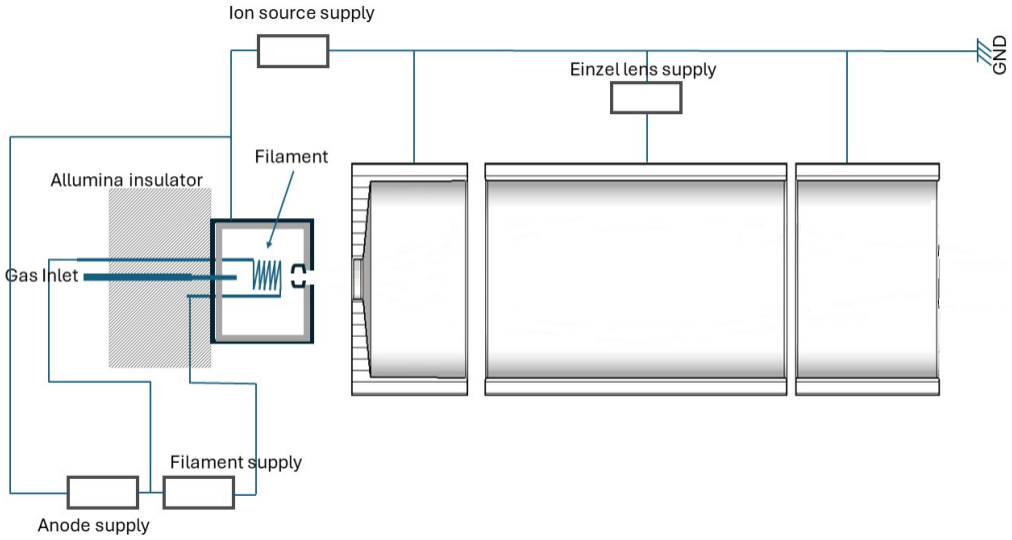

Figure 2.9: Schematic diagram of an ion beam source with plasma discharge suitable for BaF^+ beam production. Schematic of an ion beam source utilizing plasma discharge, designed for the production of a BaF^+ beam. The setup includes components such as the gas inlet, alumina insulator, filaments, and Einzel lens along with their driving circuit.

adjusting the neutral gas feed, allowing further control of the gas-to-metal ion ratio from zero up to about 99% gaseous ions for vacuum arc sources [35]. For the housing of the ion source ceramic materials have been choose for their resistance to the very high operational temperatures (1000 K) [50], but also for degassing processes, as shown in Figure 2.10 in comparison with another common material such as boron nitride [49]. This latter aspect allows to minimize impurities in the ion beam and red to reduce the vacuum pumping time. Experimental comparisons [49] have demonstrated that ceramic ion sources reach equilibrium conditions faster than their BN counterparts. The time to achieve equilibrium is reduced from about 140 minutes for a BN source to less than 50 minutes for a ceramic source under similar conditions.
Furthermore, once the ion source parameters are set, the system vacuum can be restored much more quickly with a ceramic source. This rapid restoration reduces downtime and increases the operational efficiency of the ion implantation equipment. These attributes make ceramic materials an optimal choice for constructing ion sources used in ion implantation and other demanding applications. In summary, the capability of vacuum arc ion sources to control the ion charge state distribution and the gas-to-metal ion ratio makes it a good choice for generating BaF ion beams.
This technique allows to have a high density of desired molecules inside the beam for a long period of time, as it will be shown in Chapter 3, which is crucial to prepare highly doped crystals for eEDM measurements using the matrix isolation technique.
The drawback of this technique is that it generates fast ions. For example, with an anode voltage of $U = 100$ V, the velocity of a BaF_{157} molecule exiting from a glow discharge source could be as high as:

$$v = \sqrt{\frac{2U}{m}} = \sqrt{\frac{2 \cdot 100 \cdot 1.60 \cdot 10^{-19}\text{J}}{157 \cdot 1.66 \cdot 10^{-27}\text{Kg}}} = 11.086 \text{ km/s} \tag{2.7}$$

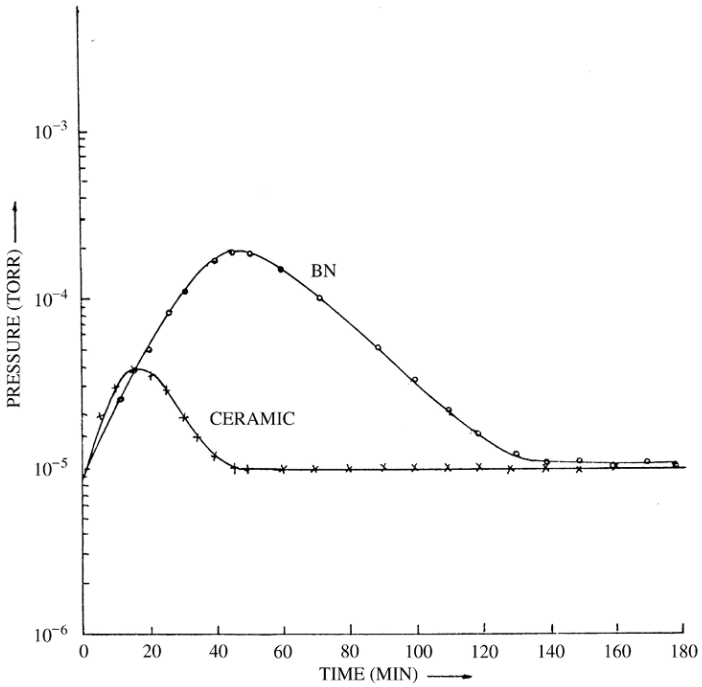

Figure 2.10: Characteristics of the degassing with ceramic and boron nitride (BN) ion-source. Figure from [49].

Furthermore, high temperatures of the ion beam, due to the plasma, will influence the already complicated molecular quantum states. In particular, a significant number of rotational or vibrational states can be excited due to the high temperature, while for the present purposes we are interested to a specific quantum state. Deceleration techniques are therefore needed when precision measurements are conducted with molecules in a gas state with such velocities. In the present work the matrix isolation technique has been chosen to overcome this issues, as it offers a promising method for interrogating BaF molecules by freezing them at around 4 K in an inert matrix, as previously mentioned in Chapter 1.4. However, deceleration technique will be employed in future experiments as high energy molecules might destroy the crystalline structure of the host crystal.

2.2 Laser ablation

In the field of molecular spectroscopy, the laser ablation technique is combined with different processes and methods to obtain stable and intense beams. In this section, a brief overview of some examples will be given, mainly effusive oven sources, supersonic expansions, and buffer gas cooling. As we will see, the combination of laser ablation with buffer gas cooling has become one of the standard method to produce molecular beams for eEDM measurements for its capability to produce a good quantity of molecules at low kinetic energy.
Laser ablation is a technique used to generate molecular beams, employing a high energy pulsed laser to ablate material from a solid target surface, creating a plasma of vaporized atoms or molecules. In particular, we will focus on laser with nanosecond (ns) pulses, as they are the most commonly used in eEDM research.
With ns pulses, the interaction of the laser with the material involves a sequence of physical phenomena, mainly: energy absorption, thermal diffusion, and material ejection. When the laser pulse strikes the surface of a material, the energy is predominantly absorbed by free electrons within the material through photon-electron interactions, which is then rapidly transferred to

the lattice atoms via electron-phonon coupling.
For laser irradiance below 10^8 W/cm^2, thermal processes dominate the interaction [51]. Thus, the efficiency of the energy transfer will be dependent on the material thermal properties, as the target surface temperature will increase leading to melting and vaporization of it.
The temperature distribution within the target [52] can be described by the heat conduction equation:

$$\frac{\partial T(x,t)}{\partial t} = \frac{\partial}{\partial x}\left(\kappa \frac{\partial T(x,t)}{\partial x}\right) + \frac{\alpha}{C_p \rho_s} I(x,t) \tag{2.8}$$

where T is the temperature inside the target, x is the distance from the surface, and κ, C_p, ρ_s, and α represent the thermal conductivity, heat capacity, mass density, and absorption coefficient of the solid target material, respectively.
The thermal diffusion length L_{th} during the nanosecond pulse is a parameter that determines the extent of the heat-affected zone (HAZ). The diffusion length [53] can be calculated using:

$$L_{\text{th}} = \sqrt{\alpha \tau} \tag{2.9}$$

where α is the thermal diffusivity of the material and τ is the pulse duration.
For nanosecond pulses, this length is typically in the micrometer range, leading to significant heating of the material to start the ablation process. However, the broad HAZ associated with nanosecond ablation can result in undesirable effects, such as a significant material damage compared to shorter pulse duration. Nonetheless, a longer pulse allows for more material to be removed, thus more molecules of interest are being diffused compared to shorter pulses.
Plasma formation is an inevitable consequence of the high energy laser-matter interaction. As the material is ablated, a plasma plume consisting of ionized atoms and electrons forms above the surface. The plasma absorbs and scatters the incident laser radiation, creating a shielding effect that reduces the effective laser fluence reaching the surface.
The intensity reduction due to this effect [54] can be described by:

$$I_{\text{eff}} = I_0 e^{-\alpha z} \tag{2.10}$$

where I_{eff} is the effective intensity reaching the material surface, I_0 is the initial laser intensity, α is the absorption coefficient of the plasma, and z is the distance from the surface. The plasma expansion also generates a recoil pressure that can influence the material removal process, complicating the ablation dynamics. Once the laser pulse ends, particles leave the sample surface

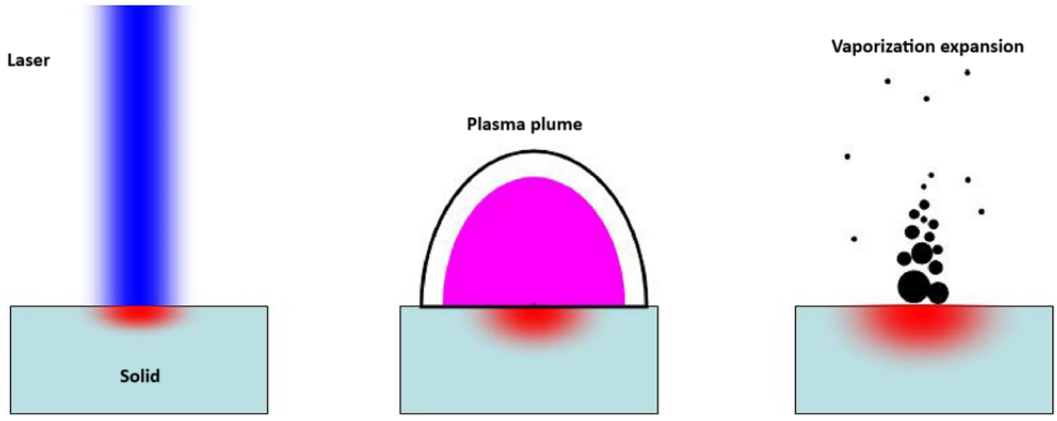

Figure 2.11: Schematic of the three main laser ablation processes. From left to right: Laser energy absorption of the sample; thermal diffusion and plasma plume generation; particles diffusion [51].

due to the expansion of the plasma plume. A schematic of the laser ablation process is shown in Figure 2.11.

In a vacuum, the laser-induced plasma plume expands adiabatically [55], whit velocity expressed as:

$$v_p = \sqrt{\frac{4\gamma + 10}{3}\frac{E}{M_v}} \tag{2.11}$$

where v_p is the expansion velocity, γ is the specific heat ratio, E is the energy driving the expansion, and M_v is the total mass of the vaporized sample within the plume.
Due to the plasma plume effect, the vapor of the interested molecules is created at temperatures over 8000 K [51], leading to molecules velocities too high to allow precise spectroscopy measurements. Therefore, a description of the gas flow and gas cooling techniques is then needed to guarantee a fine characterization and analysis of the species of interest.

Gas flow and cooling

Laser ablation to form a beam occurs inside of a cell with a hole where the gas exits. To define and characterize the gas flow through such small apertures the Reynolds number is typically used. Defined as the ratio of inertial and viscous forces in a fluid flow [56], it is described as:

$$\mathrm{Re} = \frac{F_{\text{inertial}}}{F_{\text{viscous}}} = \frac{\rho w d}{\mu} \tag{2.12}$$

where ρ represent the density, w is the flow velocity, μ is the dynamic viscosity, and d is the aperture diameter. The Reynolds number can be related to kinetic quantities by the Von Karman relation [57]:

$$\mathrm{Re} \approx \frac{1}{2}\frac{\mathrm{Ma}}{\mathrm{Kn}} \tag{2.13}$$

where the Knudsen number, $\mathrm{Kn} = \lambda/d$ is a relation describing the collisions within a system, represented as the ratio of the mean free path λ to a characteristic length scale d, such as the aperture diameter of a hole to generate a gas beam. The mean free path λ is given by:

$$\lambda = \frac{1}{\sqrt{2} n \sigma} \tag{2.14}$$

with n being the number density of the gas and σ the elastic collision cross-section of the gas atoms.
The Mach number is defined as $\mathrm{Ma} = w/c_{\text{gas}}$, where w is the flow speed, and $c_{\text{gas}} = \sqrt{\frac{\gamma kT}{m}}$ is the speed of sound in a gas with specific heat ratio γ and atomic mass m.
Near the aperture, the gas atoms travel close to their mean thermal velocity:

$$v = \sqrt{\frac{kT}{\pi m}} \tag{2.15}$$

One can observe that the buffer gas density within the cell, the buffer gas flow rate, the Reynolds number, and the number of collisions near the aperture are all linearly related. For instance, if one considers the Mach number $Ma \approx 1$:

$$\mathrm{Re} \approx 2\mathrm{Kn}^{-1} = \frac{2d}{\lambda} \tag{2.16}$$

indicating that the number of collisions occurring at distance equivalent to the aperture diameter, from the aperture itself, is approximately doubled when compared to the number of collisions expected in the absence of the effects of compressibility and rarefaction at high speeds.

Through the Reynolds number, three main flow types regime can be categorized:

- **Effusive regime, Re $\lesssim$ 1**: This is the regime where effusive beams operate. Typically there are no collisions near the aperture, thus the beam properties remain consistent with those observed while inside the cell.
- **Intermediate or partially hydrodynamic regime, 1 $\lesssim$ Re $\lesssim$ 100**: Buffer gas beams usually operate in this regime. Collisions near the aperture are enough to alter the beam properties from those in the cell.
- **Fully hydrodynamic or supersonic regime, Re $\gtrsim$ 100**: This is the regime of supersonic beams. Here the buffer gas starts to behave more like a fluid due to the high number of collisions. The beam properties become similar to those of a beam cooled via supersonic expansion.

A common setup involves a gas cell with a thin exit aperture, where both the thickness of the aperture and its diameter (d) are significantly smaller than the mean free path (λ) of the gas. It is important to note that the effusive beams discussed here originate from oven-type effusive sources, where the vapor pressure of the species is high at the source temperature. Buffer gas-cooled effusive sources operate instead at temperatures where the species have negligible vapor pressure.

Effusive oven sources

Effusive oven sources, characterized by their operational simplicity, involve heating a sample in an oven until its vapor pressure becomes sufficient for the molecules to escape through the small orifice in the oven, thus forming a beam. The Knudsen cosine law [58], tested by F. Celestini and F. Mortessagne et al. [59], describes the effusion rate of molecules through a hole as:

$$dQ_0 = \frac{1}{4\pi} n \bar{v} A_o cos(\theta) d\omega \tag{2.17}$$

where Q_0 is the total molar flux, n is the density in the source, $\bar{v}$ is the average molecular velocity, A_o is orifice area and ω is the emission solid angle. This method excels in producing steady-state beams and is suitable for species with relatively low evaporation temperatures. However, effusive oven sources often produce beams with widely distributed translational velocities, typically ranging from 200 to 800 m/s, and result in high translational and rotational temperatures, in the range of 500 to 2000 K [60]. Additionally, the steady-state nature of effusive oven sources contributes to a relatively low number of particles per pulse.

Supersonic expansion

In supersonic expansion the problem of the high temperature is mitigated by mixing the target species, produced with laser ablation, with an inert carrier gas at high pressure, such as Helium or Argon, and expanding the mixture through a small nozzle into a vacuum chamber. This adiabatic expansion process leads to collisional cooling of the molecules, where their thermal motion is converted into kinetic energy. Near the exit aperture the gas undergoes under many collisions (typically Kn $< 10^{-3}$), accordingly, supersonic expansions successfully generates molecular beams with lower translational and rotational temperatures, in the range of $1 - 5$ K [61], compared to effusive oven sources. The resulting decrease in translational velocity spread translates to a narrowing of the beam's velocity distribution, achieving typical velocities of 500 to 2000 m/s, thereby improving spectral resolution in experiments by reducing Doppler broadening. However, the high intrinsic beam velocity of supersonic expansions poses challenges by reducing the available interrogation time for spectroscopic experiments.

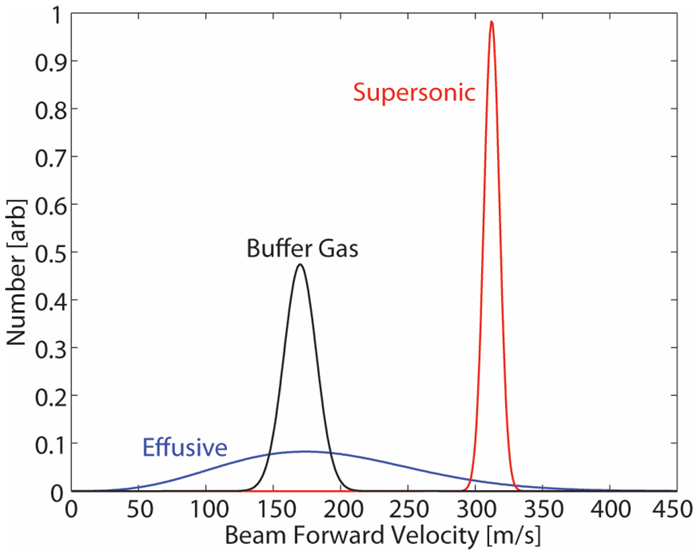

Figure 2.12: Schematic velocity distributions illustrate the properties of effusive, supersonic, and buffer gas-cooled molecular beam sources. [62]

2.2.1 Buffer gas cooling

Buffer gas cooling, first described by J. K. Messer and F. C. De Lucia et al. [63], is currently the main technique associated to laser ablation for gas cooling. It involves the introduction of a hot species of interest, usually with a concentration lower than 1%, into a cold cell filled with an inert buffer gas, such as helium or neon, which is maintained at cryogenic temperatures, ranging from 2 to 20 K [60]. This technique operates between $1 \leq Kn \geq 100$, therefore between effusive and supersonic regimes, and is composes of three stages to form a molecular beam: cooling, diffusion and extraction.
In the first stage, the cold buffer gas cools the hot molecules through elastic collisions, ideally bringing them to the temperature of the buffer gas. Few conditions bust be taken into account, for instance the thermalization distance of the molecule of interest must not exceed the length of the cell. Moreover, the cooling process is also dependent on the flow of the cool gas in the cell.

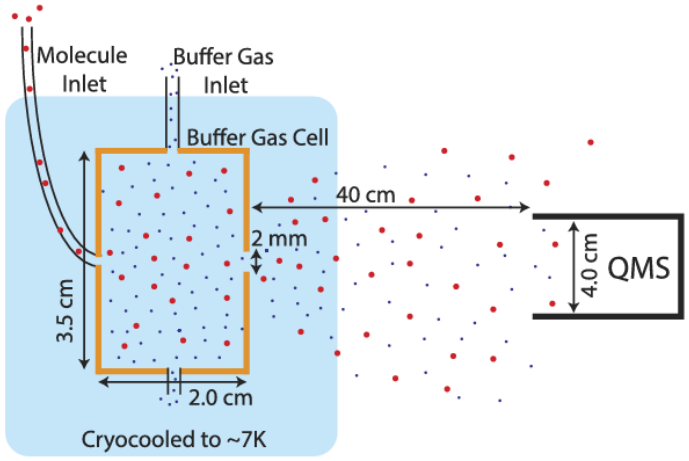

Figure 2.13: Schematic of an ablation cell employing buffer gas cooling, as utilized by [64]. Molecules are introduced into the cell and cooled to approximately 7K through collisions with a buffer gas. The cooled molecules exit the 2 mm aperture and travel through a 40 cm region before being analyzed by a Quadrupole Mass Spectrometer (QMS).

A simple model can be used to understand these aspects, in which both the molecules and the gas atoms are assumed to behave as hard spheres [65, 66]. We consider the mean temperature change per collision, which can be expressed as:

$$\Delta T_s = -(T_s - T_b) \cdot \frac{2m_s m_b}{(m_b + m_s)^2} \tag{2.18}$$

here the subscript b and s denotes buffer gas and species of interest, respectively, while T is the temperature and m the mass.
The temperature of the species after $\mathcal{N}$ collisions, $T_s(\mathcal{N})$, is given by:

$$T_s(\mathcal{N}) = T_s(\mathcal{N}-1) - (T_s(\mathcal{N}-1) - T_b)/\kappa \tag{2.19}$$

where $k = \frac{(m_b+m_s)^2}{2m_s m_b}$.
If $\mathcal{N}$ is large and the temperature change per collision is small, this discrete equation can be reduced to a differential equation:

$$\frac{dT_s(\mathcal{N})}{d\mathcal{N}} = -(T_s - T_b)/\kappa \, . \tag{2.20}$$

Solving this differential equation yields the ratio between the species' temperature and the buffer gas temperature:

$$\frac{T_s(\mathcal{N})}{T_b} = 1 + \left(\frac{T_s(0)}{T_b} - 1\right) e^{-\mathcal{N}/\kappa} \, . \tag{2.21}$$

Assuming that the species is introduced at a temperature much higher than that of the cell, and therefore the buffer gas, i.e. $T_s(0) \gg T_b$:

$$T_s(n) \approx T_b \left(1 + \frac{T_s(0)}{T_b} e^{-\mathcal{N}/\kappa}\right) \, . \tag{2.22}$$

If $m_b \approx 10$ amu, $m_s \approx 100$ amu, $T_b \approx 10$ K, and $T_s(0) \approx 1000$ K, the species' temperature should be within a few percent of the buffer gas temperature after approximately 50 collisions. This last approximation doesn't hold true if the molecules of interest are introduced with laser ablation, as the high temperatures involved require a larger number of collision, resulting in a thermalizing time of a few milliseconds [67].
It is important to note that the previous discussion focused exclusively on translational temperatures. Nonetheless, one of the primary characteristics of buffer gas cooling is its effectiveness in thermalizing internal states as well. For example, the typical rotational relaxation cross sections for molecules in helium buffer gas are approximately $\sigma_{\text{rot}} \approx 10^{-15} - 10^{-16}$ cm^2. Consequently, it takes around $\sigma_{b-s}/\sigma_{\text{rot}} \approx 10 - 100$ collisions [68] to relax the energy of a rotational state. As stated above, this is comparable with the typical number of collisions needed to achieve translational thermalization, making buffer gas cooling one of the best cooling technique, since it is capable of producing molecular samples that are cold in both translational and rotational degrees of freedom.
Once the species of interest is introduced into the cell and thermalized, it is essential to consider the second stage of buffer gas cooling, diffusion. The buffer gas cell is typically maintained at a temperature where the species has negligible vapor pressure and if it diffuses to the cell walls before exiting it will freeze and be lost. Understanding diffusion is therefore critical.
The diffusion constant for the species in the buffer gas is given by [62]:

$$D = \frac{3}{16\,(n_{0,\text{b}} + n_{0,\text{s}})\,\sigma_{b-s}} \left(\frac{2\pi k_B T_0}{\mu}\right)^{1/2} , \tag{2.23}$$

where $\mu = \frac{m_s m_b}{m_s + m_b}$ is the reduced mass, n_0 is the gas density and σ_{b-s} is the thermally averaged elastic collision cross section. Assuming $n_{0,\text{s}} \ll n_0, \text{b}$ and $m_s \gg m_b$, we get:

$$D = \frac{3}{16 n_{0,\text{b}} \sigma_{b-s}} \left(\frac{2\pi k_B T_0}{\mu}\right)^{1/2} = \frac{3\pi}{32 n_{0,\text{b}} \sigma_{b-s}} \bar{v}_{0,\text{b}}, \tag{2.24}$$

where $\bar{v}_{0,\mathrm{b}}$ is the thermal velocity of the buffer gas. After a time t, the mean-squared displacement of a molecule is:

$$\langle \Delta x^2 \rangle(t) = 6Dt = \frac{9}{16 n_{0,\mathrm{b}} \sigma_{b-s}} \bar{v}_{0,\mathrm{b}} t. \tag{2.25}$$

Given the cell's cross-sectional length d_{cell}, the diffusion timescale τ_{diff} is defined through the relation $\langle \Delta x^2 \rangle(\tau_{\mathrm{diff}}) = d_{\mathrm{cell}}^2 \approx A_{\mathrm{cell}}$ as:

$$\tau_{\mathrm{diff}} = \frac{16 A_{\mathrm{cell}} n_{0,\mathrm{b}} \sigma_{b-s}}{9\pi \bar{v}_{0,\mathrm{b}}}, \tag{2.26}$$

which is typically $1 - 10$ ms [62].
An analysis of Skoff et al. [67] compared the theoretical diffusion with measured absorption images of YbF and Li in helium buffer gas. They observed that at low densities, such as $n_{0,\mathrm{b}} \lesssim 3 \times 10^{15}$ cm^{-3} at 20 K, the linear relationship between τ_{diff} and $n_{0,\mathrm{b}}$ holds. At high densities, a divergence from linearity was noted, suggesting that molecules remain localized near the target and primarily occupy higher-order, faster diffusion modes.

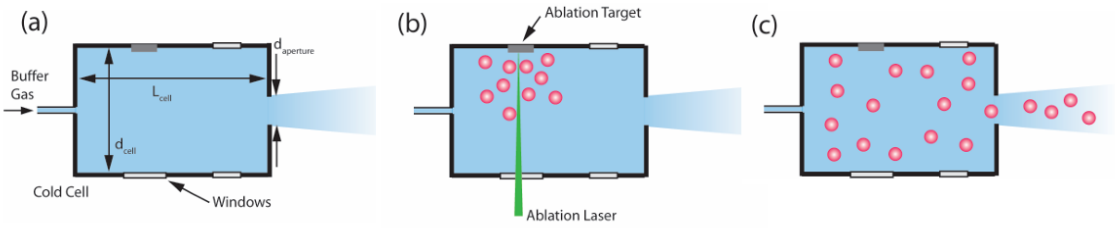

Figure 2.14: Overview of molecular beam production with buffer gas cooling and laser ablation. Image (a): The cold buffer gas enters the cell, which has a length (L_{cell}) and diameter (d_{cell}), and exits through an aperture with diameter (d_{aperture}). Image (b): Laser ablation of a precursor target produces the species of interest. Image (c): The species thermalize with the buffer gas. A molecular beam is then formed and exits the cell through the aperture, along with the buffer gas. Adapted from [62]

.

Once the species of interest is created in the gas phase and cooled in the buffer gas cell, it is crucial to ensure that the species exits from an aperture to form a beam, as shown in Figure 2.14, where a setup of laser ablation along with a buffer gas cooling cell is illustrated. As mentioned earlier, in the extraction stage the species of interest must be faster than the diffusion timescale, τ_{diff}. An important parameter here is the extraction or "pump-out" time. The rate at which the buffer gas exits the cell is given by the molecular conductance of the cell aperture:

$$\dot{N}_b = \frac{\bar{v}_{0,\mathrm{b}} A_{\mathrm{aperture}}}{4 V_{\mathrm{cell}}} N_b, \tag{2.27}$$

where N_b represents the total number of buffer gas atoms in the cell. This results in an exponential decay with a timescale τ_{pump}, the pump-out time, given by:

$$\tau_{\mathrm{pump}} = \frac{4 V_{\mathrm{cell}}}{\bar{v}_{0,\mathrm{b}} A_{\mathrm{aperture}}}. \tag{2.28}$$

Typically, τ_{pump} is a few milliseconds. This also sets the duration of the molecular pulse in the case of a pulsed beam. If the buffer gas density in the cell is high enough, the species of interest will follow the buffer gas flow, providing a good estimate for the pump-out time.
A dimensionless parameter γ_{cell} [69], is used to characterize the cell extraction process:

$$\gamma_{\mathrm{cell}} = \frac{\tau_{\mathrm{diff}}}{\tau_{\mathrm{pump}}} = \frac{4 n_{0,\mathrm{b}} \sigma_{b,s} A_{\mathrm{aperture}}}{9\pi L_{\mathrm{cell}}}. \tag{2.29}$$

where L_{cell} is the cell length.
The parameter γ_{cell} sets two different regimes:

- $\gamma_{\text{cell}} \lesssim 1$: most molecules get stuck to the cell walls and are lost, as diffusion is faster than extraction. This diffusion limit is characterized by low output flux and a velocity distribution similar to that inside the cell. Increasing γ_{cell} improves the extraction efficiency, f_{ext}, defined as the fraction of molecules created to the ones extracted.
- $\gamma_{\text{cell}} \gtrsim 1$: the molecules are extracted before sticking to the walls. This hydrodynamic entrainment limit is characterized by high output flux and a velocity distribution different from that inside the cell. The extraction efficiency can reach over 40%, but is typically around 10%.

It should be noted that while γ_{cell} effectively estimates extraction efficiency, there are exceptions. For instance, in the work of Hutzler et al.[70], varying the cell aperture diameter without changing other parameters affected the extraction efficiency of a ThO beam in a neon buffer gas. These findings suggest that the aperture Electric Dipole Moment should not be too small ($\lesssim 3$ mm) for optimal extraction, as shown in Figure 2.15. Regardless of the γ_{cell} value, thermalization must

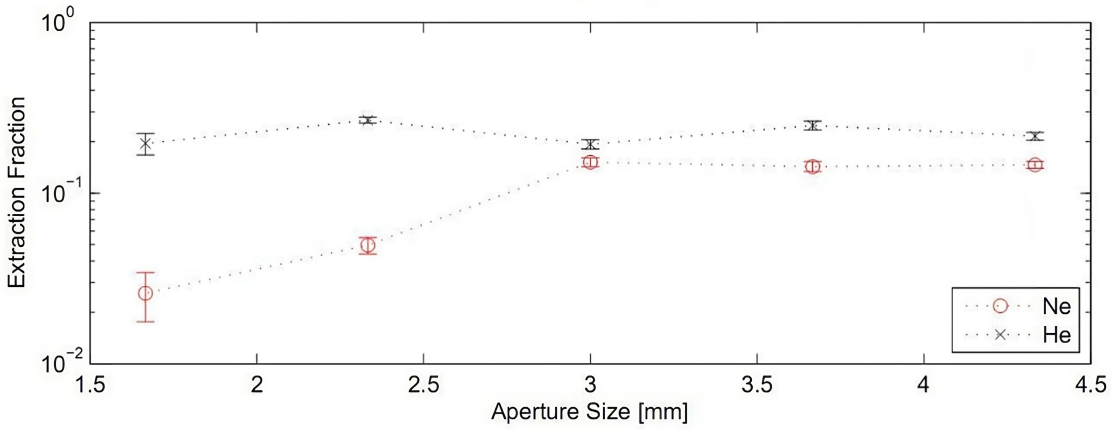

Figure 2.15: Results of an analysis [70] of extraction fraction vs aperture size for two different buffer gases (He and Ne). For helium buffer the extraction remains constant. For neon buffer gas, the extraction fall when the aperture size is lower than 3 mm.

occur faster than either τ_{pump} or τ_{diff} to cool the species. This ensures both good thermalization and efficient extraction, as demonstrated by many high flux cold beams created using the buffer gas method [71].
The Reynolds number governing the gas flow regime and the extraction parameter γ_{cell}, are related by:

$$\gamma_{\text{cell}} \propto \frac{\text{Re}}{d_{\text{cell}}}. \tag{2.30}$$

This indicates that it is possible to separately control the extraction efficiency (γ_{cell}) and the flow regime (Re). Most buffer gas sources operate in either the effusive or intermediate flow regimes, and it is challenging to design a beam that is entirely effusive, has good extraction, and sufficient thermalization.
The final forward velocity of a molecular beam coming out of a buffer gas cell [72] is:

$$v*_{||} = \sqrt{\frac{5}{2}\frac{2K_B T_0}{m}} \approx 1.6\bar{v}_{0,b} \tag{2.31}$$

where m is the buffer gas particle mass and T_0 is the stagnation temperature of the source.
Typical values range between 120 and 250 m/s [70]. For instance, with neon buffer gas at 18 K

and a ThO beam, simulations predict a final velocity of approximately 200 m/s.

2.3 Molecules spectroscopy

Working with molecules is more complicated compared to atoms, due to the presence of roto-vibrational degrees of freedom [73]. The population distribution across rotationally and vibrationally excited states reduces the density in any quantum state, decreasing the experimental sensitivity for any investigated transition. Furthermore, high rotational and vibrational temperatures, along with elevated translational temperatures of the molecule, can lead to Doppler broadening of the spectral linewidths. To mitigate these effects it is crucial to reduce both the internal temperatures (rotational and vibrational) and the translational temperatures of the molecules. Both sources described in the previous section have been developed for these purposes. However further techniques are required to allow high precision spectroscopy investigations.
Static trapping would be ideal for molecule spectroscopy, but it is impractical at the final velocities of buffer gas cooling or plasma ion sources. To investigate a molecule of interest, the main objective is thus to prepare samples of even more cold molecules. This will allow to confine them in trapping potentials that allow for extended interrogation times, like a magneto-optical trapping (MOT) used in the current eEDM record [16]. Several methods have been developed to achieve this level of molecule control. In this section we are gonna analyse laser cooling techniques.

2.3.1 Laser cooling

Historically, it was believed that laser cooling of molecules was unfeasible. Electric dipole transitions between rotational states follow selection rules for total angular momentum, $J = 0, \pm 1$, and total parity, $+ \leftrightarrow -$. Rotational closure can be achieved by driving $N = 1 \leftrightarrow 0$ transitions and using magnetic fields to destabilize the dark states within the $N = 1$ hyperfine levels. However, vibrational transitions are restricted by different selection rules, known as Franck-Condon factors (FCFs, the overlap integrals for pairs of vibrational wave functions). This initially suggested that any effort to scatter photons off a molecule would rapidly populate states that are off-resonant with the cooling light, creating a bottleneck that limits the photon cycling rate.
It has been found that a significant subset of molecules possess diagonal FCFs, where the electronic and vibrational degrees of freedom are strongly decoupled, such that vibrational relaxation pathways can be closed [74, 75]. This decoupling is characteristic of bonds between a metal atom, such as Ca, Yb, or Ba, and a strongly electronegative ligand, like F, Cl, or OR (where R represents any functional group). In these molecules, the electron cloud is concentrated around the metal atom, meaning that an electronic excitation only slightly alters the bond length. Consequently, photon scattering remains localized at the metal atom, which acts as an optical cycling center.
Currently, many experiments involving magneto-optical traps (MOTs) use laser cooling. For example, Truppe et al. [76] demonstrated that a molecular beam of CaF was cooled down to 50 μK through a molecular MOT, following a laser cooling cycle. Another versatile method to achieve longitudinal slowing is the use of Stark and Zeeman decelerators, which can reduce or even eliminate the need for optical cycling. An example is a 4.5 m long traveling-wave Stark decelerator, shown in Figure 2.16, where SrF molecules are stopped in the laboratory frame as the beam passes through a series of ring-shaped electrodes, achieving a density similar to early MOTs of the same species [77]. In this experiment, the velocity of SrF molecules in the $X^2\Sigma^+(v = 0, N = 1)$ low-field seeking state is manipulated within the time-dependent inhomogeneous electric field distribution created inside the Stark decelerator, where packets of molecules are confined by a traveling potential well, successfully removing more than 85% of the molecules'

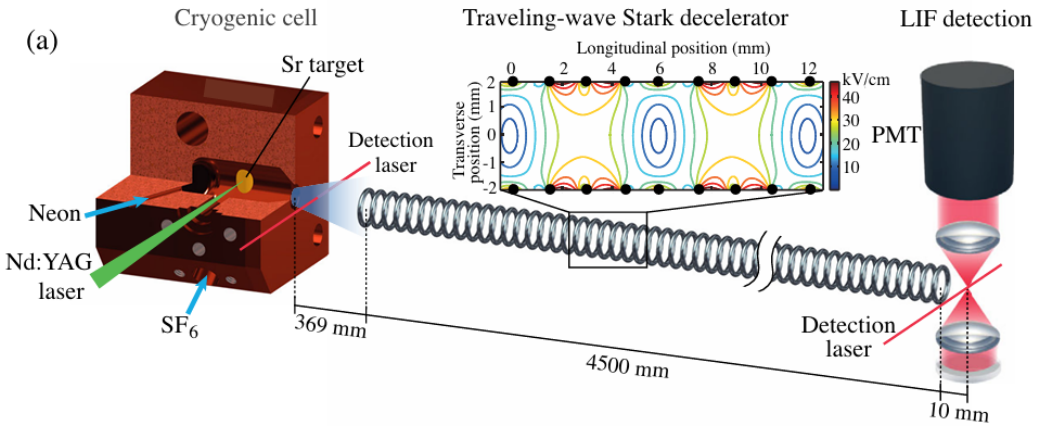

Figure 2.16: Schematic setup of a 4.5 m long traveling-wave Stark decelerator. The molecular beam exits from the buffer gas cooled source at velocities around 200 m/s and can potentially be cooled down to 4 m/s. Adapted from [77].

initial kinetic energy [78].
Both techniques encounter challenges with molecule loss during deceleration. In laser cooling, molecules like YbF can decay via low-lying electronic states, such as those arising from the excitation of a 4f electron, that can act as intermediate levels where molecules may decay, resulting in the loss of molecules from the cooling cycle [79]. Stark deceleration leads to molecule loss as well, with an estimated efficiency of 0.25%, corresponding to about 1000 molecules per shot detected after deceleration, according to the work of Mathavan et al. [78].

2.3.2 Matrix isolation

Matrix isolation mitigates molecule losses by embedding molecules in an inert, cryogenically cooled solid matrix, typically composed of noble gases like argon or neon. In this environment, the matrix restricts the movement of the molecules, as shown in the illustration of Figure 2.17, preventing them from escaping.

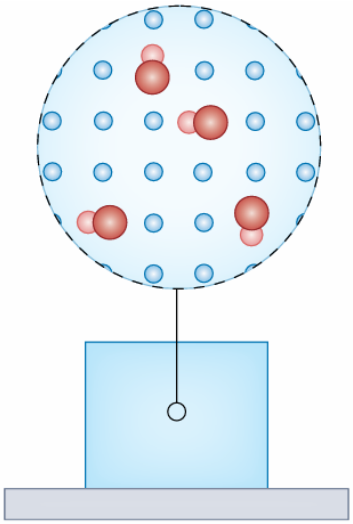

Figure 2.17: Illustration of a cryogenic crystal doped with the molecules of interest. Adapted from [10].

Consequently, while gas-phase molecules may provide the highest possible coherence time, solid-state molecules offer large number of the investigated molecule, a crucial parameter for eEDM sensitivity. Moreover, at the crystal's temperature, around a few K, the guest particles are cooled

to their ground electronic and vibrational states, facilitating spectroscopy measurements. This led to a renewed interest in eEDM searches using polar molecules embedded in crystals or noble gas matrices [80, 81]. These optically transparent media facilitate quantum control and readout methods and demonstrate potentially high sensitivity, provided that systematic errors from the complex solid-state environment can be managed.

Exploited for the first time by Whittle et al. [82] in 1954, matrix isolation, or matrix trapping, allows for the stabilization of the species of interest, known as the guest, by embedding it in a small proportion within an inert solid, referred to as the host, usually a noble gas, at a low temperature. This setup significantly reduces intermolecular reactions, achieving minimal or no interference from the surrounding environment.

The process begins with the deposition of the matrix material at temperatures typically below 20 K, onto a cold substrate, to form the host matrix. This can be achieved through techniques such as co-condensation, where the matrix material and the guest species are simultaneously deposited from the gas phase. As the matrix material condenses, the guest species are trapped within the interstitial spaces of the solid matrix. Once the matrix has been doped with the guest species, various spectroscopic techniques can be employed to study their properties. Infrared (IR), ultraviolet-visible (UV-Vis), and electron spin resonance (ESR) spectroscopy are commonly used methods. The matrix environment allows for high resolution spectra, which can provide detailed information about the electronic, vibrational, and rotational states of the trapped species.

The matrix material, either a noble gas like argon, N_2 [83], or solid parahydrogen, is inert and interacts weakly with the trapped species. This ensures that the guest species retain many of their gas-phase properties, facilitating their study in a controlled setting. Therefore, the choice of a proper matrix host material is crucial to conduct precision measurements with the molecule of interest. In table 2.1 the most important properties of host matrices such as H_2, Ne, Ar, Kr, Xe, and N_2, are given.

Table 2.1: Electronic and crystal-related properties of p-H_2 and conventional matrix hosts (Ne, Ar, Kr, Xe, and N_2) [84, 85].

	Quadrupole moment (Q)[a]	**Dielectric constant (ϵ')**[a]	**Crystal structure**[b]	**Lattice constant Å**	**N.n. distance Å**	**Zero-point motion**[c]
***p*-H_2**	0 (0.4)[d]	1.28 (3 K)	hcp	3.79 (4.2 K)	3.793	18%
Ne	0	1.25[f]	ccp	4.47 (15 K)	3.16 (4 K)	9%
Ar	0	1.63 (20 K)	ccp	5.31 (15 K)	3.76 (4 K)	5%
Kr	0	1.88 (20 K)	ccp	5.65 (15 K)	3.99 (4 K)	3%
Xe	0	2.19 (20 K)	ccp	6.13 (15 K)	4.34 (4 K)	2%
N_2	-1.4	1.43 (4.2 K)[g]	ccp	5.66 (15 K)	3.99 (4 K)	–

[a] Q in unit of 10^{26} esu cm^2; ϵ' in unit of F m^{-1}.

[b] hcp: hexagonal close-packed;
ccp: cubic close-packed, same structure as fcc (face-centered cubic).

[c] Root-mean-square longitudinal zero-point amplitude divided by the lattice constant, $\langle u^2 \rangle^{1/2}/R_0$; from [85].

[d] The quadrupole moment of o-H_2 is listed within parentheses.

In the present work we are interested to matrix hosts that do not influence the eEDM of the host molecule. Anisotropic interactions arise in hosts with an electric dipole moment, thus symmetrical structures are preferred, even though symmetric molecules can possess higher-order moments like quadrupole or hexadecapole moments. parahydrogen (p-H_2), one of the two isomers of hy-

drogen, whose properties are further discussed in the next section, is an exceptional host. Unlike the second isomer, orthohydrogen (o-H_2), parahydrogen has no quadrupole moment. The importance of quadrupole moments in intermolecular interactions was highlighted in the study of Tsuge et al. [86] on solid noble gases and N_2, where differences in decay periods of acid isomers are attributed to dipole-quadrupole interactions.
Moreover, the dielectric constant of the matrix host affects the wavenumbers of IR lines of guest molecules. Solvent-induced shifts tend to be smaller in hosts with lower relative permittivity (i.e. dielectric constant). For instance, these shifts are typically less than 1% from the gaseous phase ones when in a matrix trap of Ne [87]. Since p-H_2, has a similar dielectric constant, one can assume that it would also be an an excellent host for preserving the intrinsic properties of guest molecules.
The crystal structure influences the spatial arrangement and interaction of guest molecules within the matrix. Noble-gas atoms crystallize in either cubic close-packed (ccp) or hexagonal close-packed (hcp) structures. For example, solid argon shows a mixture of meta stable hcp and stable ccp structures, which results in broadening of the spectra. In contrast, solid p-H_2 is predominantly hcp, a more stable structure, though it can have mixed structures upon direct deposition. Annealing solid p-H_2 at approximately 4.5 K converts it to a more stable hcp structure, that could be otherwise led towards a ccp structure by the presence of o-H_2 or guest molecules.
The zero-point motion relative to the distance to the nearest neighbour affects the dynamic properties of the matrix and the behavior of guest molecules, as it indicates the localization of particles at their equilibrium positions within the crystal lattice. Solid p-H_2 exhibits significant zero-point motion, amounting to 18% of the lattice constant, indicating its classification as a quantum solid. This large zero-point motion distinguishes solid p-H_2 from classical solids like Ar, where zero-point motion is much smaller, as it indicates that the guest molecules are less influenced by the crystalline structure of the host.
These parameters collectively influence the behavior and interactions of guest molecules within the host matrix and the exceptional properties of parahydrogen makes it a very good host for eEDM measurement.

2.3.3 Parahydrogen cryogenic crystals

Parahydrogen is the singlet state of molecular hydrogen, characterized by anti parallel nuclear spins resulting in a total nuclear spin of zero. When hydrogen is cooled to low temperatures, it can exist in two distinct spin isomers: orthohydrogen and parahydrogen. In orthohydrogen, the nuclear spins are parallel, leading to a triplet state with a total nuclear spin of one. Conversely, parahydrogen, with its anti parallel spins, resides in a lower energy state compared to orthohydrogen.
In practical applications, p-H_2 is typically enriched to over 99% [88] by cooling hydrogen gas over a catalyst at cryogenic temperatures. Due to its spherically symmetric ground state ($J = 0$), p-H_2 provides a nearly perturbation-free environment for guest molecules. This could lead to sharp spectral lines for the guest molecules when embedded in this host.
Moreover, the zero-point motion (ZPM), affected by the quantum mechanical vibrations of particles, is significant for parahydrogen. Its atoms are very light and weakly interacting, leading to a large root mean square width of 18% of the nearest neighbor distance in the lattice, which is quite large compared to classical solids. Furthermore, the large ZPM of p-H_2 leads to anharmonicities in the lattice dynamics.
This characteristic makes p-H_2 a quantum solid, and the quantum Hamiltonian for the ground state of a solid [85] can be expressed as:

$$\hat{H} = -\frac{1}{2}\lambda^2 \sum_i \nabla_i^2 + \frac{1}{2}\sum_{i \neq j} \nu_{i,j} \tag{2.32}$$

where $\lambda = \hbar/(\sigma\sqrt{m\epsilon})$ is the De Boer quantum parameter, which quantifies the relative contributions of kinetic and potential energies, approximated by the sum over all pairwise interactions $\nu_{i,j}$. The constants σ and ϵ represent the core radius and the depth of the potential well in the Lennard-Jones 6-12 potential:

$$V(r) = 4\epsilon\left[\left(\frac{\sigma}{r}\right)^{12} - \left(\frac{\sigma}{r}\right)^{6}\right]. \tag{2.33}$$

Notably, λ increases for lighter particles and shallower potential wells (smaller ϵ). For example, the values of λ^2 are: 0.241 for ^{3}He, 0.076 for H_2, 0.0049 for Ne, and 0.0027 for Ar. A higher λ value indicates a softer solid, thus less perturbation on the guest molecules resulting in minimal shifts in the absorption or emission lines of the trapped species.
In addition to structural characteristics, the density of states in solid p-H_2 is remarkably sparse for a molecular solid. The rotational constant B is a parameter that quantifies the spacing between rotational energy levels as $E_J = BJ(J+1)$ where J is the rotational quantum number. For parahydrogen $B = 60.853\ cm^{-1}$. The fundamental vibrational wavenumber is 4401.2 cm^{-1} and quantifies the lowest vibrational transition. All those parameters affect the density of state as it is connected to the spacing distribution of the energy levels and to the vibrational wavenumbers, all of which are higher for p-H_2 than for of other molecules [89].
Furthermore, the Debye temperature, which reflects the lattice vibration in terms of temperature, is approximately 100 K. This Debye temperature is lower compared to that of many other molecular solids. A higher Debye temperature suggests that the matrix material can support a higher range of phonon frequencies, negatively affecting the insulation of the guest molecules.
Another important advantage in p-H_2 spectroscopic studies is related to its optical clarity, even in crystals of a few mm of thickness [90]. However, reaching these outstanding characteristics requires generating the purest possible crystal.

Growth of a pure crystal

In nature hydrogen H_2 exists as combination of approximately o-H_2 at 75% and p-H_2 at 25% when at room temperature.

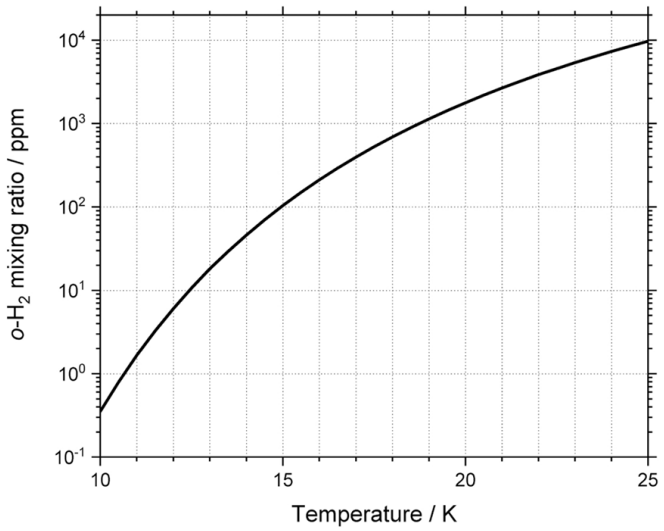

Figure 2.18: Simulation results of mixing ration of orthohydrogen presence in a parahydrogen gas after conversion at different temperatures. Taken from [83],

The initial apparatus designed in 1933 for the conversion of ortho-H_2 to para-H_2 consisted of a tube packed with an activated charcoal catalyst [91]. Activated charcoal, with its high surface

area and porous structure, acts as a catalyst for the ortho-para hydrogen conversion. On its surface, hydrogen molecules interact with the cold carbon atoms through mechanisms like spin-orbit coupling, redistributing the spins of the hydrogen gas at lower energy states. This improves the thermal coupling of the gas, thereby accelerating the conversion process from ortho-H_2 to para-H_2. The tube was submerged in a cryogenic fluid, typically liquid nitrogen, to achieve a higher enrichment of p-H_2, that would otherwise be very slow.
At low temperatures, where H_2 exists only in $J = 1$ and 0, the fraction of ortho-para hydrogen is expressed by a two level Boltzmann distribution as:

$$f = 9e^{-170.5/T} \tag{2.34}$$

where 9 is to take into account nuclear and rotational degeneracies, 170.5 K is the energy separation between $J = 1$ and 0 and T is the catalyst temperature. A simulation of how the catalyst temperature affects the ortho-para conversion in shown in Figure 2.18.
Currently, the leading technique to convert orthohydrogen to parahydrogen is the one introduced by Fajardo et al. [92] using a cryostat cold head. The conversion process involves the following steps:

- A coiled copper tubing winds downward around a solid piece of oxygen-free high conductivity copper (right side of Figure 2.19), passes through the center adjacent to the cold head, and then attaches to the outgoing stainless steel tubing.
- The tubing can be filled with an hydrous ferric oxide catalyst and is then immersed in a cryogen, such as liquid nitrogen or liquid hydrogen, to lower the temperature and achieve higher para enrichment.
- Hydrogen gas is introduced into the tube (red arrow on the left of Figure 2.19), and the backing pressure is adjusted so that the gas is forced to flow through the catalyst.

An illustration of the conversion setup used in the work of K. Sundararajan et al. [88] is shown in Figure 2.19.

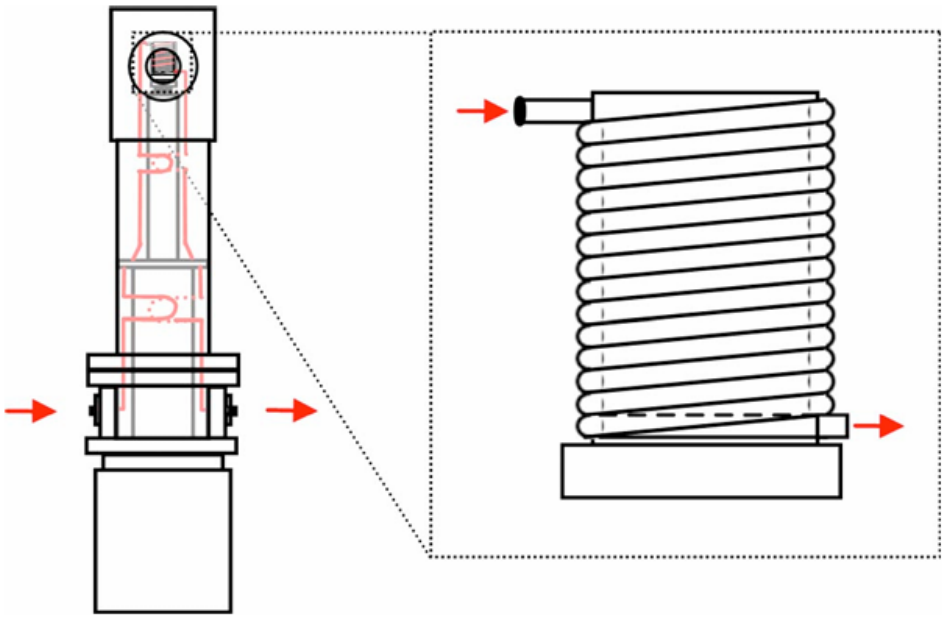

Figure 2.19: Left: An overview of the para-H2 converter. The red line highlights the hydrogen flow inside the converter. Right: A closeup of the coil section where the catalytic conversion occurs. Figrue taken from [88].

As hydrogen gas flows through the catalyst at cryogenic temperatures, the orthohydrogen molecules are converted to parahydrogen. The efficiency of this conversion increases with decreasing temperature, making liquid hydrogen the preferred cryogen to achieve nearly pure parahydrogen.
When a good concentration of parahydrogen is obtained, with orthohydrogen presence reduced from a few percentage down to 0.01% [90], the next step is to form a solid parahydrogen crystal. The rapid vapor deposition technique is commonly employed for this purpose and involves the following steps:

- The parahydrogen gas is introduced into a vacuum chamber.
- The gas is rapidly cooled and deposited onto a cold substrate, typically attached to a cold finger at temperatures around 4 K.
- The deposition rate is controlled to ensure the formation of a high quality crystal with minimal defects, with a flow rate ranging from few dozens up to 400 SCCM (Standard cubic Centimeters per Minute).

The rapid cooling and deposition process helps to preserve the high parahydrogen content and form a solid crystal. The resulting solid parahydrogen matrix is highly transparent and exhibits minimal interaction with guest molecules.
Once the setup to form a pure parahydrogen crystal is set, doping of its structure with the molecule or atom of interest can be achieved by simultaneously growing the crystal while directing a low energy molecular beam on it. This method ensures that the parahydrogen crystal incorporates the molecules or atoms from the beam, resulting in a precisely doped parahydrogen crystal.

Chapter 3

BaF ion beam production

In this chapter, an overview of the experimental setup I used during my thesis work to produce an ionized barium monofluoride (BaF) beam is provided, followed by a discussion of the data obtained to characterize and optimize its production. Based at the INFN Legnaro laboratories, near Padova, Italy, this new setup is currently under investigation by the PHYDES collaboration, which aims to perform eEDM measurements using the matrix isolation technique by embedding BaF molecules into a cryogenic parahydrogen (p-H_2) crystal. Therefore, the goal of this study is to achieve a molecular beam with high density of BaF molecules, which is a significant and necessary challenge for eEDM measurements using the matrix isolation technique.
A similar design has already been briefly described in the simulations conducted in [93]. However, this new setup includes modifications related to the characterization of the beam both before and after production.

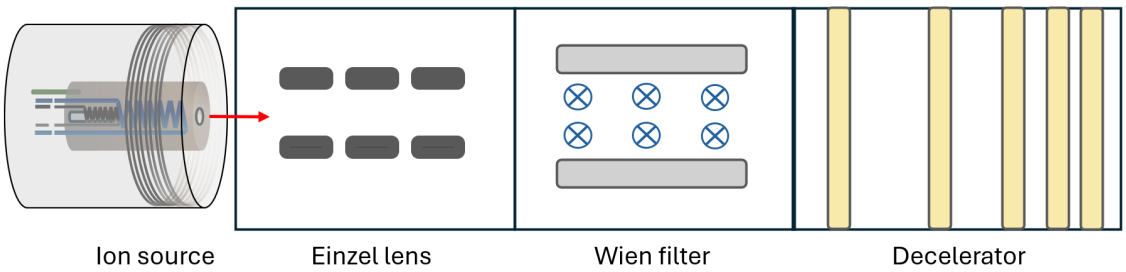

Figure 3.1: Schematics of the ideal BaF^+ beam production system of the PHYDES collaboration. The beam will be produced through a an arc plasma ion source. An Einzel lens is used to focus the beam trajectory, a Wien filter to achieve a beam composed solely of BaF molecules and a decelerator to reach slow speed necessary to embed molecules in a cryogenic crystal for eEDM measurements. In this work, only the ion source and Einzel lens have been analyzed.

The objective of the production setup is to generate a stable beam with a high density of ionized BaF^+ molecules using a plasma discharge ion source. These molecules will then. in future experiments, be embedded in a parahydrogen crystal. To achieve this goal, the apparatus has been characterized and analyzed using a Residual Gas Analyzer (RGA 200) [94], a Faraday cup, and a grid-shaped Faraday cup, shown in Figure 3.6. These instruments are essential for optimizing the production of BaF ions and establishing an ideal operating setup that maximizes molecule production over a span of several hours. Moreover, the RGA detector enables comprehensive characterization of the beam as BaF is not the only component in the produced beam, allowing for a detailed analysis throughout the production process.

3.1 Ion source setup

The production of BaF ions occurs within a vacuum chamber system and the PHYDES ideal setup includes several key components:

- plasma discharge ion source for the molecular ion beam production of BaF ions;
- Einzel lens and deflectors to focus and direct the ion beam;
- Wien filter to eliminate any residual ionized gas from the molecular beam;
- decelerator.

A schematic view of the apparatus is illustrated in Figure 3.1. For the initial characterization of the ion beam in this study, only the ion source and Einzel lens were utilized, as the additional components were not required.

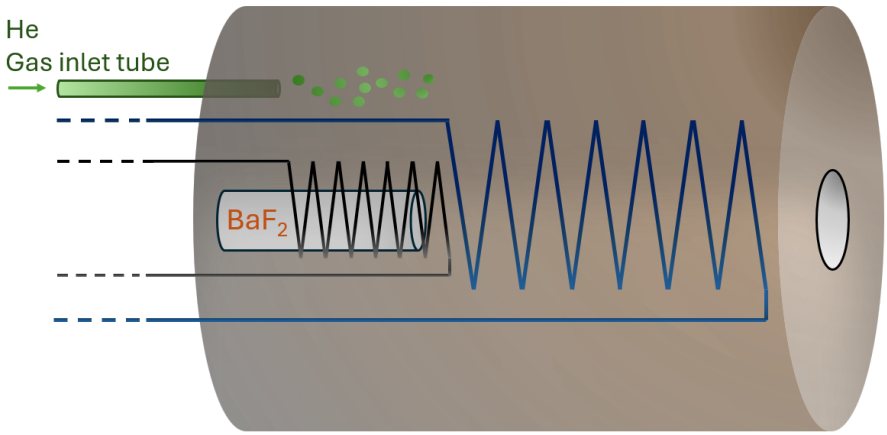

Figure 3.2: Schematics of the ceramic chamber where the generation of the molecular ion beam takes place through a plasma discharge. The BaF_2 powder is inside a cell (grey box) surrounded by the oven filament (black) to thermalize the BaF in gas phase. The ionizer gas (He) inlet is shown in green, while the filament to activate the plasma is in blue. At the extraction point an anode with a hole is present.

The ion sources cell is shown in Figure 3.2. It is contained in a chamber with a ceramic coating and is characterized by two concentric winded filaments shown in Figure 3.3. The first, referred to as the 'oven', is used to to heat and evaporate the BaF_2 powder contained in a small cell. The second filament triggers the plasma discharge. Molecules are extracted through a 2 mm-diameter aperture at the anode, which can be set to voltages from a few V up to kV.
Helium has been selected as the activation gas of the plasma discharge, since an effective and quick plasma discharge can be achieved with a sufficient energy to ionize the BaF molecules. The ion source is filled with helium through a gas inlet, therefore a dynamic vacuum inside the chamber is generated, requiring constant pressure monitoring using a Pirani gauge. The ion source is filled with He at approximately $P_{in} = 10^{-1}$ mBar measured at the gas inlet, while the vacuum chamber, at the ion source exit, is maintained in a high vacuum regime of approximately $P_{ch} = 10^{-5}$ mBar through a turbo-molecular pump.
Once a minimum constant entrance pressure $P_{in} = 1.5 \times 10^{-1}$ mBar is reached, the activation filament of the plasma can be turned on. At 11.5 A and 14.5 V, close to the maximum allowed power, the filament set the activation gas in optimal condition to initiate the plasma discharge process. Once the gas is thermally ionized by the filament and the anode is set to desired voltage, a high voltage U_{plasma} is applied between the plasma filament and the anode. This high voltage induces a cascade of ionization processes (Townsend breakdown), allowing the system to enter

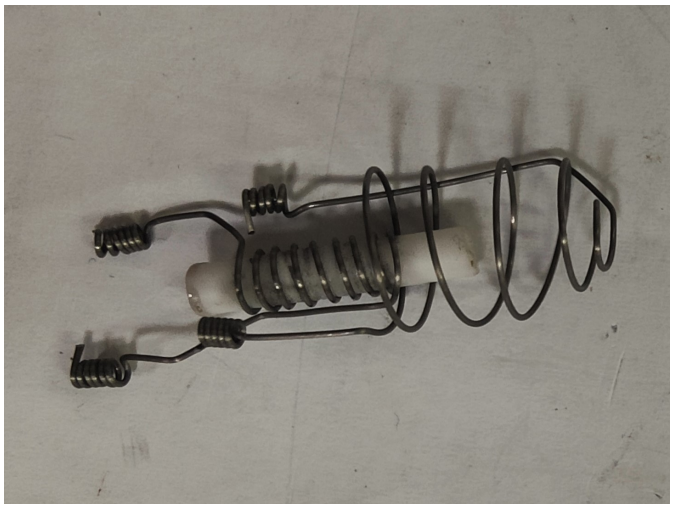

Figure 3.3: The oven filament surrounds a small tube containing BaF_2, with the plasma-activating filament positioned above. They measure just just 2x1x0.5 cm and are housed inside the ceramic chamber of the ion source.

the glow discharge regime of the plasma. At this stage, ions are accelerated towards the anode. By measuring the current on the anode, an estimation of the plasma current can be obtained. Typically, a plasma current of a few hundreds mA is measured.
When the plasma current is detected and consequently the plasma is active and stable, a molecular beam is generated and extracted from the anode hole. At this stage, the oven ca be turned on to introduce BaF into the molecular beam. Inside the oven filament a sample of BaF_2 is vaporized into the gas phase and thermally dissociates primarily into BaF + F. Our molecule of interest, BaF, interacts with the plasma electrons and ionizes into a BaF^+ molecules. During the heating process, particular attention is given to gradually increasing the voltage of the oven filament, as a rapid emission of molecules from the sample is not ideal for the final purpose of achieving a doped crystal with a high density of BaF. By taking these precautions, a maximum BaF production duration of a a few hours has been achieved.

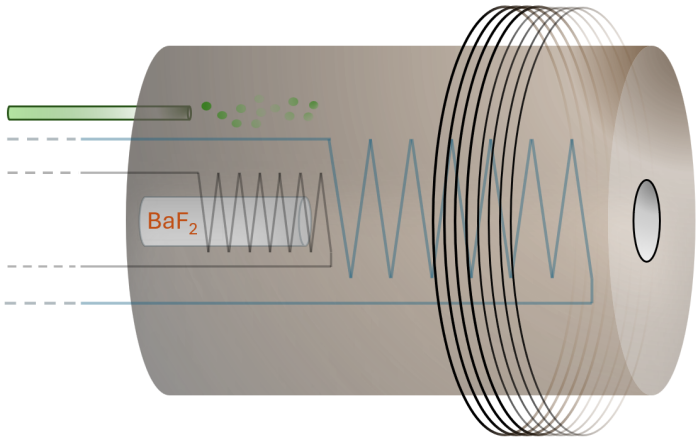

Figure 3.4: Illustration of the solenoid surrounding the ion source chamber. The solenoid is composed of 168 turns and can sustain a current of 5 A, reaching a maximum magnetic field of approximately 100 Gauss.

3.2 Magnetic field confinement

The entire process of molecular beam production occurs under the influence of a magnetic field generated by a solenoid surrounding the ion source chamber, as shown in Figure 3.4.
The 168-turns solenoid can sustain a maximum current of 5 A, generating a magnetic field of approximately 100 Gauss can be generated. A measurement of the magnetic field at the center of the solenoid was performed using a three-dimensional magnetic field detector. The results are shown in Figure 3.5. Although a magnetic field could in principle enhance the ionization process [95], in this case its function is to facilitate the ion beam extraction. The effect of the solenoid's

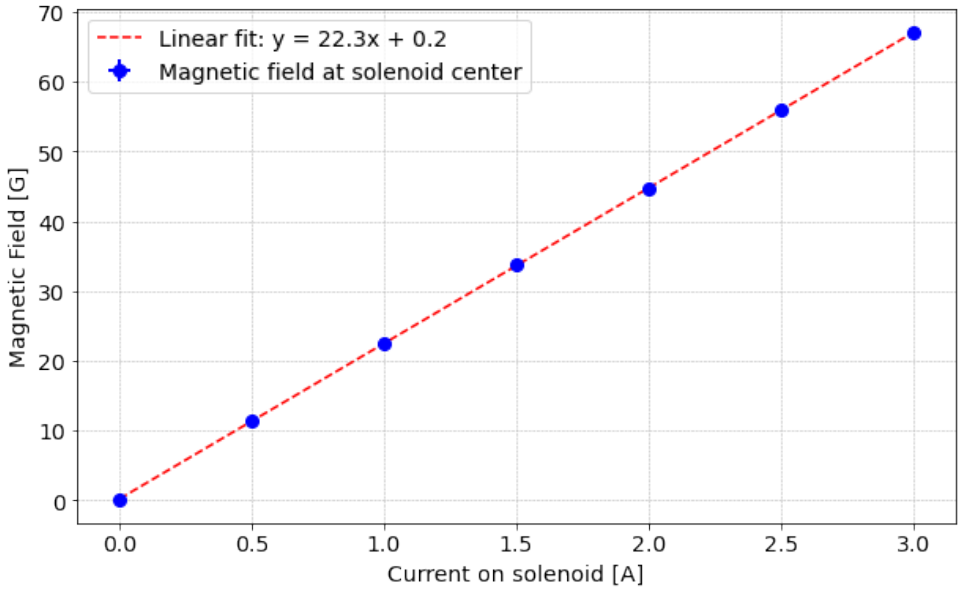

Figure 3.5: Measurement of the magnetic field amplitude at the center of the solenoid embedded in the source to optimize the ion beam extraction. A linear fit to the data provides a direct relationship between the magnetic field affecting the molecular beam and the current applied to the solenoid. The linear fit resulted in $y = 22.3x + 0.2$, where y represents the magnetic field in Gauss and x denotes the current in Amperes applied to the solenoid.

magnetic field was studied when the vacuum pressure of $P_{ch} = 2 \times 10^{-5}$ mBar was reached. The plasma current was maintained at $I_{plasma} = 300$ mA by setting the plasma filament at 11.5 A and 14.5 V and the high voltage $V_{plasma} \approx 100$ V. The molecular beam current I_B was measured through a grid, shown in Figure 3.6, positioned at 20 cm from the extraction point of the source. By varying the current flow through the solenoid (I_S), we determined the optimal magnetic field value to focus the beam out of the anode hole. The results, depicted in Figure 3.7, indicate a maximum at $I_{S-max} = 2.7$ A when reaching $I_{beam} = 336$ nA.

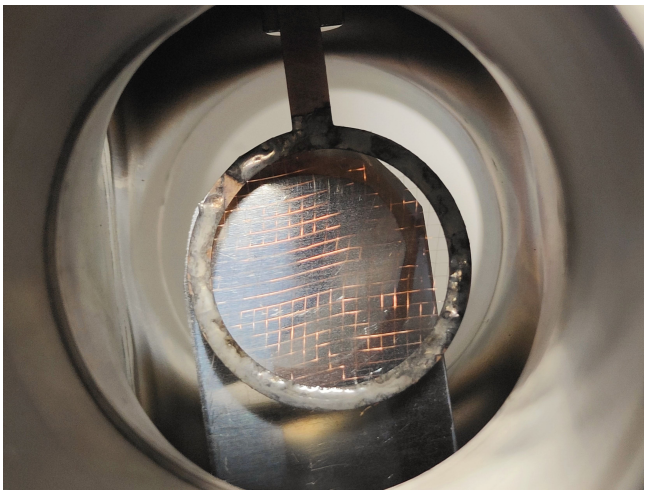

Figure 3.6: Beam current measurement tools: a copper grid developed at the LNL INFN laboratory, which allows for intercepting only a fraction of the current flowing to the target crystal, and behind it a flat beam dump to measure the total current. Both these experimental components can be moved away from the beam.

The results align well with the study presented in [35], which suggests an optimal magnetic field of the order of several hundred Gauss for a plasma current of a few Amperes. In our setup, with a lower plasma current, the optimal value was found to be $I_{S-max} = 2.7$ A, corresponding to an optimal magnetic field of $B_{max} = 60.4$ G.

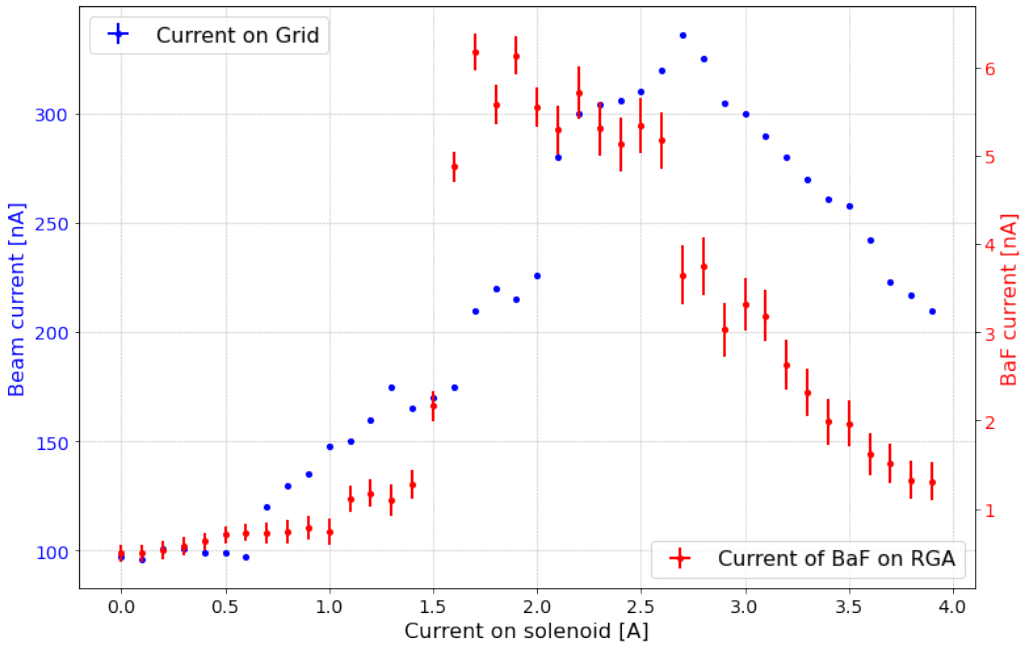

Figure 3.7: Optimization measurements of the magnetic field of the solenoid installed in the ion source. The BaF current has been later measured with an SRS RGA200 and shows a maximum at $I_{S-max} = 1.7$ A. For the following measurement this was the selected current on the solenoid.

It should be noted that at $I_S = 1.6$ A, the plasma began to exhibit instability. Consequently, the high voltage U_{plasma} was adjusted to reestablish a stable plasma condition at around $I_{plasma} =$ 400 mA. This instability did not significantly impact the overall measurement, as an increasing beam intensity was already observed at lower values of I_S. Moreover, the plasma current was set

to $I_{plasma} = 430$ mA when $I_S = 2.9$ A, but again the decreasing trend behaviour of the beam current is only slightly affected by those changes.

3.3 Einzel lens analysis

Once extracted from the ion source, the beam needs to be collimated before entering a Wien filter, a decelerator and final deposition on the cryogenic matrix. For this purpose, an Einzel lens is used. In this thesis, a study of the beam focus settings in combination with different source parameters has been conducted and is reported in this section.
These lenses utilize electric fields to collimate ion beams while conserving their energies. A detailed analysis of the trajectory with a similar ion source setup, but different lens and with two deflectors, can be found in [93], along with simulations of ion beam trajectories.

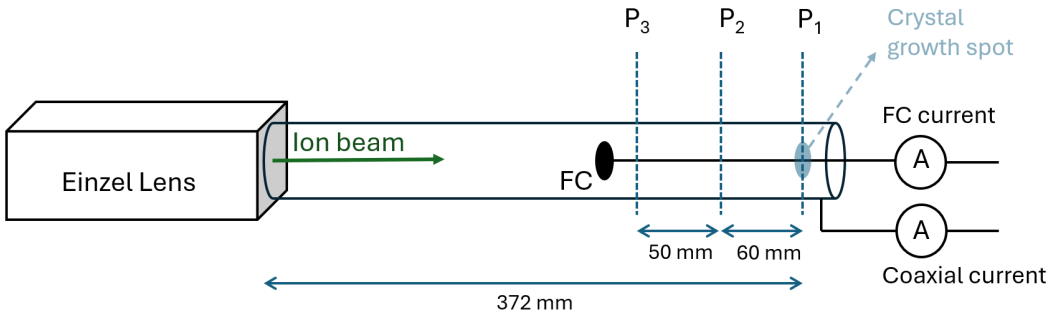

Figure 3.8: A schematic of the setup to characterize the Einzel lens focusing over an ion beam. The setup simulates a realistic position of a chamber for crystal growth, where P_1 is the Crystal growth position, P_2 is the chamber entrance and P_3 is the outside of the chamber.

A movable Faraday cup (FC) with a diameter of $d = 13$ mm was positioned right after the Einzel lens, with the possibility to move it along the beam direction, covering a total distance of 110 mm. The setup was studied to simulate the focus of the beam between 3 points. Assuming an hypothetical setup where the source and lens are directly connected to the crystal growth chamber, the three points indicates

- P_1: crystal growth position, distance from Einzel lens output $D_1 = 372$ mm;
- P_2: chamber entrance (60 mm from P_1), $D_2 = 312$ mm ;
- P_3: outside of the chamber (110 mm from P_1), $D_3 = 262$ mm.

A schematic of this setup is shown in Figure 3.8.
Two main measurement have been carried out, using same ion source settings but with different values of anode voltage $U_A = 100$ V and $U_A = 36$ V to study the efficiency of the lens at the lowest possible ion energies achievable with this ion source. The ion source operational parameter were, for both measurements, of $P_{ch} = 8 \times 10^{-6}$ mBar, plasma filament at 16 V and 12 A and $U_{plasma} = 90$ V with a plasma current of $I_{plasma} = 30$ mA. Throughout the experiments, the high voltage required multiple adjustments due to high instability of the plasma.
In Figure 3.9 we report the measured current on the Faraday cup I_{FC} for multiple lens voltages U_L, to determine the focusing path and voltages at three different positions. As the molecular beam might be out of focus at each distance investigated, the current on the coax tube covering the Faraday cup I_coax was concurrently measured.

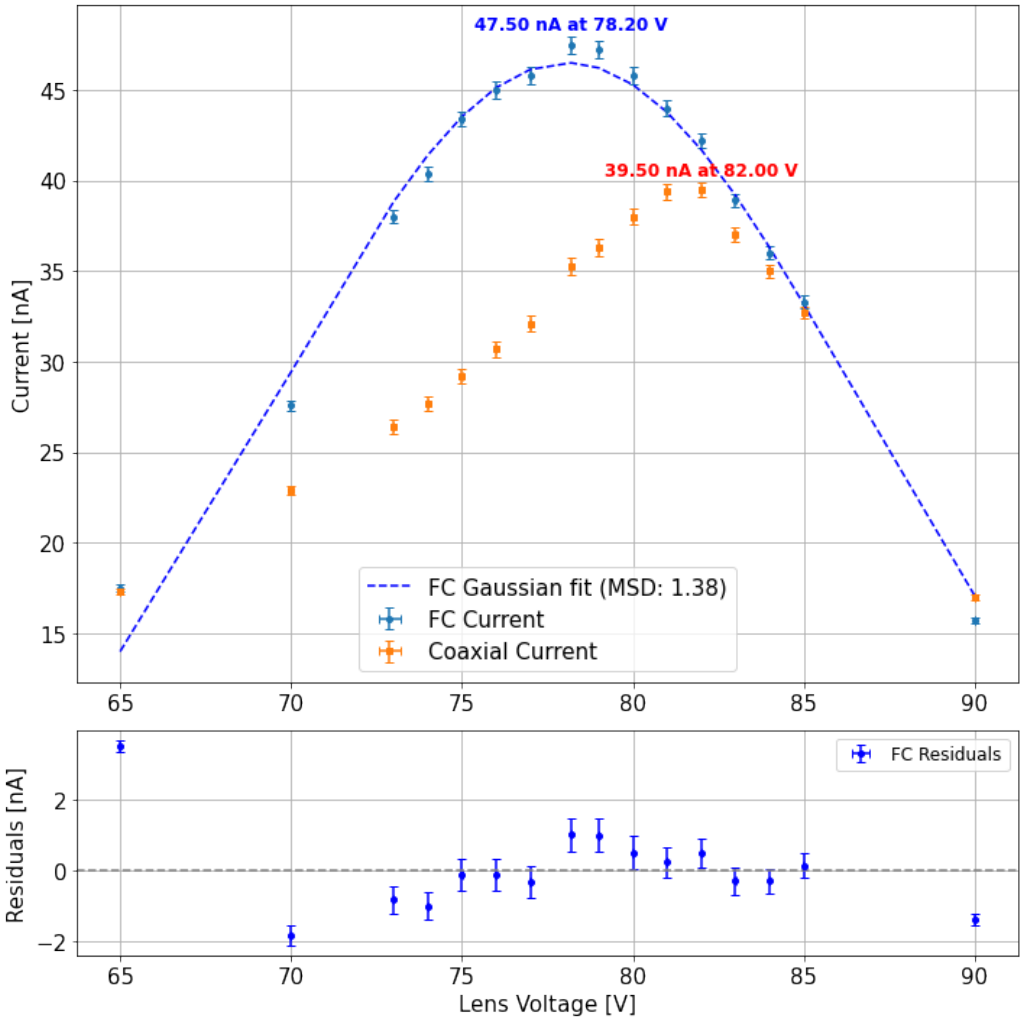

Figure 3.9: Measurement of Einzel lens voltage to focus the molecular beam produced at $U_A = 100$ V on the hypothetical crystal growth site, at $D_1 = 372$ mm from lens exit. A Gaussian fit of the FC current shows the Gaussian profile of the ion beam with good approximation ($MSD = 1.37$). Residuals of the fit are shown in the lower plot.

All measurements have been carried out following the same procedure:

- U_A is set at the desired value: $U_A = 100$ V or 36 V;
- the Faraday cup is moved in one of the three spots: D_1, D_2 or D_1;
- by varying U_L, a scan to find the optimal focus lens voltage is done.

One of the measurement results is displayed in Figure 3.9, where the Faraday cup and coaxial current are displayed in blue and orange, respectively. Similar to the expected results [93], the molecular beam is focused on the crystal site for $U_L = 78.2$ V, which is around 80% of the anode voltage. However, the lens voltage must be adjusted very carefully. As shown in the plot, for $U_L = 82.0$ V, the beam intensity drops by about 20% and the maximum coax current is observed.

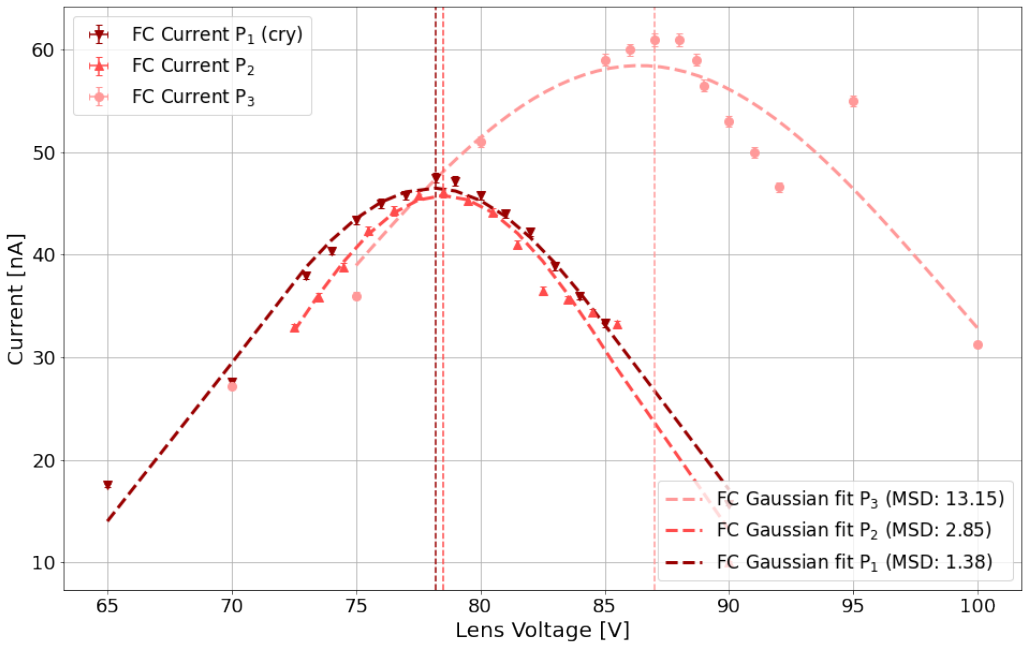

Figure 3.10: Einzel focusing anode with $U_A = 100$ V studied at the expected cryocrystal position surface and at distances 60 mm, 110mm from it. The vertical dashed lines indicate for each data series the point of maximum current. Darker colors were chosen to indicate measurements conducted at positions closer to the crystal site, both for Faraday cup (red) and coaxial currents (blue). The bad Gaussian fit of the FC current on sit P_3 indicates that, most probably, plasma fluctuations affected the measurements when $U_L > 87$ V.

The results of three measurements taken with $U_A = 100$ V are displayed in Figure 3.10. Note that the difference in optimal Einzel lens voltage U_{L-max} between point D_3 and D_2 is $\Delta U_{L-max_{2,3}} = 8.5$ V, while $\Delta U_{L-max_{2,1}} = 0.3$ V (D_2 - crystal site). This result indicates that the Einzel lens is not effective to collimate the beam for distances greater than D_2. On top of that, the difference between Faraday cup and coaxial current diminishes, with the coaxial current being only 18.0% and 25.68% less than the Faraday cup current at distances D_2 and D_1, respectively. This is approximately half of the 40.89% difference observed when measuring closer to the lens at D_3. From the collected data, a distance difference of 110 mm, starting from 262 mm from the lens, results in a 25.7% loss of beam intensity when $U_A = 100$ V.
Results shown in Figure 3.11 illustrate the optimal voltage for the Einzel lens with respect to the distance from the lens output and the anode voltage. As seen in the previous analysis, for both anode voltage settings, it seems that after the second Faraday cup spot, the lens starts loses its focusing capabilities, as the last two positions do not show a significant change in beam current compared to the initial position.
Moreover, when 36 V are applied on the anode, the second position has an optimal lens voltage grater than the third one, on the crystal. As displayed in Figure 3.12, an unexpected behaviour is observed, where the coaxial current is greater than the Faraday cup current throughout the whole measurement. Moreover, its trend increases without reaching the maximum point as in previously reported current vs lens voltage plots (Figure 3.9 and 3.10). These inconclusive results can be ascribed to the large instabilities of the plasma current observed during the measurements, that led us to analyse a wrong interval of the lens voltage.

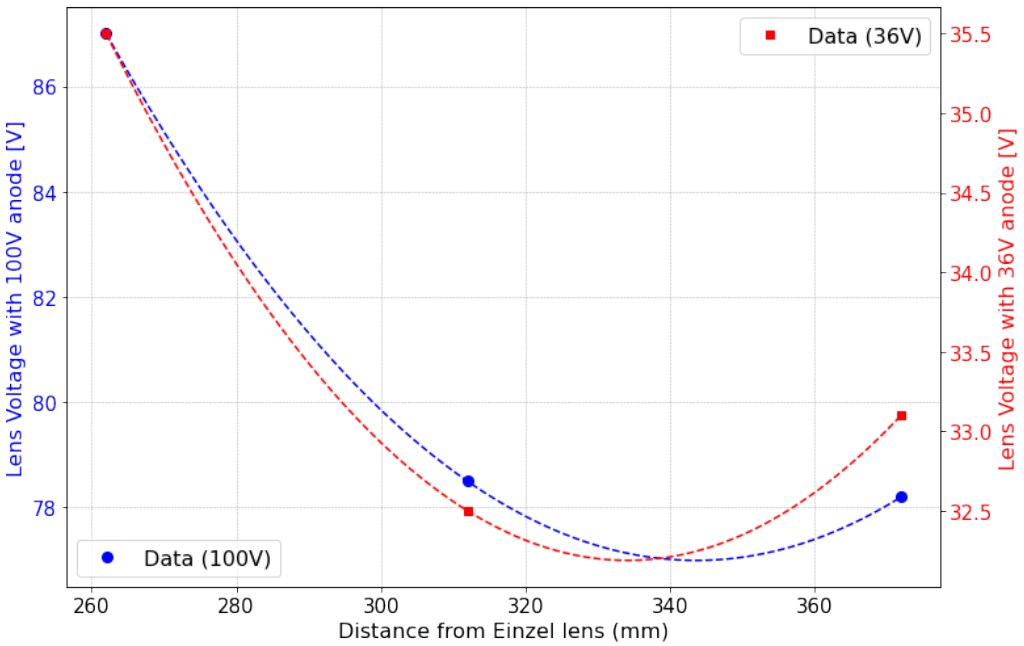

Figure 3.11: Optimal focusing lens voltage with corresponding distance from the output of the lens. Note that for different anode voltages (blue: $U_A = 100$ V, red: $U_A = 36$ V), correspond a different y-axes representing the Einzel lens voltage. A quadratic fit shown through a dotted line is used to guide the reader through the descending behaviour of the data.

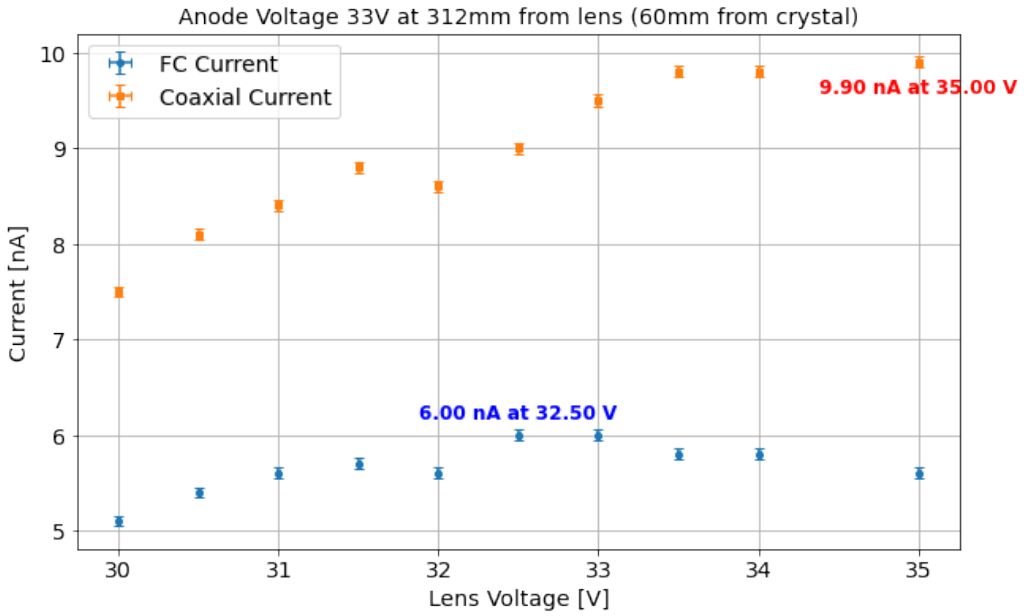

Figure 3.12: Measurement of Einzel lens voltage to focus the molecular beam produced at $U_A = 36$ V at 5 mm from the hypothetical crystal growth site, at $D_1 = 312$ mm from lens exit.

However, the reduction in beam intensity observed at higher lens voltages (25.71%) is diminished to 9.9% over the same distance, as shown in Figure 3.13. This behavior aligns with the Einzel lens working principle which is more effective with low-energy ions [96], thus providing better focusing and more precise control of the ion beam at $U_A = 36$ V.

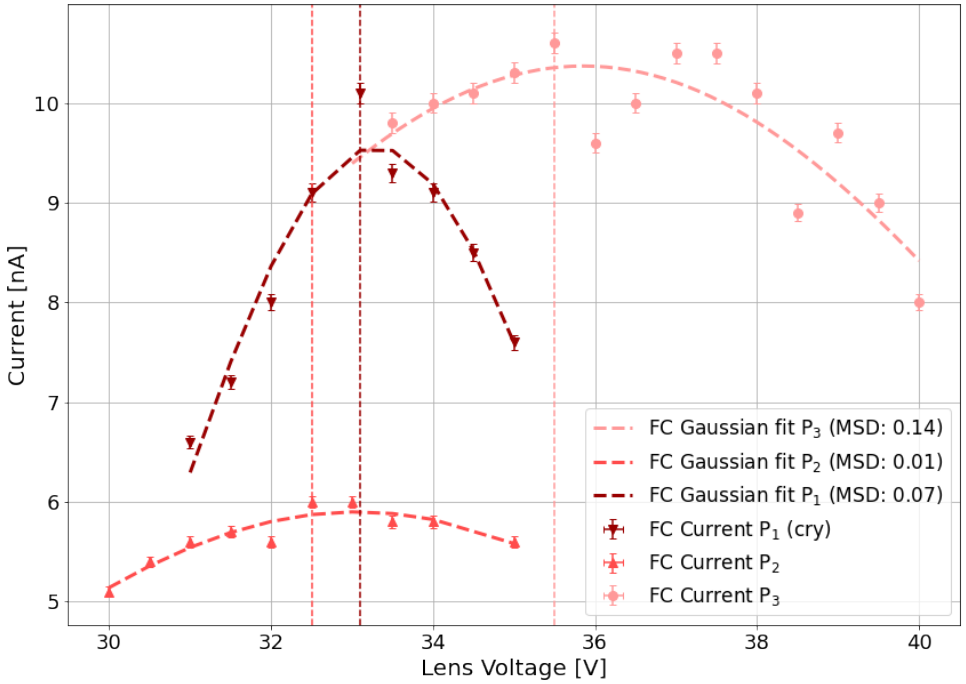

Figure 3.13: Einzel focusing anode with $U_A = 36$ V studied at the expected cryocrystal position surface and at distances 60 mm, 110mm from it. The vertical dashed lines indicate for each data series the point of maximum current. Darker colors were chosen to indicate measurements conducted at positions closer to the crystal site.

3.4 RGA 200 mass analysis

The Residual Gas Analyzer (RGA) 200 [94] is a mass spectrometer that can be connected directly to vacuum chambers to analyze the composition of gases inside of them. It is based on a quadrupole mass filter that separate ions by their mass-to-charge ratio. Here, a detailed description of the RGA 200's working principle will be given, focusing on the quadrupole mass filter and the process of signal acquisition and spectrum generation. The measured spectra of the BaF ion source are then analyzed.
The RGA is mainly divided into two components, an electronics control unit (ECU) and a quadrupole probe. The quadruple probe is engineered to act as a mass spectrometer sensor and

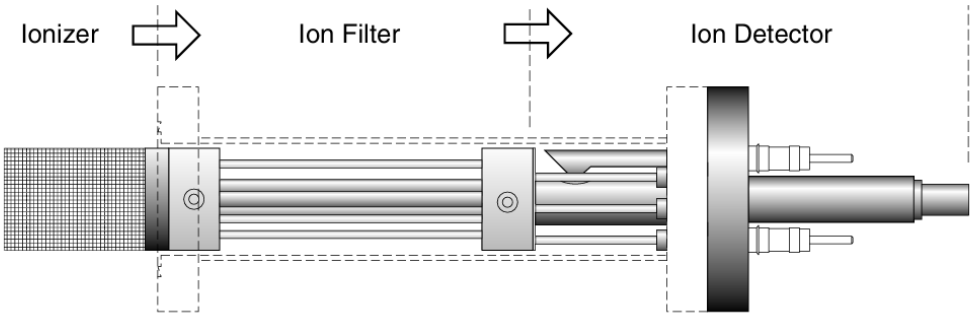

Figure 3.14: Schematic representation of quadrupole probe of the RGA that is directly connected to a vacuum chamber. The ions flow goes from left to right.

is directly connected to the vacuum chamber, at the exit of the ion source, with the ionizer (see Figure 3.14) protruding inside the chamber where the residual gases need to be analyzed. The ionizer, which allows for mass filtering through the quadrupole, is composed of a repeller,

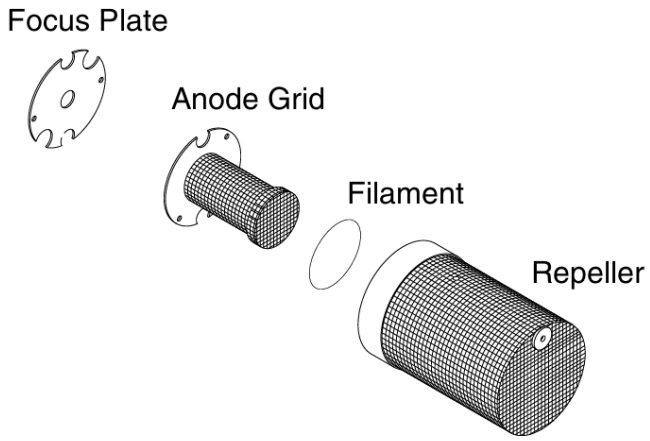

Figure 3.15: Ionizer components. Electrons that do not immediately ionize molecules are decelerated and re-accelerated due to the electric field between the repeller and the anode grid. This circulation increases ionization efficiency by allowing multiple passes. Ions are then drawn to the center of the anode grid by the negative potential produced by the growing electron density. The formed ions are extracted by the electric field difference between the anode grid and the focus plate, which is at a negative potential relative to ground.

an anode grid, a filament and a focus plate. The ThO_2 filament serves as the electron source for ionizing gas molecules. It operates at a negative potential relative to ground and is heated to incandescence by an electrical current. The thermionically emitted electrons are accelerated toward the positively charged anode grid, which is shaped as an open wire mesh so that electrons can pass through it, and produce ions (at the next stage) by impact ionization. The ions are drawn to the center of the anode grid and extracted towards the filter by the electric field difference between anode grid and focus plate.
The quadrupole mass filter, illustrated in Figure 3.16, is the core component of the RGA 200, and comes right after the ionizer. It consists of four cylindrical rods arranged in a parallel configuration, held together by high purity alumina insulators. The quadrupole mass filter operates by applying a combination of direct current (DC) and radio frequency (RF) voltages to the rods. Opposite pairs of rods are connected to an applied potential:

$$V_{x/y} = \pm(U + V_0 \cos \omega t) \tag{3.1}$$

where U is the DC voltage, V_0 is the amplitude of the RF voltage, and ω is the angular frequency of the RF voltage. Ions enter the quadrupole along the z-axis and are subjected to forces in the x and y directions due to the applied voltages, respectively DC and RF voltage. Light ions, with a low mass-to-charge ratio, are able to follow the alternating component of the electric field. In the X direction, these ions will remain in phase with the RF drive, gaining energy from the field and oscillating with increasingly large amplitudes until they collide with one of the rods and become neutralized. Therefore, the Z direction functions as a high pass mass filter, meaning that only ions with higher masses will be transmitted to the other end of the quadrupole without striking the X electrodes.
Conversely, in the Y direction, heavy ions will be unstable due to the defocusing effect of the DC component. However, lighter ions can be stabilized by the alternating component if its magnitude and amplitude are sufficient to correct the trajectory whenever the amplitude tends to increase. Thus, the Y direction acts as a low-pass mass filter and only ions with lower masses will be transmitted to the other end of the quadrupole without colliding with the Y electrodes. Therefore, by carefully tuning these voltages, the quadrupole can selectively filter ions of a specific m/z ratio, allowing them to pass through to the detector while others are deflected away.
The electronics control unit regulates the RF and DC voltages applied to the quadrupole rods.

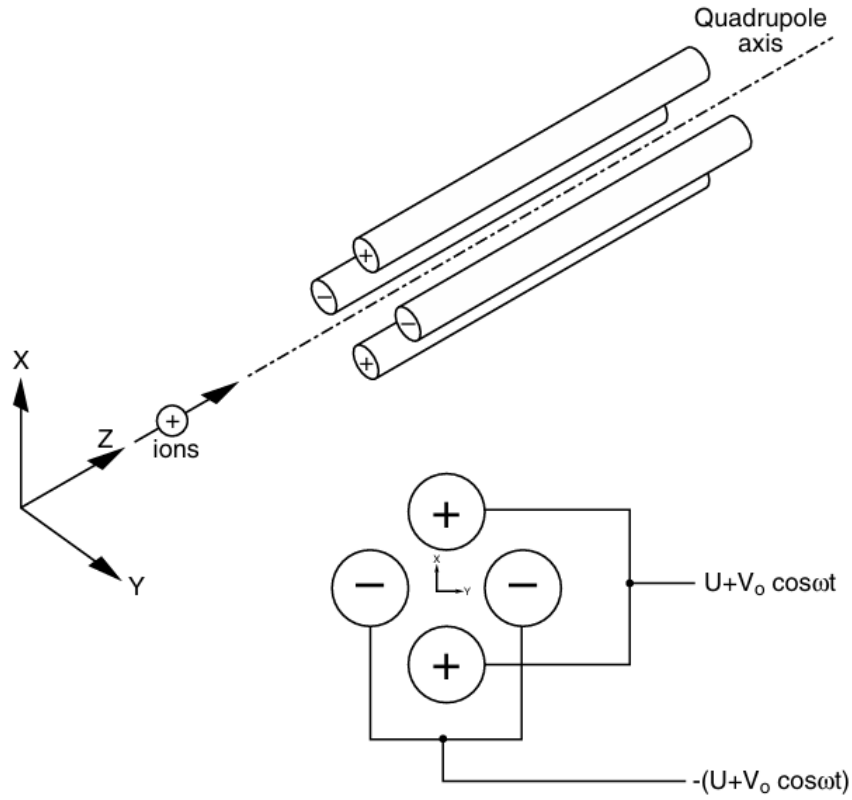

Figure 3.16: Schematic illustration of a quadrupole mass filter, depicting the arrangement and electrical connections of the four rods used to selectively stabilize or destabilize ion trajectories, allowing specific mass-to-charge ratios to pass through.

The ECU scans the voltages to produce a range of m/z values, generating a mass spectrum. This spectrum represents the ion signal intensity as a function of m/z ratio, providing detailed information about the gas composition in the vacuum system.
Once the ions pass through the quadrupole mass analyzer, they reach the ion detector. The detector in the RGA 200 is a Faraday cup, like in our setup, or an electron multiplier. The Faraday cup collects the ions and the resulting current of the filtered ions is measured. This current is proportional to the number of ions, and thus, to the partial pressure of the gas in the vacuum chamber
The detected signal is processed and displayed as a mass spectrum, showing the intensity of ion signals as a function of their m/z ratios. This spectrum allows for the identification and quantification of different gas species in the vacuum chamber.
The resolution of a quadrupole mass spectrometer, such as the RGA 200, is a characteristic that determines its ability to distinguish between ions of different masses and is affected by mass range, ultimate resolution and throughput characteristics.
The spectrometer used in the present work (mod. SRS RGA200) can detect ions in the mass range 1 to 200 amu, thus including the mass of the ion of interest, BaF, which corresponds to 157 amu.
Resolution and resolving power are key terms used to describe the performance of a quadrupole mass filter:

- **Resolution (Absolute Resolution)**: Defined as $M_{10\%}$, it represents the width of the pass band of the filter, specifically the full width at which the ion current falls to 10% of its maximum value. The unit of measurement is amu.
- **Resolving Power**: Expressed as $R = M/M_{10\%}$, it is the dimensionless ratio between a

particular mass M and $M_{10\%}$ at that mass.

For the RGA200 quadrupole, $M_{10\%}$ is preset to 1 amu.
The resolving power R at a given mass M is closely related to the DC/RF voltage ratio. Increasing the resolving power often leads to a reduction in the effective throughput of the filter, thus the sensitivity typically decreases at a rate of 1 to 1.5 times the rate of increase in resolving power.
A characteristic of quadrupole mass filters operated at constant resolution is that the throughput decreases with increasing mass. As $M_{10\%}$ remains constant, the resolving power $R = M/M_{10\%}$ increases with mass, reducing the filter's effective throughput for higher masses. This effect could result in an underestimation of the BaF ion current, which corresponds to a high mass of 157 amu.
In this work the software of the SRS RGA was used principally in the histogram mode, which displays the individual mass amplitudes for the selected scan range, usually set from 1 to 180 amu. This mode is particularly useful for visualizing the distribution of ion currents across different masses. The following is a description of how the software generates the histogram plot: In Histogram mode, the RGA head performs a peak-lock for each mass within the selected scan

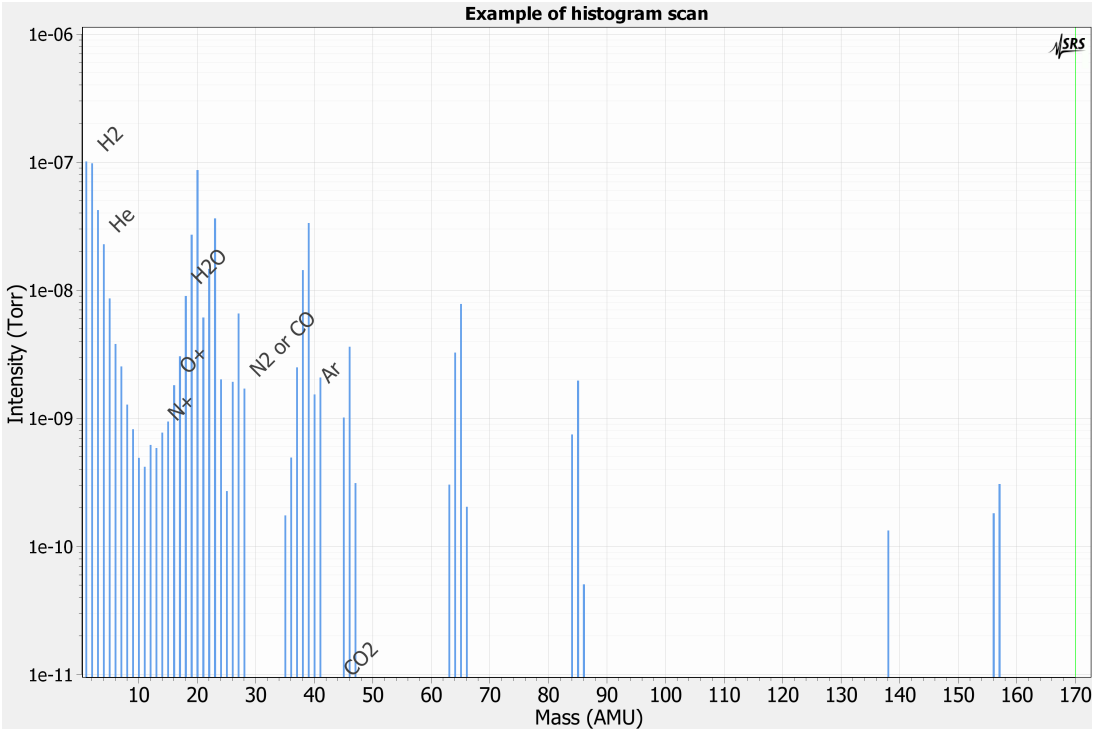

Figure 3.17: An histogram resulting from a measurement scan of the BaF ion source. The RGA software is also capable of labelling commonly known elements present in the ion beam.

range. The peak-lock process involves the following steps:

- For each mass, the RGA head conducts 7 measurements per atomic mass unit (AMU).
- The RGA head identifies the peak amplitude among these 7 measurements.
- This peak amplitude is then recorded as the representative value for that particular mass.

Once the peak amplitudes are determined, the software plots these values as bars in a histogram (see Figure 3.17). The X-axis of the histogram represents the mass range chosen before running the measurement. The Y-axis displays the partial pressure in Torr units of each mass measured, providing both a quantitative and a visual representation of the detected ion currents.

The time required to acquire each partial pressure measurement depends on the scan speed selected, for instance, each scan taken in this work usually took about 2 minutes.

RGA measurements

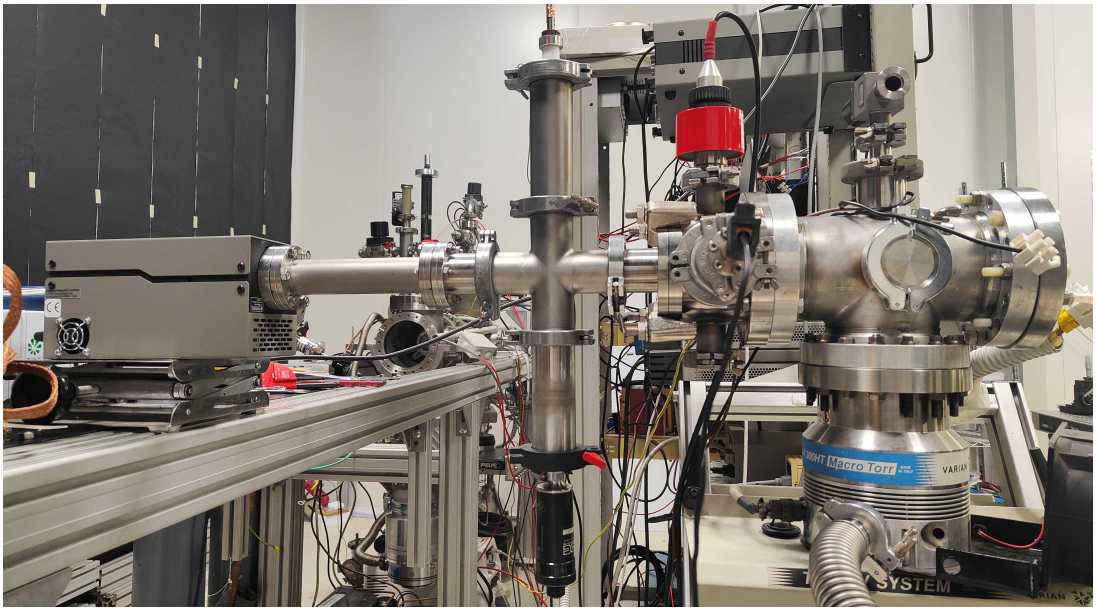

Figure 3.18: Setup used to take RGA spectrum of our BaF ion source. From right to left: The molecular ion source, where the BaF ions are produced, is positioned at the bottom right. The beam travels through an Einzel lens and then passes through a 4-way tube, where a grid Faraday cup and a movable Faraday cup are positioned. Finally the beam reaches the RGA200 connected to the 4 way tube.

In this study, all measurements taken with the RGA200 were performed with the configuration shown in Figure 3.18. The molecular beam emitted from the source is first focused by an Einzel lens. At its output, a 4-way cross hosts two movable Faraday cups (as in Fig 3.6). The flat one is used to measure the total beam current flow, while the grid shaped Faraday cup monitors the beam flow during the mass spectroscopy measurements. To check the initial level of vacuum, we typically record a spectrum with all components turned off except for the turbo molecular pump connected to the chamber (see Figure 3.18). In Figure 3.19 an overview of the residual gas components is shown, obtained with a pressure of $P_{ch} = 2 \times 10^{-5}$ mBar measured by the Penning gauge mounted at the chamber entrance (see Figure 3.18).
RGA scans are usually reported in Torr units (see Figure 3.17), as the software automatically converts the ion current detected into partial pressures through an internal conversion factor. However, for the analysis carried in this work, the scan was set back to Ampere units as we are interested in the amount of molecules. For instance, if a current of 1 μA is measured over 1 hour (3600 seconds), the total charge is $Q = 1 \times 10^{-6}\,\mathrm{A} \times 3600\,\mathrm{s} = 3.6 \times 10^{-3}\,\mathrm{C}$ and the total number of ions can be computed as:

$$N = \frac{3.6 \times 10^{-3}\,\mathrm{C}}{1.602 \times 10^{-19}\,\mathrm{C/ion}} \approx 2.25 \times 10^{16}\,\mathrm{ions} \tag{3.2}$$

As previously mentioned, while the Residual Gas Analyzer (RGA) provides good high mass spectrum sensitivity, it does not accurately measure the total ion current. To address this limitation, direct full current measurement with the RGA was not pursued. Instead, the lens focus was adjusted to the Faraday Cup (FC) position, which is closer to the lens and offers a more reliable measurement of the full ion current of the beam. The spectra obtained were subsequently normalized using this measurement.

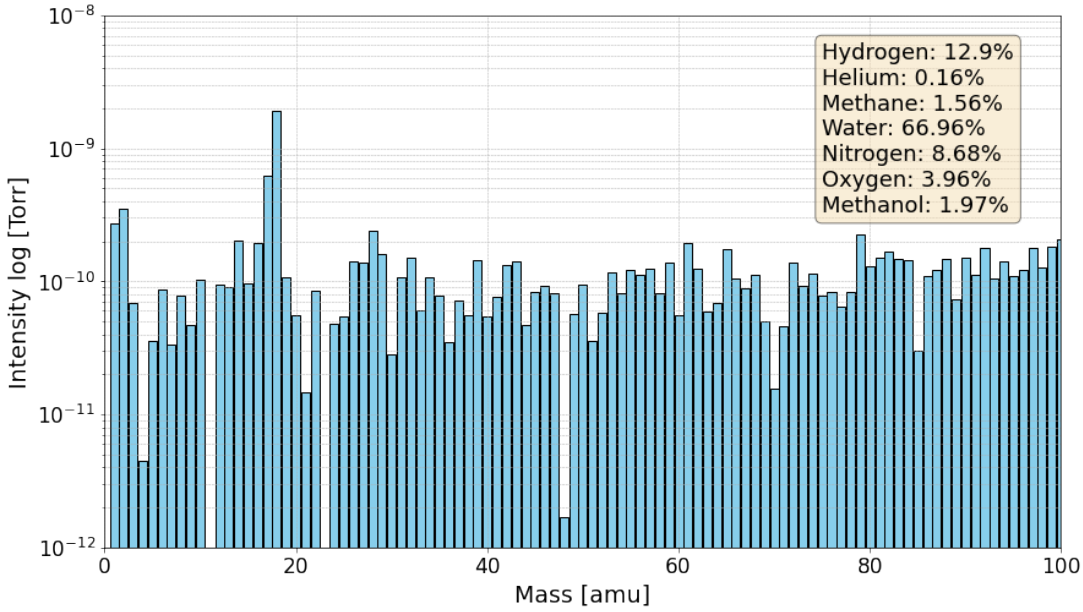

Figure 3.19: Vacuum residual gas analysis done with a vacuum of $P_{ch} = 2 \times 10^{-5}$ mBar. The RGA software remained in Torr units since measuring ion beam intensity was unnecessary, as the ion source was turned off.

The procedure followed to get the spectra with the ion source is:

- The ion source is activated and tuned to the optimal values obtained from the previous tests;
- Both Faraday cups are inserted into the four-way cross and a total current measurement is taken, along with a partial current taken with the grid;
- Only the grid is then left in place to control the stability and intensity of the molecular beam and a mass spectrum scan is initiated with the RGA200;

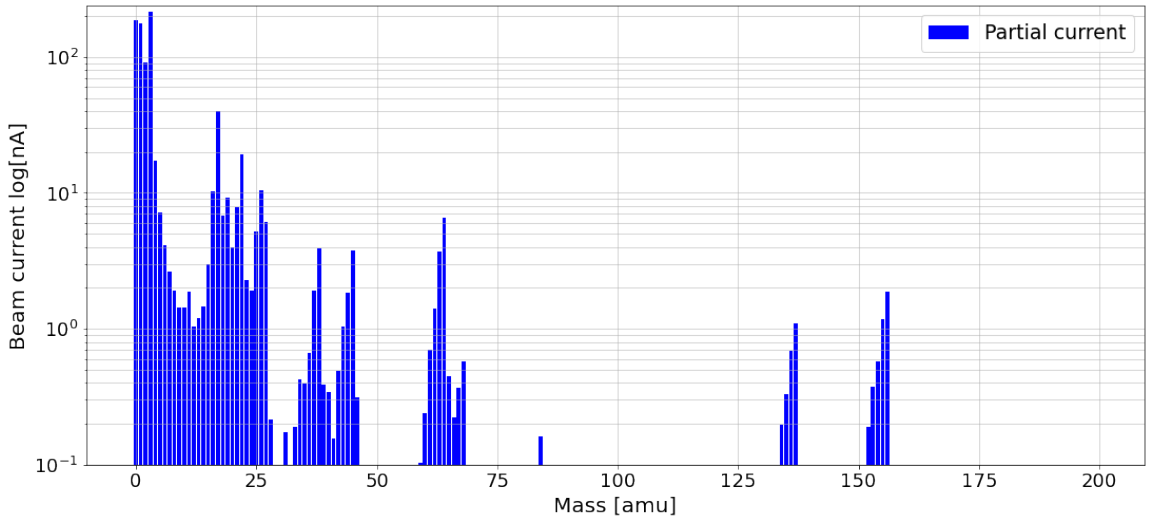

Figure 3.20: Mass spectrum of the molecular on beam after 2.5 hours. The plasma generated with Helium at $P_{in} = 2 \times 10^{-1}$ mBar was set at $I_{plasma} = 200$ mA. The oven filament was at 9 A, Einzel lens at 80 V and magnetic field filament at 1.7 A. Production of BaF from a few mg sample lasted more than 2 hours with this settings. BaF emission line are between 154 and 157 amu, depending on the isotope.

Due to plasma fluctuations, there was insufficient time to change the focus of the Einzel lens on the RGA. Consequently, the scan is taken immediately after the removal of the FC.
We conducted several scans to optimize the production of BaF. Throughout them, we focused on how the beam intensity was affected by the plasma intensity and stability. In one of the final measurements, where the molecular ion source operated continuously for over 2 hours, we gained valuable insights into the production rate of BaF molecules with our current setup.
The plasma was generated using helium at an entrance pressure of $P_{in} = 2 \times 10^{-1}$ mBar, with the plasma current set at around $I_{\text{plasma}} = 200$ mA. The oven filament operated at 9 A, while the Einzel lens voltage was maintained at 78 V as the anode voltage was set at $U_A = 100\ V$, and the magnetic field filament was set to 1.7 A. Under these conditions, the BaF production continued for over 2 hours. The BaF emission lines, ranging between 154 and 157 amu, depending on the isotope, are depicted in Figure 3.20.
BaF molecules are only a small fraction of the molecular beam generated in our setup. The beam is primarily composed of common vacuum component and helium, found in high concentrations as it serves as the plasma activator gas. In the range between 135 and 137 amu, the presence of Barium isotopes can be detected. This is a result of the evaporation process of the BaF_2 sample in the oven, which can evaporate as BaF + F and, to a slightly lesser extent, as BaF + F_2. To achieve a pure BaF ion beam, a velocity filter (Wien filter) will be utilized in future experiments. From these spectra, is possible to compute the beam current corresponding to BaF ions by summing the contributions of all BaF isotopes present in our sample, ranging from BaF_{154} to BaF_{157}. For future experiments, we plan to use a pure BaF_{157} sample, as it is the isotope of interest for eEDM investigations. The initial and final BaF currents were measured at $I_i = 5.54$ A and $I_f = 3.62$ nA.

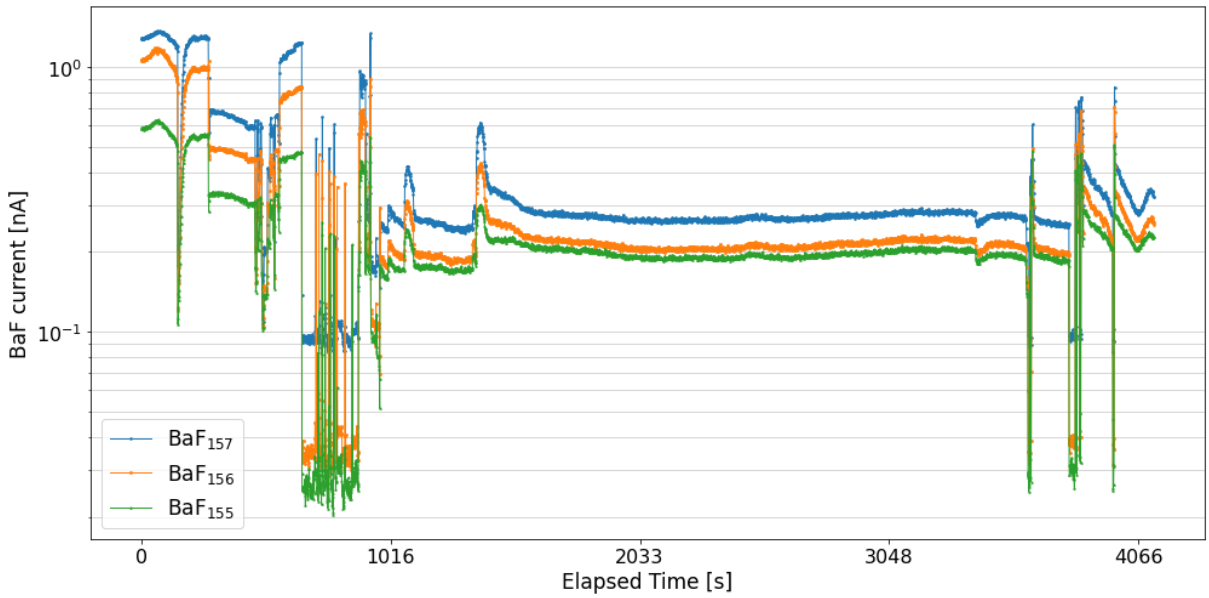

Figure 3.21: Time spectra achieved with RGA200 measured during the 2.5 hours run. Here we provide time to current data of the three most common isotopes of BaF, mainly BaF 155, 156, and 157. The latter one is the eEDM particle of interest. The big, although short in time, oscillations are due to plasma instability of the ion source. The total current of BaF was of 0.12 nA at the end of this scan.

Averaging these values, we estimate that during one hour of production, approximately a number of 8.15×10^{13} unfiltered BaF molecules can be produced per hour. However, this production rate was not constant throughout the entire measurement, as shown in Figure 3.21, where the BaF production is tracked over a span time of an hour. Presumably, shortly after the turning on of the plasma and oven filament, the BaF production dropped by one order of magnitude.

Unfortunately, due to the inability to normalize the current values during the time scan, we could not react immediately and fix the production issue. When a new mass spectrum was taken at the end of the one hour time spectra, the BaF production was found to be suboptimal, with a total current of only 0.12 nA. By increasing the oven filament, by adding 0.5 V, the production was reestablished to $I_f = 3.62$ nA.
It is likely that the oven filament was initially set too low and should have been gradually increased to a higher voltages leading to a more stable produciton of BaF molecules.
During the same time scan, several large but brief fluctuations were observed. These are due to plasma instability of the ion source. Even though this issue can be fixed by either adjusting the entrance Helium pressure P_{in} to higher values or fine tuning the high voltage U_{plasma} over the electrodes, new upgrade to the setup have to be considered in future experiments, such as a larger source chamber.

Chapter 4

Parahydrogen crystal production and characterization

Measurements of eEDM using the matrix isolation technique could enhance current sensitivity due to a high number of embedded molecules and good clarity of today's crystals. Recent experiments [28] shows that embedding BaF molecules, produced by laser ablation, in a neon crystal does not significantly perturb its optical transitions.
In the PHYDES project, we plan to embed BaF molecules into parahydrogen (p-H_2) crystal, as its exceptional characteristics (see Chapter 2.3.2) makes it an ideal host for molecular spectroscopy within the matrix isolation technique, with a combination that has never been utilized for eEDM measurements. Although a BaF-doped parahydrogen crystal was not produced in this work, future experiments involving it are planned in order to investigate the influence of the crystal on the energy levels and line widths of the molecule.
This chapter provides an overview of the production of a pure p-H_2 crystal conducted at the LNL INFN laboratories lay a ground work for such projects. The experimental setup consists of two main components: a cryogenic system to grow the crystal matrix and an optical system to characterize it. An analysis has been carried out to indirectly measure the thickness and the orthohydrogen percentage of the crystals.

4.1 Cryogenic and optical system

The parahydrogen crystal growth starts from a pure hydrogen gas, with impurity concentration of 1 ppm, further purified by a cryogenic trap at liquid nitrogen temperature, as shown in Figure 4.1. Subsequently, it is directed through a copper line containing Fe_2O_3 fine powder, which acts as a catalyst to enhance the conversion of o-H_2 to p-H_2. The gas line is then wrapped around a copper block, which is connected to the cold head of a Leybold-Heraeus RG210 pulse tube refrigerator operating at temperatures lower than 20 K. Indium contacts ensure a good thermal exchange between the copper block and the hydrogen line. The gas flowing outside of this line will consist of pure parahydrogen, with orthohydrogen concentrations of approximately 2%. The quality achieved is sufficient for this work, but could be improved and will be further investigated in future experiments. For instance, in the work of Bhandari et al. [97], a significantly lower orthohydrogen fraction ($< 0.1\%$) is reached using a double-stage converter, where each tube was filled with iron(III) oxide and the average temperature was lower than what we can achieve with our apparatus.
In the experimental setup used during this work (see Figure 4.3), the conversion step was bypassed, as we leveraged the capability to produce and store parahydrogen in a separate laboratory of the LNL INFN laboratories, maintaining high purity levels without the complexities associ-

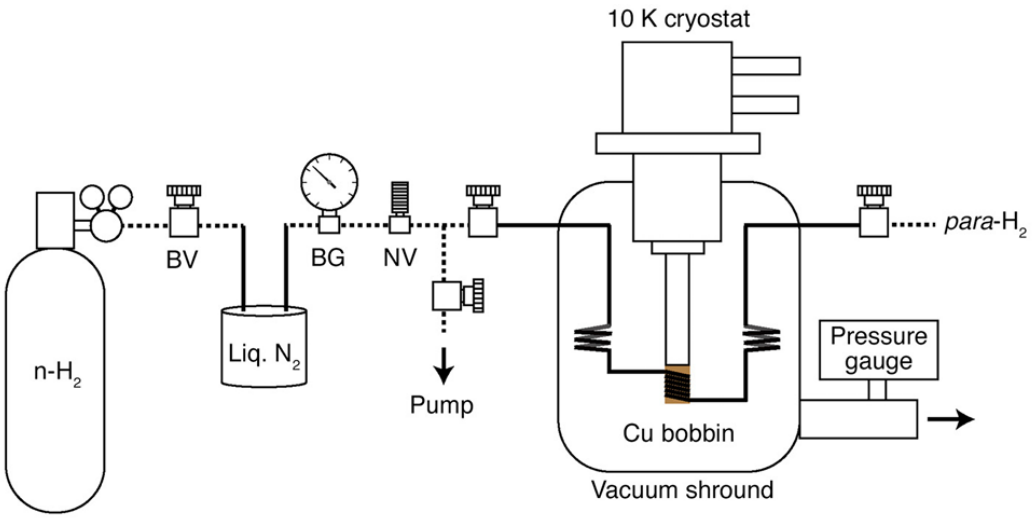

Figure 4.1: Schematic diagram of an ortho to parahydrogen converter. Gaseous normal hydrogen (n-H_2) is cooled through a liquid nitrogen bath to facilitate the conversion. The gas passes through a vacuum shroud containing a copper bobbin cooled to 10 K using a cryostat, enabling the catalytic conversion of ortho-hydrogen to para-hydrogen.

ated with on-site production of p-H_2. However, it's important to note that storing p-H_2 can be tricky due to the endothermic conversion of para to ortho hydrogen [98], which can absorb heat and complicate the maintenance of low temperatures required for stable storage. For instance, in an aluminum tank p-H_2 back conversion is of 1,91%/week [99], starting from a 99.9% pure parahydrogen gas.
In this work, p-H_2 was kept in a tank for a few hours at room temperature, before connecting it to the gas line of the system, regulated through a flow meter. The gas flows out of a 3 mm-diameter nozzle, Figure 4.2 at a distance of less than 10 mm from a 15 mm-diameter sapphire substrate, where the crystal is grown. As shown later in the data analysis, a orthohydrogen concentration of approximately 3% was achieved, similar to the concentration obtained from in-site conversion. The substrate is mounted on an oxygen-free, high thermal conductivity copper plate cooled to approximately 4 K by a cryocooler (mod. Sumitomo RP62B helium pulse tube), as illustrated in Figure 4.3. The temperature of the copper plate near the substrate is monitored using a calibrated silicon diode sensor. The cold head of the cryocooler is enclosed in a copper shield at 50 K and covered with Mylar foil to reduce radiation heating. The cryostat chamber, where the crystal growth occurs, is a six-way cross stainless-steel chamber with DN 200CF flanges. The chamber is evacuated to a base pressure below 10^{-6} mBar using a turbomolecular pump. Once the cryostat is turned on, the chamber reaches a vacuum pressure below 10^{-7} mbar. Optical access to the cryostat is provided by two CaF_2 windows mounted on opposite sides of the growth chamber. One is used for IR absorption measurements, while the other allows IR light collection by an InSb detector.
Note that the setup for crystal growth described in this section, without the need for a converter, can be used for the growth of matrices starting from other gas species as, for instance, neon or hydrogen.

Fourier-Transform Infrared (FT-IR) spectroscopy

To characterize the p-H_2 crystals, we use a Fourier-Transform Infrared (FT-IR) spectroscopy setup. FT-IR spectroscopy is an analytical technique used to identify and quantify chemical substances and crystals. When a molecule absorbs infrared light, it undergoes vibrational transitions, each corresponding to a specific energy and frequency, which is unique to the molecular

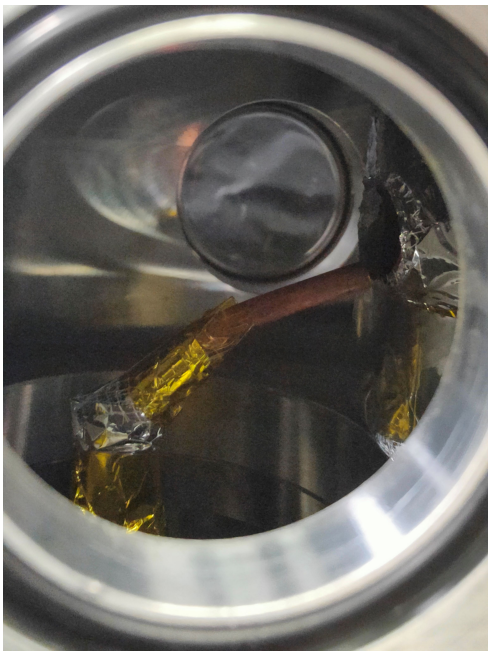

Figure 4.2: Picture of the gas line nozzle set in front of the sapphire substrate. The nozzle is used to directed the desired gas to the cryogenic surface where the crystal develops.

structure and functional groups present in the sample, that can be subsequently detected.
In this work the Bruker Invenio R FT-IR spectrometer (see Figure 4.4), along with the Bruker Opus software, have been used to measure the IR absorption spectrum of the p-H_2 matrix. The main component of the FT-IR spectrometer is the Michelson interferometer, whose illustration is shown in Figure 4.4, mainly consisting of a beamsplitter, a fixed mirror, and a moving mirror. The infrared light source is directed at the beamsplitter, which divides the beam into two paths: one reflecting off the fixed mirror and the other off the moving mirror. After interacting with the sample, the two beams are recombined at the beamsplitter, creating an interference pattern that varies with the position of the moving mirror. The IR beam, transmitted through the sapphire substrate and p-H_2 crystal, is then focused and collimated by gold-coated parabolic mirrors before being detected by an InSb detector, which measures the intensity of transmitted light. A schematic illustration of the optical layout is shown in Figure 4.5. The signal is captured in the time domain, therefore a Fourier transform is applied to convert it into a frequency spectra. The resulting data is either a transmittance or absorbance spectra than can be analyzed to identify molecular structures, based on characteristic absorption peaks corresponding to specific vibrational modes of the molecule.

4.2 Crystal characterization

The absorbance $A(\nu)$ measured by the FT-IR is a function of the wavenumber ν in cm^{-1}. The optical density (OD) used to analyze the crystal is defined through it as:

$$OD(\nu) = -\log_{10}(A(\nu)) = -\log_{10}\left(\frac{I(\nu)}{I_0(\nu)}\right) \tag{4.1}$$

where $I(\nu)$ is the intensity (transmittance) spectrum taken while the crystal is growing and $I_0(\nu)$ is the reference intensity of the cold substrate with no sample deposition. The reference spectrum is usually taken either before sample deposition or after the sublimation of the crystal. The information provided the OD can be used to determine both the thickness of the crystal and the fraction of orthohydrogen in the crystal.

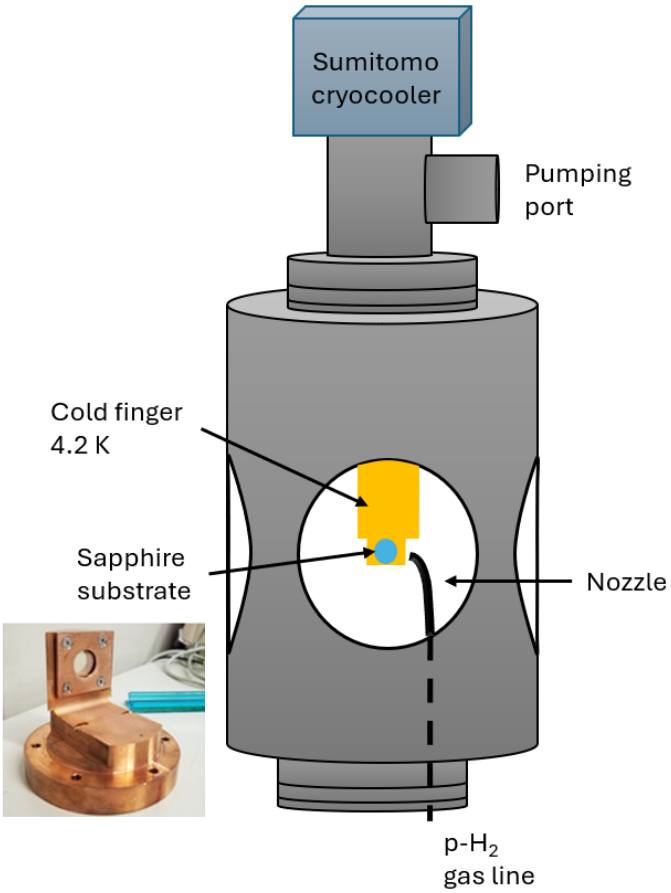

Figure 4.3: Schematic illustration of the experimental setup for p-H_2 crystal growth. Inset: Sapphire substrate holder machined from oxygen-free, high thermal conductivity copper.

The IR absorbance spectrum of solid p-H_2 is usually described through the spectroscopy notation $L_v(J)$, defining the rotovibrational transition to the vibrational level v, starting from $v = 0$ and rotational level J, with L being either Q or S if $\Delta J = 0$ or $+2$, respectively.
Usually three main absorption peaks related to three main rotovibrational transition are observed, mainly:

- A sharp zero-phonon single transition, like the $S_1(0)$ peak around the 4486 cm^{-1} band;
- A broader zero-phonon double transition, like $Q_1(0) + S_0(0)$ and $S_1(0) + S_0(0)$,
- A blue-degraded phonon sideband, where one or more phonon are generated, like the $S_R(0)$ associated to $S_1(0)$, where R denotes a production of phonons.

The peaks corresponding to single transitions are unsuitable for measuring the grown crystal thickness, due to an effect called "cancellation effect" [92]. In highly symmetrical environments the intensities of these transitions are strongly dependent on the symmetries of the occupied site. Since our sample might be composed of a mixture of a fcc and hcp p-H_2 crystal structures, the single transitions peaks are not suitable for our characterization analysis. Our focus is therefore on the double transitions $Q_1(0) + S_0(0)$ $(Q + S)$ and $S_1(0) + S_0(0)$ $(S + S)$, as their intensity depends on the density of p-H_2, a characteristic independent from the crystal structure since their bulk densities are the same.
The thickness h of the crystal can be determined by integrating the optical Density (OD) spec-

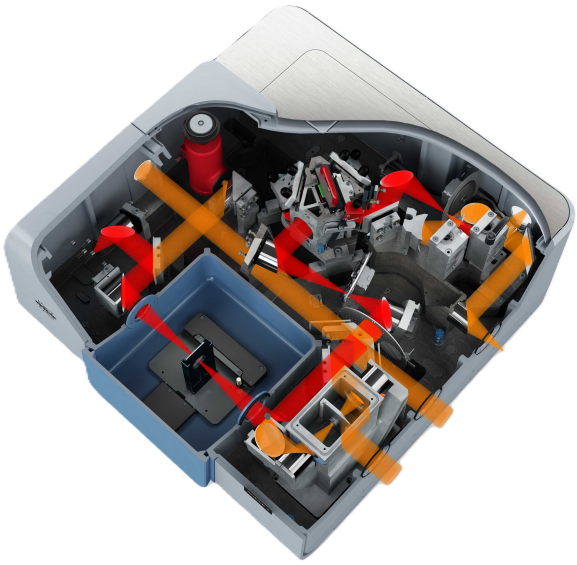

Figure 4.4: Invenio R illustration showing: the complex Michelson interferometer (center), the beam splitter, the optical pathways marked in orange and the high precision moving mirror (top left) along with a series of mirrors for directing the IR beam, and a detectors compartment.

trum in the $Q + S$ region (4495-4520 cm^{-1}) as:

$$h(mm) = 4.8 \cdot 10^{-2} \int_{4485\ cm^{-1}}^{4520\ cm^{-1}} OD(\nu)\, d\nu \tag{4.2}$$

As seen in the lower plot of Figure 4.7, the background OD is subtracted prior to integration, assuming it to be equal to a linear interpolation of the OD at the endpoints of the scan.
The error can be estimated at ±3% in the limit of low orthohydrogen fraction [100].

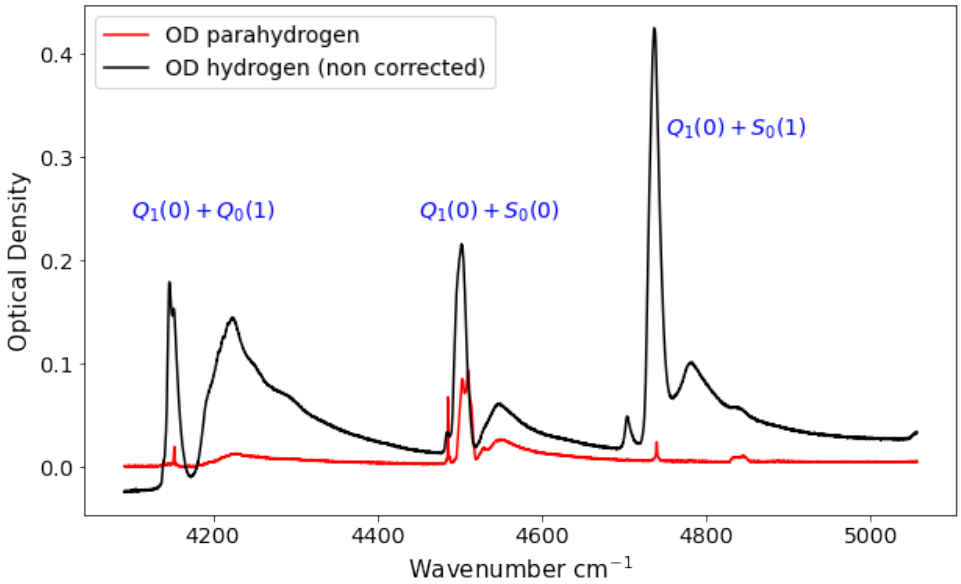

Figure 4.6: Confront of absorption intensity of two crystal: one of pure hydrogen and one of pure parahydrogen. Transitions $Q_1(0) + Q_0(0)$ and $Q_1(0) + S_0(1)$ are dependent on the presence of orthohydrogen.

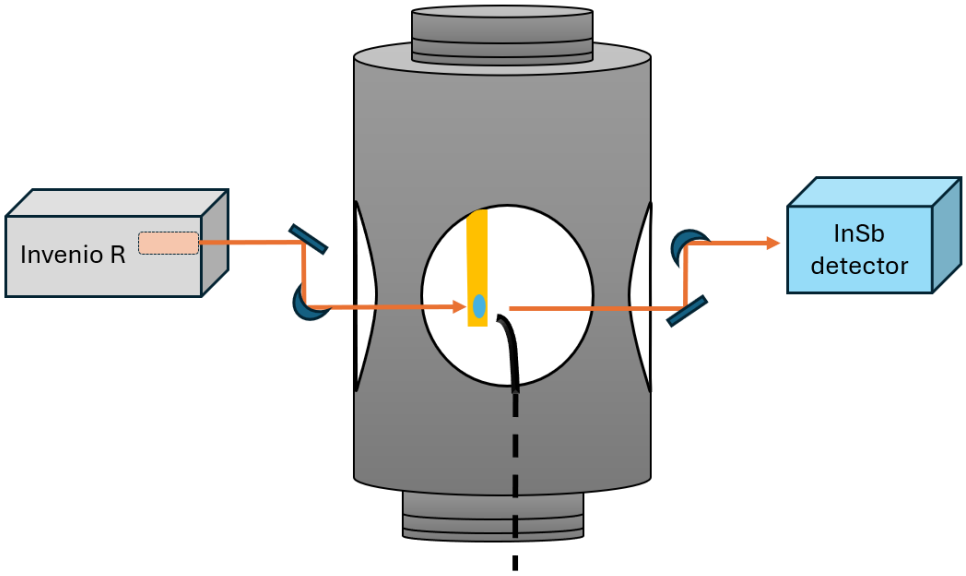

Figure 4.5: Optical layout for the FT-IT spectroscopy. The Invenio R has an built-in IR light source.

The fraction of orthohydrogen $f_{\mathrm{oH_2}}$ can be determined by analyzing the $Q_1(0)+Q_0(0)$ transition, around 4150 cm^{-1}. The optical depth of this transition is ortho dependent, as it can be seen if one confronts the OD of Hydrogen and parahydrogen spectra in Figure 4.6. This dependence have been quantified by Fajarado et al. [101] as:

$$f_{ortho} = \frac{1.24 \cdot 10^{-1} mm}{h(mm)} \int_{4151\ cm^{-1}}^{4154\ cm^{-1}} OD(\nu)\, d\nu \tag{4.3}$$

The estimated accuracy of this dependence is reported to be $\pm 10\%$.
In this work, a broader interval of integration has been used to analyse the ortho-transition. A similar issue happens in the work of Bhandari et al. [97], likely due to a higher presence of orthohydrogen respect to the limit of low orthohydrogen fraction. An estimated accuracy of $\pm 15\%$ is claimed, considering the higher concentration of orthohydrogen and the conditions of the apparatus, such as non linearity in detector response or calibration errors, polarization effects and variations in the refractive index.

Data analysis

A growth analysis of a pure hydrogen gas has been done to test the correct functioning of the apparatus. The sapphire window was at a temperature of $T_s = 4.2$ K while the nozzle exit was at $T_n = 15.7$ K. The vacuum chamber pressure was measured to be $P_{ch} = 2 \cdot 10^{-7}$ mBar. A total number of 10 spectrum have been collected during the growing process of the crystal, at approximately 15 minutes one from the other.

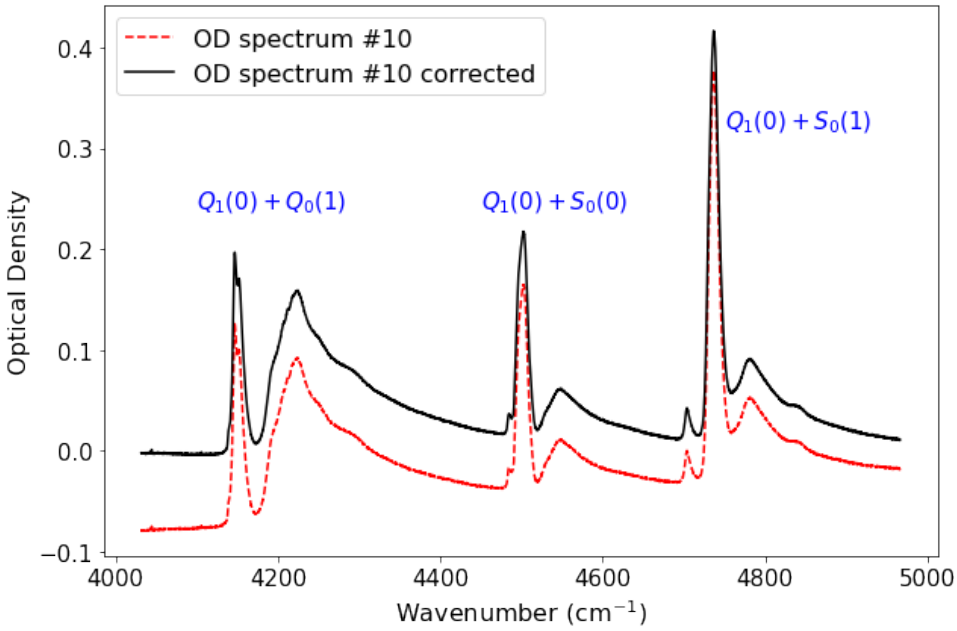

Figure 4.7: The 10^{th} Optical Density spectra of the growing hydrogen crystal. A non linearity correction of the OD baseline, due to the different slope between background and emission spectra, has been done and is shown in the same plot (black spectra). The rotovibrational transitions are labeled.

Transmittance and optical density of the tenth and last taken spectra of hydrogen crystal are shown in figure 4.7. Starting from spectrum #3, the flux was adjusted to an higher value of 10 SCCM, as the chamber pressure was low enough to allow higher gas flux inside.
The fraction of orthohydrogen, as described in equation 4.3, cannot be computed as it is specifically defined for pure parahydrogen crystals. The peak investigated in the equation has a significant contribution from orthohydrogen molecules (see Figure 4.6), resulting in a peak width too large for accurate investigation.

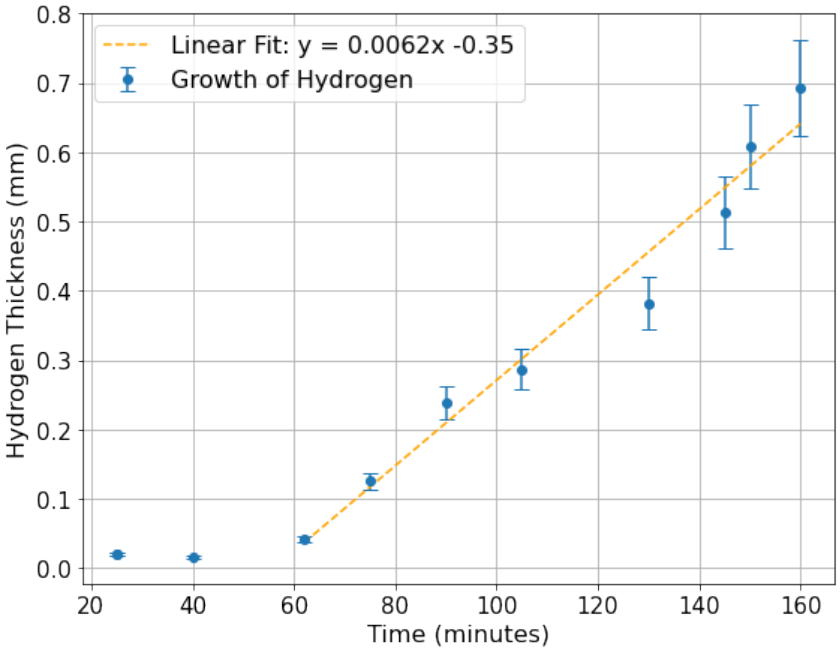

Figure 4.8: Growth of the hydrogen crystal over a time span of 200 minutes. The crystal growth rate is 0.096 ± 0.09 mm/hr.

However, equation 4.2 can be applied to estimate the thickness of the hydrogen crystal. The $Q_1(0) + S_0(0)$ peak's contribution mainly depends on the p-H_2 density, which constitutes approximately 25% of the crystal structure. Therefore, the result of equation 4.2 is multiplied by a factor of 4 to account for the remaining 75% of the crystal composed of o-H_2. The error in the low orthohydrogen limit is about $\pm 3\%$, thus we estimate a total measurement error of $\pm 10\%$, accounting for the mixed composition of the hydrogen crystal.
A growing rate of 0.10 ± 0.09 mm/hr has been measured from a linear fit of the data. The crystal grow starts from the #4, in accordance with the characteristic cryogenic crystal cooling process that usually takes around 40 to 50 minutes to start, depending on the gas flow.

Parahydrogen crystal growth

Even though the test itself did not yield significant data relevant to this work, it successfully achieved its primary objective: confirm that the crystal growth process was functioning effectively.

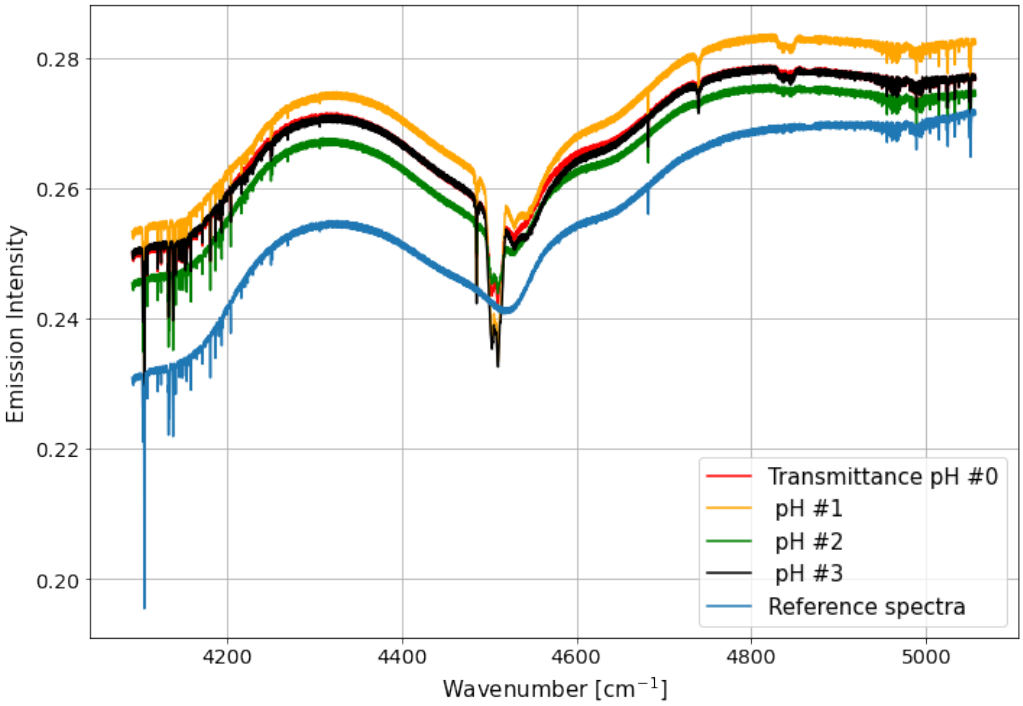

Figure 4.9: Four transmittance spectra obtained during the parahydrogen crystal growth. The reference spectrum, used to compute the optical density (see Equation 4.1), is depicted in blue.

The next step is to grow and characterize a pure parahydrogen crystal. The setup will now include a tube of parahydrogen connected directly to a valve and then to the flow meter. The crystal growth of p-H_2 has been carried out with the sapphire window maintained at a temperature of $T_s = 4.2$ K, while the nozzle exit was set to $T_n = 14.2$ K. The pressure within the vacuum chamber was $P_{ch} = 8 \times 10^{-8}$ mBar. Four spectra were collected during a 100 minutes span, with a first spectra taken after 42 minutes and then one every 20 minutes. The four transmittance spectra are shown in Figure 4.9, along with the reference spectra.

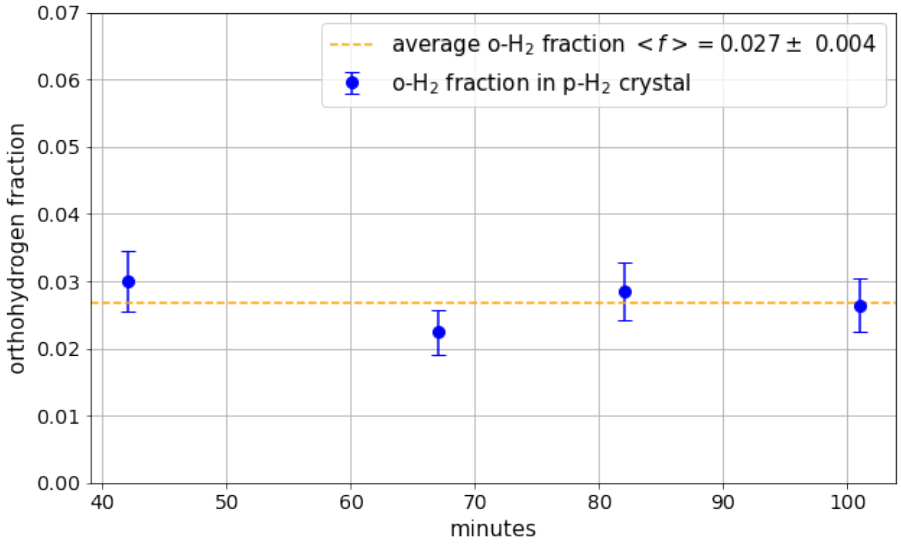

Figure 4.10: Ortohydrogen fraction into the parahydrogen crystal during a time span of a hour. The percentage of orthohydrogen was stable at $< f >= 0.026 \pm 0.004$ during the growth.

As shown in Figure 4.10, our new method of storing parahydrogen in a tube and subsequently connecting it to the system resulted in a good o-H_2 fraction, with an average of $< f >= 0.027 \pm 0.004$, thus approximately 3% presence of orthohydrogen in the crystal. Although better results can be achieved [97], we are confident in our result, as the possibility to store parahydrogen provides us more flexibility over the crystal growth process.
The experiment commenced with a flow rate of 10 SCCM, which was reduced to 5 SCCM after 33 minutes. Following spectra #1, the flux was further decreased to 3 SCCM because the vacuum chamber pressure was above 10^{-6} mBar. This adjustment significantly affected the crystal growth process. As illustrated in Figure 4.11, between measurements #2 and #3, the crystal appears to undergo a sublimation process.

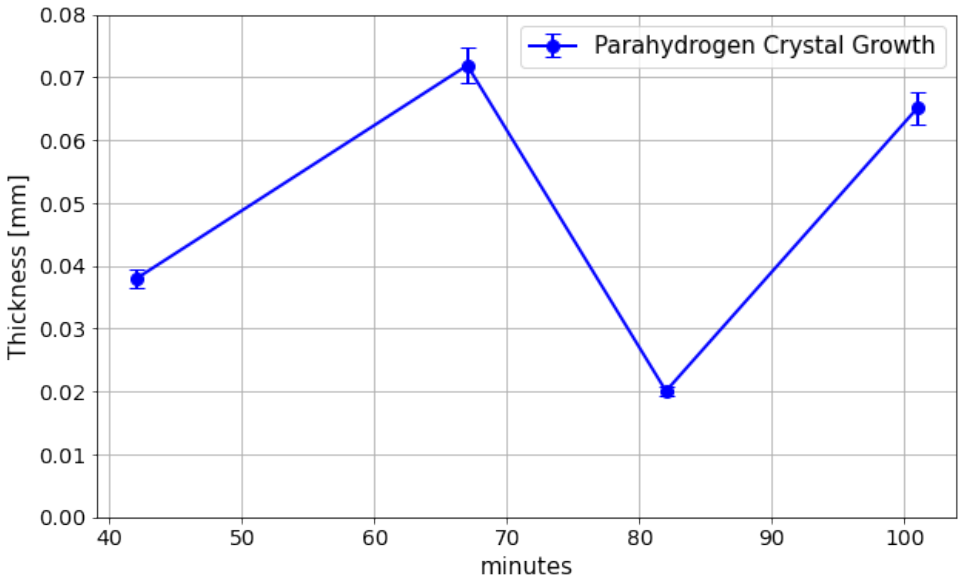

Figure 4.11: Growth of the pure parahydrogen crystal, monitored over a 100 minutes time span. The flow rate of p-H_2 was reduced from 10 to 3 SCCM after the first measurement. The effect of this adjustment probably contributed to the apparent sublimation of the crystal observed between spectra #2 and #3.

An insight of the sublimation is also directly visible from the optical density spectra shown in Figure 4.12. The fraction of o-H_2 does not seem to be directly affected by the flow rate adjustments. However, in equation 4.3, the thickness plays a crucial role. Therefore, further investigation of how the presence of o-H_2 might be influenced by the flow rate will be conducted in future experiments.

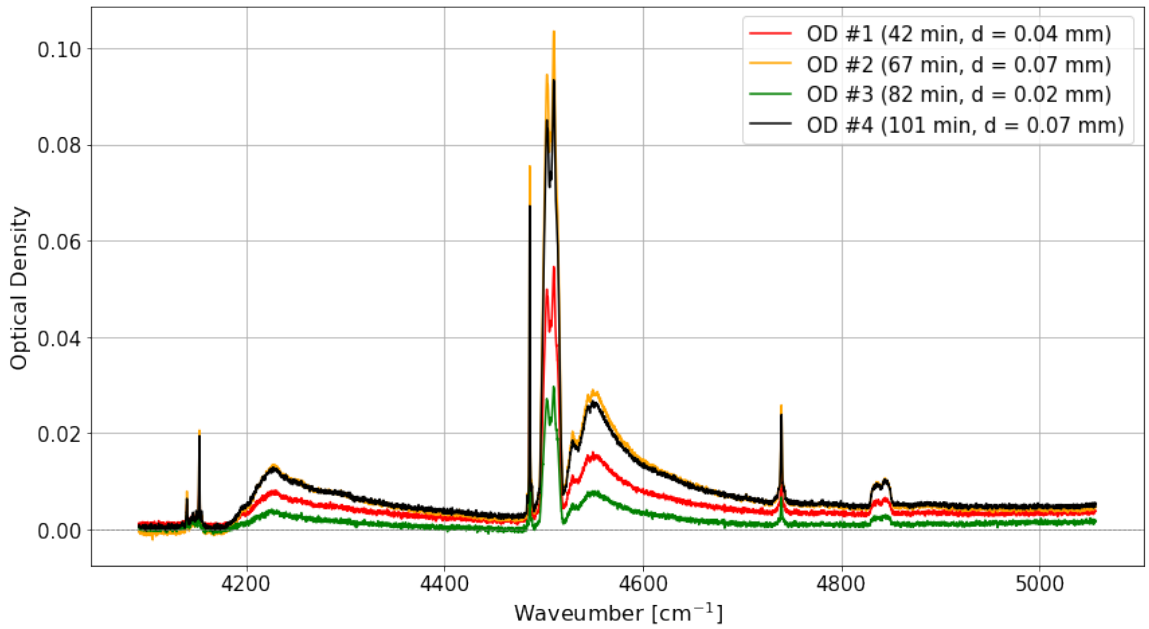

Figure 4.12: The four optical densities obtained during the parahydrogen crystal growth. The difference in peak height between OD #2 and #3, due to a crystal sublimation, is clearly visible (yellow and green spectra).

We lowered the parahydrogen flow to 3 SCCM since, as the gas flows through the chamber, it increases its pressure, especially with very light gases like hydrogen. In this run, the pressure was too high, leading to a poorer thermal connection between external surface and cold finger. This raised the temperature and heated up the substrate, causing the crystal to sublimate. As a consequence, despite reducing the flow, the sublimation process was detected 30 minutes later through spectrum #3.
Although this last measurement did not provide consistent data, it gives us hope for future experiments, as with careful monitoring of the vacuum chamber pressure, we can achieve stable and reliable results as done with the hydrogen crystal.

Conclusions and Outlook

This thesis work is devoted to the development of a molecular source, capable of generating a BaF^+ ion beam, along with the production of a pure parahydrogen crystal with the desired characteristics for electron Electric Dipole Moment (eEDM) measurements.
We motivated searches of eEDM, as the presence of new particles predicted by various beyond the Standard Model (BSM) theories could manifest through an induced asymmetry in the electron's space charge distribution, resulting in a non-zero eEDM (d_e).
Small-scale, table-top experiments are currently pushing the sensitivity limits of d_e measurements by conducting high precision spectroscopy on polar molecules, whose energy levels can shift if a non-zero eEDM is present in the valence electron. The best limit, obtained by the JILA group, University of Colorado, using trapped HfF^+ ions, is of $d_e < 4.1 \times 10^{-30}$ e cm. The result ruled out the existence of new predicted particles with masses up to 40 TeV, a sensitivity out of reach for current particle accelerators.
In this thesis, we lay the groundwork for building an apparatus to measure the eEDM using the matrix isolation technique, which involves doping an inert cryogenic crystal with the guest molecules of interest. Improved sensitivity might be achieved with this method, as we are investigating Barium Monofluoride (BaF) molecules, a polar molecule offering a high internal effective field (E_{eff}), necessary to reach an almost full polarization $P \approx 1$ and potentially long coherent interaction times (τ), both crucial parameters to enhance the eEDM sensitivity. Additionally, we plan to embed those molecules into a parahydrogen (p-H_2) crystal. The crystal structure of p-H_2 has minimal interaction with the guest molecules, facilitating high precision spectroscopy with minimal interference from the environment. The most interesting aspect of this approach is that a large number of molecules (N) can be investigated, further enhancing the eEDM sensitivity, described as:

$$\sigma(d_e) \approx \frac{1}{PE_{\text{eff}}\sqrt{N}\tau} \tag{4.4}$$

The experimental work has been focused on the construction and characterization of:

1. a reliable and efficient source of BaF ions;
2. a setup to grow a pure parahydrogen crystal.

For the first objective, the experimental setup utilizes a ceramic-coated chamber with two concentric filaments. The first filament (oven) heats and evaporates the BaF powder, while the second filament initiates the plasma discharge. Helium is chosen as the activation gas for the plasma discharge due to its efficiency in quickly achieving the necessary energy to ionize BaF molecules. Once the plasma is initiated and BaF molecules have been ionized, they are extracted through a 2 mm aperture at the anode. The resulting molecular beam is then optimized using a solenoid-generated magnetic field, which concentrates the plasma at the center of the chamber. Additionally, an Einzel lens is employed to focus the ion beam over longer distances. Systematic studies with a residual gas analyzer (RGA 200) have demonstrated that setting a solenoid current of $I_S = 1.7$ A and a lens voltage of $U_L = 78.2$ V, while accelerating the ions through the anode at $U_A = 100$ V, results in a consistent and efficient production, yielding approximately

10^{14} molecules per hour.
This high production is essential to achieve the molecular density required in the host p-H_2 matrix. As approximately 10^{13} molecules are needed inside the matrix along one axes, our goal is to achieve a total number of 10^{16} molecules out of the ion source in future experiments.
This goal appears to be feasible, as there is still room for further improvements to the source. For instance, using a larger lens could improve focusing at longer distances, while a larger ion source chamber, combined with optimized filaments, could increase the number of molecules and enhance stability. Future work will explore the integration of a Wien filter which can be used to achieve a pure BaF beam, while a deceleration stage allows the BaF molecules to be embedded in the crystal.
As concerns the second objective, the experimental setup focuses on the growth and characterization of p-H_2 crystals in a vacuum apparatus that will be connected to the molecular source. The cryogenic system developed for this purpose utilizes stored parahydrogen, produced and maintained at high purity levels within a separate laboratory at LNL INFN. The experimental setup avoids the complexity of on-site ortho-to-para conversion by using this pre-purified gas, which is directed through a nozzle onto a sapphire substrate cooled to approximately 4 K, where the crystal will grow.
To characterize the p-H_2 crystal, Fourier-Transform Infrared (FT-IR) spectroscopy is used to obtain the optical density (OD), employed to determine the crystal's thickness and orthohydrogen fraction. The OD spectra reveals characteristic peaks corresponding to specific vibrational transitions. In this work the $Q_1(0) + S_0(0)$ peak is investigated to compute the crystal thickness, while the $Q_1(0) + Q_0(0)$ to evaluate the orthohydrogen fraction. The experimental results demonstrated an average parahydrogen concentration of 97.3%, consistent with the purity of in-site production.
During the crystal growth process, issues were encountered, possibly due to a gas overflow in the chamber that interrupted the growth by raising the substrate temperature and sublimating the crystal. This issue can be overcome by carefully controlling the gas flow parameters and vacuum pressures, as demonstrated by the successful controlled growth of a hydrogen crystal with the same setup.
Upcoming experiments will focus on refining the cryogenic setup to achieve an even higher purity level, as it is critical to fully exploit the optical characteristics and inert host behavior of the parahydrogen, where impurities must be lower than 0.1%. Potentially, even lower levels can be achieved by implementing a double-stage converter and an upgraded cryocooler to reach lower temperatures.
In conclusion, this research paves the way for the preparation of BaF-doped crystals of p-H_2, potentially laying the groundwork for the next generation of precision eEDM measurements.

Bibliography

[1] Gerald Gabrielse. "The standard model's greatest triumph". In: *Physics Today* 66.12 (Dec. 2013), pp. 64–65. ISSN: 0031-9228. DOI: 10.1063/PT.3.2223. eprint: https://pubs.aip.org/physicstoday/article-pdf/66/12/64/15826275/64_1_online.pdf. URL: https://doi.org/10.1063/PT.3.2223.

[2] Steven Weinberg. "Essay: Half a Century of the Standard Model". In: *Phys. Rev. Lett.* 121 (22 Nov. 2018), p. 220001. DOI: 10.1103/PhysRevLett.121.220001. URL: https://link.aps.org/doi/10.1103/PhysRevLett.121.220001.

[3] S. Weinberg. "The making of the Standard Model". In: *The European Physical Journal C* 34.1 (May 2004), pp. 5–13. ISSN: 1434-6052. DOI: 10.1140/epjc/s2004-01761-1. URL: http://dx.doi.org/10.1140/epjc/s2004-01761-1.

[4] Tom W. B. Kibble. *The Standard Model of Particle Physics*. 2014. arXiv: 1412.4094 [physics.hist-ph]. URL: https://arxiv.org/abs/1412.4094.

[5] Peter W. Higgs. "Broken Symmetries and the Masses of Gauge Bosons". In: *Physical Review Letters* 13.16 (1964), pp. 508–509. DOI: 10.1103/PhysRevLett.13.508.

[6] Peter Jenni and Tejinder S. Virdee. "The Discovery of the Higgs Boson at the LHC". In: *Particle Physics Reference Library*. Springer, 2020, pp. 263–309. DOI: 10.1007/978-3-030-35318-6_8.

[7] Steven Weinberg. "Ultraviolet Divergences in Quantum Theories of Gravitation". In: *General Relativity and Gravitation* 1.1 (1979), pp. 16–19. DOI: 10.1007/BF00760451.

[8] Andrei D. Sakharov. "Violation of CP Invariance, C Asymmetry, and Baryon Asymmetry of the Universe". In: *JETP Letters* 5 (1967), pp. 24–27. DOI: 10.1070/PU1991v034n05ABEH002497.

[9] Yosef Nir. "CP Violation In and Beyond the Standard Model". In: *arXiv preprint hep-ph/9911321* (1999). URL: https://arxiv.org/abs/hep-ph/9911321.

[10] D. DeMille, N. R. Hutzler, A. M. Rey, et al. "Quantum sensing and metrology for fundamental physics with molecules". In: *Nature Physics* 20 (2024), pp. 741–749. DOI: 10.1038/s41567-024-02499-9.

[11] David DeMille, John M. Doyle, and Alexander O. Sushkov. "Probing the frontiers of particle physics with tabletop-scale experiments". In: *Science* 357 (2017), pp. 990–994. URL: https://api.semanticscholar.org/CorpusID:3740521.

[12] andB.Renk F. J.Gilman K.Kleinknecht. "Observation of large CP violation in the neutral B meson system". In: *Physical Review Letters* 87 (2001), pp. 0918021-1–6.

[13] D. Kirkby and Y. Nir. "CP violation in meson decays". In: *Journal of Physics G: Nuclear and Particle Physics* 33 (2006). Ed. by W.-M. Yao et al. Review of Particle Physics, pp. 1–24.

[14] F. J. Gilman, K. Kleinknecht, and B. Renk. "The Cabibbo-Kobayashi-Maskawa quark-mixing matrix". In: *Physics Letters B* 592 (2004). Ed. by S. Eidelman et al. Review of Particle Physics, pp. 1–15.

[15] I.B. Khriplovich and M.E. Pospelov. "Magnetic quadrupole moment of W-boson in Kobayashi-Maskawa model". In: *Nuclear Physics B* 420.3 (1994), pp. 505–514. ISSN: 0550-3213. DOI: https://doi.org/10.1016/0550-3213(94)90075-2. URL: https://www.sciencedirect.com/science/article/pii/0550321394900752.

[16] Tanya Roussy et al. "An improved bound on the electron's electric dipole moment". In: *Science (New York, N.Y.)* 381 (July 2023), pp. 46–50. DOI: 10.1126/science.adg4084.

[17] M. Pospelov and A. Ritz. "Electric dipole moments as probes of new physics". In: *Annals of Physics* 318.1 (2005), pp. 119–169. DOI: 10.1016/j.aop.2005.04.002.

[18] B.C. Regan et al. "New limit on the electron electric dipole moment". In: *Physical Review Letters* 88 (2002), p. 071805. DOI: 10.1103/PhysRevLett.88.071805.

[19] J. Baron et al. "Order of Magnitude Smaller Limit on the Electric Dipole Moment of the Electron". In: *Science* 343.6168 (2014), pp. 269–272. DOI: 10.1126/science.1248213.

[20] L. I. Schiff. "Measurability of nuclear electric dipole moments". In: *Physical Review* 132 (1963), pp. 2194–2200. DOI: 10.1103/PhysRev.132.2194.

[21] P. G. H. Sandars. "Enhancement factor for the electric dipole moment of the valence electron in an alkali atom". In: *Physics Letters* 22 (1966), pp. 290–291.

[22] Klaus Kirch and Philipp Schmidt-Wellenburg. "Search for electric dipole moments". In: *EPJ Web of Conferences* 234 (2020), p. 01007. DOI: 10.1051/epjconf/202023401007. URL: https://doi.org/10.1051/epjconf/202023401007.

[23] I. B. Khriplovich and S. K. Lamoreaux. *CP Violation Without Strangeness*. New York: Springer, 1997.

[24] Ricardo Alarcon et al. *Electric dipole moments and the search for new physics*. 2022. arXiv: 2203.08103 [hep-ph]. URL: https://arxiv.org/abs/2203.08103.

[25] Masahiro Fukuda et al. "Local spin dynamics with the electron electric dipole moment". In: *Phys. Rev. A* 93 (1 Jan. 2016), p. 012518. DOI: 10.1103/PhysRevA.93.012518. URL: https://link.aps.org/doi/10.1103/PhysRevA.93.012518.

[26] Timo Fleig and Malaya K. Nayak. "Electron electric dipole moment and hyperfine interaction constants for ThO". In: *Journal of Molecular Spectroscopy* 300 (2014). Spectroscopic Tests of Fundamental Physics, pp. 16–21. ISSN: 0022-2852. DOI: https://doi.org/10.1016/j.jms.2014.03.017. URL: https://www.sciencedirect.com/science/article/pii/S0022285214000782.

[27] Takamasa Momose and Takeshi Shida. "Solid parahydrogen as a novel matrix for matrix isolation spectroscopy". In: *Chemical Physics* 270.2-3 (2001), pp. 373–382. DOI: 10.1016/S0301-0104(01)00386-4.

[28] S J Li et al. "Optical control of BaF molecules trapped in neon ice". In: *New Journal of Physics* 25.8 (2023), p. 082001. DOI: 10.1088/1367-2630/ace9f3.

[29] J. J. Hudson et al. "Improved measurement of the electron electric dipole moment using YbF molecules". In: *Nature* 473 (2011), pp. 493–496.

[30] V. Andreev et al. "Improved limit on the electric dipole moment of the electron". In: *Nature* 562 (2018), pp. 355–360.

[31] Yuval Shagam et al. "Continuous temporal ion detection combined with time-gated imaging: Normalization over a large dynamic range". In: *Journal of Molecular Spectroscopy* 368 (2020), p. 111257. ISSN: 0022-2852. DOI: https://doi.org/10.1016/j.jms.2020.111257. URL: https://www.sciencedirect.com/science/article/pii/S0022285220300254.

[32] T. E. Chupp et al. "Electric dipole moments of atoms, molecules, nuclei, and particles". In: *Reviews of Modern Physics* 91.1 (2019), p. 015001. DOI: 10.1103/RevModPhys.91.015001.

[33] T. Bose et al. “Proceedings of the 2022 Snowmass Summer Study”. In: *Proceedings of the 2022 Snowmass Summer Study*. Seattle, WA, July 2022.

[34] AC Vutha, M Horbatsch, and EA Hessels. “Orientation-dependent hyperfine structure of polar molecules in a rare-gas matrix: A scheme for measuring the electron electric dipole moment”. In: *Physical Review A* 98.3 (2018), p. 032513.

[35] Ian G. Brown. “Vacuum arc ion sources”. In: *Review of Scientific Instruments* 65.10 (Oct. 1994), pp. 3061–3081. DOI: 10.1063/1.1144756. URL: https://doi.org/10.1063/1.1144756.

[36] Peter F. Lang. “Measurement, calculation, and applications of ionization energies and electron affinities of hydrogen and atomic ions”. In: *Monatshefte für Chemie - Chemical Monthly* 154 (2023), pp. 709–716. URL: https://link.springer.com/article/10.1007/s00706-023-03078-z.

[37] Lauren Reutenauer. “2.3: Ionization Techniques”. In: *Chemistry LibreTexts* (2023). URL: https://chem.libretexts.org/Bookshelves/Organic_Chemistry/Introduction_to_Organic_Spectroscopy/02%3A_Mass_Spectrometry/2.03%3A_Ionization_Techniques.

[38] SG Walton et al. “Extraction of positive and negative ions from electron-beam-generated plasmas”. In: *Applied physics letters* 81.6 (2002), pp. 987–989.

[39] Horst Loeb. “Plasma-based ion beam sources”. In: *Plasma Physics and Controlled Fusion* 47 (Nov. 2005), B565. DOI: 10.1088/0741-3335/47/12B/S41.

[40] J. W. Luginsland, Y. Y. Lau, and R. M. Gilgenbach. “Two-Dimensional Child-Langmuir Law”. In: *Physical Review Letters* 77 (1996), pp. 4668–4671. DOI: 10.1103/PhysRevLett.77.4668. URL: https://doi.org/10.1103/PhysRevLett.77.4668.

[41] S. Anders et al. “Plasma distribution of cathodic arc deposition systems”. In: *Journal of Applied Physics* 79.11 (1996), pp. 6785–6788. DOI: 10.1063/1.362258.

[42] RA MacGill, A Vizir, and IG Brown. “On the use of magnetic buckets for ion beam profile tailoring”. In: *Review of Scientific Instruments* 71.2 (2000), pp. 672–674.

[43] M. Szilagyi and J. Szep. “A systematic analysis of symmetric three-electrode electrostatic lenses”. In: *IEEE Transactions on Electron Devices* 34.12 (1987), pp. 2634–2642. DOI: 10.1109/T-ED.1987.23365.

[44] A Adams and F H Read. “Electrostatic cylinder lenses II: Three element einzel lenses”. In: *Journal of Physics E: Scientific Instruments* 5.2 (Feb. 1972), p. 150. DOI: 10.1088/0022-3735/5/2/019. URL: https://dx.doi.org/10.1088/0022-3735/5/2/019.

[45] RT Abdulla and OA Hussein. “Simulation and Optimization of the Optical Properties of an Einzel lens”. In: *Journal of Physics: Conference Series*. Vol. 1530. 1. IOP Publishing. 2020, p. 012128.

[46] Taneli Kalvas. “Beam Extraction and Transport”. In: *CAS - CERN Accelerator School: Ion Sources*. CERN. 2014, pp. 537–564. DOI: 10.5170/CERN-2013-007.537. URL: https://cds.cern.ch/record/1643436.

[47] Ahmad K. Ahmad and Basma Faiz Abd-Alghane. “Design and analysis of the optical properties of electrostatic unipotential lens (einzel lens)”. In: *Journal of Electron Optics* 45.3 (2023), pp. 123–134.

[48] Michael Menzinger and Lars Wåhlin. “High Intensity, Low Energy Spread Ion Source for Chemical Accelerators”. In: *Review of Scientific Instruments* 40.1 (Jan. 1969), pp. 102–105. ISSN: 0034-6748. DOI: 10.1063/1.1683697. URL: https://doi.org/10.1063/1.1683697.

[49] GS Virdi. “An ion-source of ceramic construction suitable for ion-implantation”. In: *Vacuum* 64.1 (2001), pp. 37–40.

[50] Serdar Salman et al. “An investigation of different ceramic coating thermal properties”. In: *Materials & design* 27.7 (2006), pp. 585–590.

[51] Richard E. Russo et al. “Chapter 3 - Laser ablation”. In: *Laser-Induced Breakdown Spectroscopy (Second Edition)*. Ed. by Jagdish P. Singh and Surya N. Thakur. Second Edition. Amsterdam: Elsevier, 2007, pp. 41–70. ISBN: 978-0-12-818829-3. DOI: https://doi.org/10.1016/B978-0-12-818829-3.00003-4. URL: https://www.sciencedirect.com/science/article/pii/B9780128188293000034.

[52] Annemie Bogaerts et al. “Laser ablation for analytical sampling: what can we learn from modeling?” In: *Spectrochimica Acta Part B: Atomic Spectroscopy* 58.11 (2003), pp. 1867–1893. ISSN: 0584-8547. DOI: https://doi.org/10.1016/j.sab.2003.08.004. URL: https://www.sciencedirect.com/science/article/pii/S0584854703001666.

[53] JOHN F. READY. “CHAPTER 3 - Effects Caused by Absorption of Laser Radiation at Opaque Surfaces”. In: *Effects of High-Power Laser Radiation*. Ed. by JOHN F. READY. Academic Press, 1971, pp. 67–125. ISBN: 978-0-12-583950-1. DOI: https://doi.org/10.1016/B978-0-12-583950-1.50008-8. URL: https://www.sciencedirect.com/science/article/pii/B9780125839501500088.

[54] A. Sasaki, S. U. Hayat, and H. Ogawa. “Laser plasma interaction with nanosecond and picosecond laser pulses”. In: *Optical Engineering* 31.9 (1992), pp. 1967–1974.

[55] Y. B. Zel’dovich and Y. P. Raizer. *Physics of Shock Waves and High-Temperature Hydrodynamic Phenomena*. Ed. by W. Hayes. Originally published in two volumes: Vol. I (1966) and Vol. II (1967). Academic Press, 2002. ISBN: 9780323147859.

[56] R. C. Pankhurst. “From Low Speed Aerodynamics to Astronautics.Th. von Kármán. Pergamon Press, London. 1963. 82 pp. Illustrated. 25s.” In: *The Journal of the Royal Aeronautical Society* 68.641 (1964), pp. 351–351. DOI: 10.1017/S0368393100079475.

[57] Yoshio Sone. “Molecular Gas Dynamics: Theory, Techniques, and Applications”. In: 2006. URL: https://api.semanticscholar.org/CorpusID:117259767.

[58] W. Steckelmacher. “Knudsen flow 75 years on: the current state of the art for flow of rarefied gases in tubes and systems”. In: *Reports on Progress in Physics* 49.10 (1986), p. 1083. DOI: 10.1088/0034-4885/49/10/001. URL: https://dx.doi.org/10.1088/0034-4885/49/10/001.

[59] Franck Celestini and Fabrice Mortessagne. “Cosine law at the atomic scale: Toward realistic simulations of Knudsen diffusion”. In: *Physical Review E* 77.2 (Feb. 2008). ISSN: 1550-2376. DOI: 10.1103/physreve.77.021202. URL: http://dx.doi.org/10.1103/PhysRevE.77.021202.

[60] Yan Zhou et al. “Direct Observation Of Rydberg-rydberg Transitions Via Cpmmw Spectroscopy”. In: *PhD thesis* (2014). URL: https://api.semanticscholar.org/CorpusID:93590779.

[61] P. Aggarwal et al. “A supersonic laser ablation beam source with narrow velocity spreads”. In: *Review of Scientific Instruments* 92.3 (Mar. 2021), p. 033202. ISSN: 0034-6748. DOI: 10.1063/5.0035568. eprint: https://pubs.aip.org/aip/rsi/article-pdf/doi/10.1063/5.0035568/13857860/033202_1_online.pdf. URL: https://doi.org/10.1063/5.0035568.

[62] Nicholas R. Hutzler, Hsin-I Lu, and John M. Doyle. “The Buffer Gas Beam: An Intense, Cold, and Slow Source for Atoms and Molecules”. In: *Chemical Reviews* 112.9 (2012). PMID: 22571401, pp. 4803–4827. DOI: 10.1021/cr200362u. eprint: https://doi.org/10.1021/cr200362u. URL: https://doi.org/10.1021/cr200362u.

[63] J. K. Messer and Frank C. De Lucia. "Measurement of Pressure-Broadening Parameters for the CO-He System at 4 K". In: *Phys. Rev. Lett.* 53 (27 Dec. 1984), pp. 2555–2558. DOI: 10.1103/PhysRevLett.53.2555. URL: https://link.aps.org/doi/10.1103/PhysRevLett.53.2555.

[64] Thomas Gantner et al. "Buffer-gas cooling of molecules in the low-density regime: comparison between simulation and experiment". In: *Journal of Physics B: Atomic, Molecular and Optical Physics* 53.14 (June 2020), p. 145302. ISSN: 1361-6455. DOI: 10.1088/1361-6455/ab8b42. URL: http://dx.doi.org/10.1088/1361-6455/ab8b42.

[65] R. deCarvalho, J. Doyle, and B. Friedrich. "Buffer-gas loaded magnetic traps for atoms and molecules: A primer". In: *Eur. Phys. J.* (1999), pp. 289–309. DOI: https://doi.org/10.1007/s100530050572.

[66] J. Kim et al. "Buffer-Gas Loading and Magnetic Trapping of Atomic Europium". In: *Physical Review Letters* 78 (19 1997), pp. 3665–3668. URL: https://doi.org/10.1103/PhysRevLett.78.3665.

[67] S. Truppe et al. "A buffer gas beam source for short, intense and slow molecular pulses". In: *Journal of Modern Optics* 65.5-6 (2018), pp. 648–656. DOI: 10.1080/09500340.2017.1384516. eprint: https://doi.org/10.1080/09500340.2017.1384516. URL: https://doi.org/10.1080/09500340.2017.1384516.

[68] R.V. Krems, William Stwalley, and Bretislav Friedrich. "Cold molecules: Theory, experiment, applications". In: *Cold Molecules: Theory, Experiment, Applications* (Jan. 2009), pp. 1–723.

[69] David Patterson and John M. Doyle. "Bright, guided molecular beam with hydrodynamic enhancement". In: *The Journal of Chemical Physics* 126.15 (Apr. 2007), p. 154307. ISSN: 0021-9606. DOI: 10.1063/1.2717178. eprint: https://pubs.aip.org/aip/jcp/article-pdf/doi/10.1063/1.2717178/14858917/154307_1_online.pdf. URL: https://doi.org/10.1063/1.2717178.

[70] Nicholas R. Hutzler et al. "A cryogenic beam of refractory, chemically reactive molecules with expansion cooling". In: *Phys. Chem. Chem. Phys.* 13 (2011), pp. 18976–18985. DOI: 10.1039/C1CP20901A. URL: https://doi.org/10.1039/C1CP20901A.

[71] S. E. Maxwell et al. *High-flux beam source for cold, slow atoms or molecules.* 2005. DOI: https://doi.org/10.1103/PhysRevLett.95.173201. arXiv: physics/0508100 [physics.atom-ph]. URL: https://arxiv.org/abs/physics/0508100.

[72] James M. Lisy. " Atom, Molecule, and Cluster Beams ". In: *Physics Today* 54.12 (Dec. 2001), pp. 56–58. ISSN: 0031-9228. DOI: 10.1063/1.1445554. eprint: https://pubs.aip.org/physicstoday/article-pdf/54/12/56/11186236/56_2_online.pdf. URL: https://doi.org/10.1063/1.1445554.

[73] Donald H. Levy. "The Spectroscopy of Very Cold Gases". In: *Science* 214.4518 (1981), pp. 263–269. DOI: 10.1126/science.214.4518.263. eprint: https://www.science.org/doi/pdf/10.1126/science.214.4518.263. URL: https://www.science.org/doi/abs/10.1126/science.214.4518.263.

[74] M. D. DiRosa. "Laser-cooling molecules. Concept, candidates, and supporting hyperfine-resolved measurements of rotational lines in the A - X(0,0) band of CaH". In: *Eur. Phys. J. D* 31 (2004), p. 395.

[75] B. K. Stuhl et al. "Magneto-optical Trap for Polar Molecules". In: *Phys. Rev. Lett.* 101 (2008), p. 243002.

[76] S. Truppe, H. Williams, M. Hambach, et al. "Molecules cooled below the Doppler limit". In: *Nature Phys* 13 (2017), pp. 1173–1176. DOI: 10.1038/nphys4241.

[77] P. Aggarwal et al. "Deceleration and Trapping of SrF Molecules". In: *Phys. Rev. Lett.* 127 (17 Oct. 2021), p. 173201. DOI: 10.1103/PhysRevLett.127.173201. URL: https://link.aps.org/doi/10.1103/PhysRevLett.127.173201.

[78] Sreekanth C. Mathavan et al. "Deceleration of a Supersonic Beam of SrF Molecules to 120ms-1". In: *ChemPhysChem* 17.22 (2016), pp. 3709–3713. DOI: https://doi.org/10.1002/cphc.201600813. eprint: https://chemistry-europe.onlinelibrary.wiley.com/doi/pdf/10.1002/cphc.201600813. URL: https://chemistry-europe.onlinelibrary.wiley.com/doi/abs/10.1002/cphc.201600813.

[79] Chi Zhang et al. "Inner-shell excitation in the YbF molecule and its impact on laser cooling". In: *Journal of Molecular Spectroscopy* 386 (2022), p. 111625.

[80] H. D. Ramachandran and A. C. Vutha. "Nuclear T-violation search using octopole-deformed nuclei in a crystal". In: *Physical Review A* 108.1 (July 2023). ISSN: 2469-9934. DOI: 10.1103/physreva.108.012819. URL: http://dx.doi.org/10.1103/PhysRevA.108.012819.

[81] M. G. Kozlov and Andrei Derevianko. "Proposal for a Sensitive Search for the Electric Dipole Moment of the Electron with Matrix-Isolated Radicals". In: *Physical Review Letters* 97.6 (Aug. 2006). ISSN: 1079-7114. DOI: 10.1103/physrevlett.97.063001. URL: http://dx.doi.org/10.1103/PhysRevLett.97.063001.

[82] Eric Whittle, David A. Dows, and George C. Pimentel. "Matrix isolation method for the experimental study of unstable species". In: *The Journal of Chemical Physics* 22.11 (1954). Cited by: 263, p. 1943. DOI: 10.1063/1.1739957. URL: https://www.scopus.com/inward/record.uri?eid=2-s2.0-33846454104&doi=10.1063%2f1.1739957&partnerID=40&md5=d224f9d3454889dcf041a86f16daf95c.

[83] Masashi Tsuge and Yuan-Pern Lee. "Spectroscopy of molecules confined in solid para-hydrogen". In: *Molecular and Laser Spectroscopy*. Elsevier, 2020, pp. 167–215.

[84] HE Hallam and GF Scrimshaw. *Experimental techniques and properties of matrix materials*. Wiley, London, 1973.

[85] Isaac Silvera. "The solid molecular hydrogens in the condensed phase: Fundamentals and static properties". In: *Reviews of Modern Physics - REV MOD PHYS* 52 (Apr. 1980), pp. 393–452. DOI: 10.1103/RevModPhys.52.393.

[86] Masashi Tsuge and Leonid Khriachtchev. "Tunneling Isomerization of Small Carboxylic Acids and Their Complexes in Solid Matrixes: A Computational Insight". English. In: *Journal of Physical Chemistry A* 119.11 (Mar. 2015), pp. 2628–2635. ISSN: 1089-5639. DOI: 10.1021/jp509692b.

[87] Marilyn E. Jacox. "The vibrational energy levels of small transient molecules isolated in neon and argon matrices". In: *Chemical Physics* 189.2 (1994), pp. 149–170. ISSN: 0301-0104. DOI: https://doi.org/10.1016/0301-0104(94)00143-X. URL: https://www.sciencedirect.com/science/article/pii/030101049400143X.

[88] K. Sundararajan et al. "Production and characterization of para-hydrogen gas for matrix isolation infrared spectroscopy". In: *Journal of Molecular Structure* 1117 (2016), pp. 181–191. ISSN: 0022-2860. DOI: https://doi.org/10.1016/j.molstruc.2016.03.068. URL: https://www.sciencedirect.com/science/article/pii/S0022286016302666.

[89] Takamasa Momose and Tadamasa Shida. "Matrix-isolation spectroscopy using solid parahydrogen as the matrix: Application to high-resolution spectroscopy, photochemistry, and cryochemistry". In: *Bulletin of the Chemical Society of Japan* 71.1 (1998), pp. 1–15.

[90] Simon Tam and Mario E. Fajardo. "ORTHO/PARA HYDROGEN CONVERTER FOR RAPID DEPOSITION MATRIX ISOLATION SPECTROSCOPY". In: *Review of Scientific Instruments* 70 (1999), pp. 1926–1932. URL: https://api.semanticscholar.org/CorpusID:97938840.

[91] Clive Cuthbertson and Maude Cuthbertson. "On the refractivity of para-hydrogen". In: *Proceedings of the Royal Society of London. Series A, Containing Papers of a Mathematical and Physical Character* 139.839 (1933), pp. 517–520. DOI: 10.1098/rspa.1933.0034. eprint: https://royalsocietypublishing.org/doi/pdf/10.1098/rspa.1933.0034. URL: https://royalsocietypublishing.org/doi/abs/10.1098/rspa.1933.0034.

[92] Mario E. Fajardo and Simon Tam. "Rapid vapor deposition of millimeters thick optically transparent parahydrogen solids for matrix isolation spectroscopy". In: *The Journal of Chemical Physics* 108.10 (Mar. 1998), pp. 4237–4241. ISSN: 0021-9606. DOI: 10.1063/1.475822. eprint: https://pubs.aip.org/aip/jcp/article-pdf/108/10/4237/19034136/4237_1_online.pdf. URL: https://doi.org/10.1063/1.475822.

[93] Antonini and Co. "Heavy Polar Molecules Beam Production and Characterization: BaF Case". In: (Feb. 2024).

[94] SRS Instruments. *Models RGA100, RGA200, and RGA300 Residual Gas Analyzer*. 2009. URL: https://www.thinksrs.com/products/rga.html.

[95] Guochen Qi et al. "Numerical Simulations and the Design of Magnetic Field-Enhanced Electron Impact Ion Source with Hollow Cylinder Structure". In: *Journal of Analytical Methods in Chemistry* 2020.1 (2020), p. 2809485.

[96] S. H. L. G. Munro. *Mass Spectrometry: Principles and Applications*. 2nd. John Wiley & Sons, 2000. Chap. The Einzel Lens: Design and Operation, pp. 159–174.

[97] Ashok Bhandari et al. "High-purity solid parahydrogen". In: *Review of Scientific Instruments* 92.7 (2021), p. 073202. DOI: 10.1063/5.0049006.

[98] S. Ubaid et al. "Effect of para–ortho conversion on hydrogen storage system performance". In: *International Journal of Hydrogen Energy* 39.22 (2014), pp. 11651–11660. ISSN: 0360-3199. DOI: https://doi.org/10.1016/j.ijhydene.2014.05.101. URL: https://www.sciencedirect.com/science/article/pii/S0360319914014839.

[99] Brian A. Tom et al. "Producing and quantifying enriched para-H2". In: *Review of Scientific Instruments* 80.1 (Jan. 2009), p. 016108. ISSN: 0034-6748. DOI: 10.1063/1.3072881. eprint: https://pubs.aip.org/aip/rsi/article-pdf/doi/10.1063/1.3072881/14827893/016108_1_online.pdf. URL: https://doi.org/10.1063/1.3072881.

[100] Mario E. Fajardo. "Solid Parahydrogen Thickness Revisited". In: *Applied Spectroscopy* 73.12 (2019), pp. 1403–1408. DOI: 10.1177/0003702819861581.

[101] Mario E. Fajardo. "Matrix Isolation Spectroscopy in Solid Parahydrogen: A Primer". In: *Physics and Chemistry at Low Temperatures*. Ed. by Leonid Khriachtchev. Singapore: Pan Stanford Publishing, 2011, pp. 167–202. ISBN: 9789814267519.